Nonadiabatic Effects in Molecular Systems: Electronic Structure and Dynamical Studies

PhD Thesis
Egyetemi Doktori (PhD) értekezés

András Csehi

Supervisor/Témavezető
Dr. Gábor Halász

University of Debrecen
PhD School in Informatics

Debreceni Egyetem
Természettudományi Doktori Tanács
Informatikai Tudományok Doktori Iskola
Debrecen, 2013

Ezen értekezést a Debreceni Egyetem Természettudományi Doktori Tanács Informatikai Tudományok Doktori Iskola Alkalmazott információ technológia és elméleti háttere programja keretében készítettem a Debreceni Egyetem természettudományi doktori (PhD) fokozatának elnyerése céljából.

Debrecen, 2014. .....

Csehi András

Tanúsítom, hogy Csehi András doktorjelölt 2010-2013 között a fent megnevezett Doktori Iskola programjának keretében irányításommal végezte munkáját. Az értekezésben foglalt eredményekhez a jelölt önálló alkotó tevékenységével meghatározóan hozzájárult. Az értekezés elfogadását javasolom.

Debrecen, 2014. .....

Dr. Halász Gábor

témavezető

Nonadiabatic Effects in Molecular Systems: Electronic Structure and Dynamical Studies

Értekezés a doktori (PhD) fokozat megszerzése érdekében
az informatika tudományágban

írta: Csehi András okleveles fizikus

Készült a Debreceni Egyetem Informatikai Tudományok Doktori Iskolája
Alkalmazott információ technológia és elméleti háttere programja keretében.

Témavezető: Dr. Halász Gábor

A doktori szigorlati bizottság:

elnök: Dr. .....
tagok: Dr. .....
Dr. .....

A doktori szigorlat időpontja: 2014. .....

Az értekezés bírálói:

Dr. .....
Dr. .....

A bírálóbizottság:

elnök: Dr. .....
tagok: Dr. .....
Dr. .....
Dr. .....
Dr. .....

Az értekezés védésének időpontja: 2014. .....

Abbreviations applied in the Thesis

ADT	Adiabatic-to-diabatic transformation
BO	Born-Oppenheimer
CASSCF	Complete active space self-consistent field
CC2	Coupled cluster second-order
CI	Conical intersection
DOF	Degree of freedom
ECP	Effective core potential
ESIHT	Excited state intramolecular hydrogen transfer
HF	Hartree-Fock
HOMO	Highest occupied molecular orbital
JT	Jahn-Teller
LUMO	Lowest unoccupied molecular orbital
LVC	Linear vibronic coupling
MCTDH	Multi-configuration time-dependent Hartree
MO	Molecular orbital
MP2	Møller-Plesset second-order
MRCI	Multi-reference configuration interaction
NACT	Nonadiabatic coupling term
NPE	2-(4-nitropyrimidine-2-yl) ethenol
PEP	Potential energy profile
PES	Potential energy surface
PQol	8-(pyrimidine-2-yl) quinolin-ol
QVC	Quadratic vibronic coupling
RJCP	Renner-Jahn coupling parameter
RT	Renner-Teller
SD	Slater determinant
WF	Wavefunction

Contents

1. Introduction

During my PhD studies I have been investigating nonadiabatic properties of molecular systems by means of theoretical tools. In this Thesis I would like to give a brief description of this field of molecular physics and then summarize my own results achieved in the last three years.

The dynamics taking place in a molecule is usually treated in the framework of the Born-Oppenheimer (BO) or adiabatic approximation [1, 2], which separates the motion of the fast electrons and slow nuclei. In this picture, the nuclei move on a single potential energy surface (PES) produced by the faster moving electrons. Although this approach is suitable to handle several chemical and physical processes, it breaks down in many important situations. These are the nonadiabatic processes where the nuclear and electronic motions can couple and so-called conical intersections (CIs) appear [3–8]. In these nonadiabatic phenomena, energy exchange between electrons and nuclei may become significant. Therefore, CIs between electronic PESs play a key mechanistic role [4–6]. In several important processes like dissociation, proton transfer, isomerization of polyatomic molecules, or radiationless deactivation of excited state systems [9–20] CIs can provide efficient channels for ultrafast interstate crossings on the femtosecond time scale. CIs can be formed already between low-lying electronic states of triatomic molecules. In truly large polyatomic systems they are always present.

An important characteristic feature of these CIs is that they behave linearly - like double cones - around the points of degeneracy. Several important books and review articles have demonstrated the existence and relevance of such intersections in recent years [3–6, 8]. The nonadiabatic coupling terms (NACTs) couple the different electronic states in the molecule. This coupling depends on the gap between the two electronic surfaces and may become the largest possible in the vicinity of CIs [5, 7]. Therefore, on approaching CIs, the NACTs become singular and provide the source for wide range of phenomena that are considered as topological effects and lead to several interesting subjects, including the Longuet-Higgins or Berry phase [21–23], the open-path phase and the quantization feature of the NACTs and so forth.

Another type of electronic intersections is the Renner or Renner-Teller (RT) intersection [24] which has quadratic behaviour in the vicinity of the point of degeneracy, as the

coupling between the two electronic states is caused by second-order terms.

Thus, electronic structure degeneracies play the principal role in this Thesis: I investigated nonadiabatic coupling terms in the vicinity of conical intersections and Renner-Teller intersections and their topological effects on several related physical quantities. I also studied the entanglement between so-called Jahn-Teller intersections (namely conical intersections induced by symmetry, as the involved electronic states belonging to the same irreducible representation are degenerate as long as the symmetry is present in the system) and RT intersections. I investigated molecular switches which are typically based on conical intersections and provide a very useful application in practice. Quantum dynamical calculations through CIs have also been carried out in the present work.

The structure of this Thesis is as follows: After a general introduction (chapter 1.), a brief description of the theoretical background of nonadiabatic processes will be given in chapter 2. In addition, the basics of electronic structure and nuclear dynamical approaches will be presented in that part of the Thesis as well. Chapters 3. and 4. discuss topological issues of the electronic structure of molecules. In chapter 3., the relation between conical intersections and the topological phase is detailed, while chapter 4. reports on the entanglement between Jahn-Teller and Renner-Teller intersections. Chapter 5. is devoted to molecular switches introducing the history of their evolution and the basic concepts of such systems. Finally, in chapter 6. I will present a method for describing the short-time dynamics of large polyatomic systems at conical intersections. After that, a summary and conclusions of the results will be given. My own results will be discussed separately within the chapters, namely they will be detailed in the so-called results sections. In the prologues of chapters 3-6. I will always specify the sections containing the own results. In addition, a short declaration will be presented at the end of these chapters specifying my own contributions.

2. Theoretical background

In order to make my results more transparent and easier to understand, I devote this chapter to the introduction of the basic concepts of the phenomena discussed in this Thesis. The main milestones of the theoretical treatment of molecular systems will be presented both from the electronic structure and nuclear dynamical point of view. Section 2.1 describes the fundamental Born-Oppenheimer approximation of quantum chemistry and its limitation, which is the source of a vast number of interesting physical phenomena. These so-called nonadiabatic processes are closely related to electronic degeneracies, which will be the subject of the subsequent section. I considered relevant to summarize the most important electronic structure approximations in section 2.3. There I discuss the Hartree-Fock method which is a starting point for almost all higher level approximations. After that several approaches for calculating electron correlation energy are introduced. The final section of this chapter is devoted to the basic principles of nuclear dynamics studies. I will focus on different wavefunction ansatz and the related equations of motion in a comprehensive manner, starting from the simplest and approaching the more involved techniques.

2.1 The Born-Oppenheimer and nonadiabatic approximations

Let us consider a molecule consisting of N_{el} electrons and N_{nuc} nuclei. Let the charge and mass of the electrons be denoted by -e and m_{el}, respectively. The charge of the nucleus with label α is then $Z_\alpha \cdot e$ and the mass is M_α. Let the coordinates of the electrons be $\vec{r}=\{ \vec{r}_k$, k=1,2, ... N_{el} $\}$ and for the nuclei $\vec{R}=\{ \vec{R}_\alpha$, α=1,2, ... N_{nuc} $\}$. The total Hamiltonian of the molecular system in nonrelativistic approximation then has the following form [6]:

$$\hat{H}_{tot}(\vec{r},\vec{R}) = \hat{T}_{nuc}(\vec{R}) + \hat{T}_{el}(\vec{r}) + \hat{U}(\vec{r},\vec{R}) \tag{2.1.1}$$

where

$$\hat{T}_{nuc} = -\frac{\hbar^2}{2}\sum_{\alpha=1}^{N_{nuc}} \frac{1}{M_\alpha}\Delta_\alpha \tag{2.1.2}$$

is the nuclear kinetic energy operator,

$$\hat{T}_{el} = -\frac{\hbar^2}{2m_{el}}\sum_{k=1}^{N_{el}} \Delta_k \tag{2.1.3}$$

is the electronic kinetic energy operator and

$$\hat{U}(\vec{r},\vec{R}) = -e^2 \sum_{\alpha=1}^{N_{nuc}} \sum_{k=1}^{N_{el}} \frac{Z_\alpha}{r_{\alpha k}} + e^2 \sum_{\alpha<\beta}^{N_{nuc}} \frac{Z_\alpha Z_\beta}{R_{\alpha\beta}} + e^2 \sum_{k<l}^{N_{el}} \frac{1}{r_{kl}} \tag{2.1.4}$$

is the potential energy operator of the nuclei and the electrons. Here the first term on the right side describes the nuclear-electron attraction, while the second and third terms correspond to the nuclear-nuclear and electron-electron repulsions, respectively.

Given the above Hamiltonian of the molecular system, one has to solve the time-independent Schrödinger equation in order to obtain the stationary eigenstates and corresponding eigenenergies of the total system:

$$\hat{H}_{tot}(\vec{r},\vec{R})\psi(\vec{r},\vec{R}) = E_{tot}\psi(\vec{r},\vec{R}) \quad . \tag{2.1.5}$$

The Born-Oppenheimer approximation provides a great simplification to this problem [1]: It is well known that the masses of the nuclei (M_α) are 3 - 4 orders of magnitude larger than those of the electrons (m_{el}). Hence the electrons move much faster than the nuclei. This fact gives rise to the separation of the movement of the two types of particles eventuating two separate equations, one for the electrons and one for the nuclei. As will be demonstrated later the BO approximation is not always valid. Phenomena beyond the limitations of the BO approximation will be discussed in the second half of this section.

Within the frames of the BO approximation the nuclei can be considered clamped in space, namely $\hat{T}_{nuc} = 0$ ($\hat{H}_{tot} = \hat{T}_{el}(\vec{r}) + \hat{U}(\vec{r};\vec{R}) = \hat{H}_{el}$). By this the following equation is given for the electrons [6]:

$$\hat{H}_{el}\xi_i(\vec{r};\vec{R}) = V_i(\vec{R})\xi_i(\vec{r};\vec{R}) \quad . \tag{2.1.6}$$

There is a different set of these equations for each nuclear configuration, thus the stationary electronic eigenstates, $\xi_i(\vec{r};\vec{R})$ and the corresponding energies, $V_i(\vec{R})$ are parametrically dependent on $\vec{R}$. The exact solutions of the total Schrödinger equation (2.1.5) can be expanded in terms of the above Born-Oppenheimer eigenstates:

$$\psi(\vec{r},\vec{R}) = \sum_i \chi_i(\vec{R})\xi_i(\vec{r};\vec{R}) \tag{2.1.7}$$

where the $\chi_i(\vec{R})$ are the nuclear functions that act as expansion coefficients. Inserting (2.1.7) into (2.1.5), multiplying from the left by one particular electronic function, ξ_j and

then integrating over the electronic coordinates, we obtain the following coupled equations:

$$[\hat{T}_{nuc} + \hat{V}_j]\chi_j - \sum_i \hat{\Lambda}_{ji}\chi_i = E_{tot}\chi_j \tag{2.1.8}$$

where

$$\hat{\Lambda}_{ji} = \frac{1}{2M}(2\vec{F}_{ji}\nabla + G_{ji}) \tag{2.1.9}$$

are the matrix elements of the nonadiabatic coupling operator. These terms describe the dynamical interaction between the electronic and nuclear motions. In (2.1.9) M is the effective mass of the system, $\vec{F}_{ji}$ is the derivative coupling vector:

$$\vec{F}_{ji} = \langle \xi_j | \nabla \xi_i \rangle = \frac{\langle \xi_j | (\nabla \hat{H}_{el}) | \xi_i \rangle}{V_i - Vj} \tag{2.1.10}$$

(later in the Thesis I will often refer to (2.1.10) as $\vec{\tau}_{ji}$)
and

$$G_{ji} = \langle \xi_j | \nabla^2 \xi_i \rangle = (\nabla \vec{F})_{ji} + (\vec{F}\vec{F})_{ji} \tag{2.1.11}$$

is the scalar coupling.
It is important to notice here that the electronic eigenenergies, V_j play the role of the potential energy in the nuclear equation of motion (2.1.8). The $\hat{\Lambda}_{ji}$ terms couple the electronic and nuclear motions. If they can be neglected, we obtain the Born-Oppenheimer approximation. In this picture the nuclear and electronic motions are decoupled and the nuclei move on a single electronic potential energy surface. The neglect of the nonadiabatic coupling terms in (2.1.8) is justified in many cases, since the large M makes the $\hat{\Lambda}_{ji}$ small. However, $\hat{\Lambda}_{ji}$ are inversly proportional to the energy differences between the corresponding electronic energies (see (2.1.10)), which means, when the potential energy surfaces meet, the coupling becomes singular and the BO approximation breaks down.

Using (2.1.9) and (2.1.11), the nuclear Schrödinger equation can be written in the following form [6, 25]:

$$\left[-\frac{1}{2M}(\nabla + \vec{F})^2 + \hat{V} \right] \chi = E_{tot}\chi \tag{2.1.12}$$

where the kinetic energy operator has been replaced by the so-called dressed kinetic energy operator, $(\nabla + \vec{F})^2$ and the potential energy matrix $\hat{V}$ is diagonal. In (2.1.12) the nonadiabatic coupling vector is transformed into the kinetic energy term. In the vicinity of an

intersection of two electronic states the nonadiabatic coupling is singular, therefore it is desirable to transform (2.1.12) to a form where the coupling is included in the potential term. This can be done by a unitary transformation, which is often referred to as the adiabatic-to-diabatic transformation (ADT) in the literature. If the transformation is denoted by $\hat{A}$, then the connection between the adiabatic and diabatic wavefunctions is:

$$\chi = \hat{A}\tilde{\chi} \tag{2.1.13}$$

$$\xi = \tilde{\xi}\hat{A}^{\dagger} \tag{2.1.14}$$

where $\tilde{\chi}$ and $\tilde{\xi}$ are the diabatic electronic and nuclear wavefunctions, respectively. By a proper choice of the transformation $\hat{A}$, the coupling can be removed from the kinetic energy term and transferred to the $\hat{W}$ potential energy. The price we pay is that $\hat{W}$ will have nonzero offdiagonal elements as well. In this case the diabatic Schrödinger equation has the following form:

$$\left[-\frac{1}{2M}\Delta + \hat{W} \right] \tilde{\chi} = E_{tot}\tilde{\chi} \tag{2.1.15}$$

where $\hat{W}$ is given by the transformation:

$$\hat{W} = \hat{A}^{\dagger}\hat{V}\hat{A} \quad . \tag{2.1.16}$$

When investigating nonadiabatic processes, eq. (2.1.15) is used for describing the nuclear motion problem.

2.2 Degenerate states and conical intersections

The diabatic potential matrix, $\hat{W}$ in (2.1.15) can be expanded in Taylor series around $\vec{R}_0$ which can be the point of the equilibrium, the point of an intersection or any other nuclear arrangement. By doing so one can reveal information about the topology of the potential energy surfaces [6].

$$\hat{W} = \hat{W}^{(0)} + \hat{W}^{(1)} + \hat{W}^{(2)} + \hat{W}^{(3)} + \quad ... \tag{2.2.1}$$

In $\vec{R}_0$ the zero-order term, $\hat{W}^{(0)}$ can be chosen to be equal to the diagonal $\hat{V}$:

$$\hat{W}^{(0)} = \hat{V}(\vec{R}_0) \quad . \tag{2.2.2}$$

The first-order matrix elements of $\hat{W}$ can be expressed in terms of the adiabatic electronic functions at $\vec{R}_0$:

$$W^{(1)}_{\alpha,ij} = \left[\left\langle \xi_i \middle| \frac{\partial \hat{H}_{el}}{\partial R_\alpha} \middle| \xi_j \right\rangle\right] R_\alpha \tag{2.2.3}$$

where R_α is the α component of the displacement vector relative to $\vec{R}_0$. The diagonal bra-ket terms in (2.2.3) are called force integrals and often denoted as $\vec{\kappa}^{(1)}$ (i=j=1) and $\vec{\kappa}^{(2)}$ (i=j=2) while the off-diagonal term is called linear coupling and regularly termed as $\vec{\lambda}$. Using the above notations we can write:

$$W^{(1)}_{11} = \vec{\kappa}^{(1)}\vec{R} \quad , \quad W^{(1)}_{22} = \vec{\kappa}^{(2)}\vec{R} \quad , \quad W^{(1)}_{12} = \vec{\lambda}\vec{R} \quad . \tag{2.2.4}$$

Another important vector that will be used later is the gradient difference vector:

$$\vec{\delta} = \frac{1}{2}(\vec{\kappa}^{(2)} - \vec{\kappa}^{(1)}) \quad . \tag{2.2.5}$$

In order to determine the adiabatic potential energy surfaces of the system, one has to find the eigenvalues of the diabatic potential matrix.

$$\hat{V} = \hat{A}\hat{W}\hat{A}^{\dagger} \tag{2.2.6}$$

If we consider a two-state system, the adiabatic surfaces can be expressed analytically:

$$V_{\pm} = \Sigma \pm \sqrt{\Delta^2 + W^2_{12}} \tag{2.2.7}$$

where

$$\Sigma = \frac{1}{2}(W_{11} + W_{22}) \quad \text{and} \quad \Delta = \frac{1}{2}(W_{22} - W_{11}) \quad . \tag{2.2.8}$$

Using (2.2.4) and (2.2.5) the following relations hold:

$$\frac{1}{2}(W^{(1)}_{22} - W^{(1)}_{11}) = \vec{\delta}\vec{R} \quad \text{and} \quad W^{(1)}_{12} = \vec{\lambda}\vec{R} \quad . \tag{2.2.9}$$

If we choose now $\vec{R}_0$ to be the point of an intersection ($W^{(0)}_{11}$=$W^{(0)}_{22}$), then the adiabatic energies V_+ and V_- can be degenerate only if the two conditions are simultaneously fulfilled:

$$\Delta = \vec{\delta}\vec{R} = 0 \tag{2.2.10}$$

$$W^{(1)}_{12} = \vec{\lambda}\vec{R} = 0 \quad . \tag{2.2.11}$$

This will generally happen only if the two terms are independent, i.e., they are functions of different coordinates. In polyatomic systems the large number of degrees of freedom provides that (2.2.10) and (2.2.11) may, in principle, always be fulfilled irrespective of the symmetry of the states. In our arguments so far we concentrated on the vicinity of R_0, hence the linear expansion is justified. Near the degeneracy, $\Delta = \vec{\delta}\vec{R}$ and $W_{12} = \vec{\lambda}\vec{R}$ thus, to first order, the degeneracy is lifted in the space spanned by the vectors $\vec{\delta}$ and $\vec{\lambda}$. Furthermore, from (2.2.7) the topology of the surfaces are a double-cone meeting at the point of degeneracy. The space of the two vectors is termed the branching space or the g-h plane. Orthogonal to the branching space is the intersection space in which the degeneracy is not lifted. If N is the number of internal coordinates, this space thus forms a N-2 dimensional seam, at each point of which is a conical intersection.

2.3 Electronic structure methods

In this section I will focus on wavefunction based approximations for the investigation of the electronic structure of molecular systems. All the approaches presented in this section are concerned with solving the electronic Schrödinger equation of (2.1.6). For the sake of simplicity, the subscript of the Hamiltonian in eq. (2.1.6) will be dropped and the electronic Hamiltonian will be denoted as $\hat{H}$ in this section. Furthermore, electronic wavefuntions will be denoted as φ and Ψ instead of ξ.

Wavefunction based methods use molecular orbitals (as linear combinations of atomic orbitals) for the construction of the wavefunction of the electronic system. For a system of N electrons the wavefunction has 4N variables taking into account the spatial and spin coordinates. The starting point in this section will be the fundamental Hartree-Fock method and then the basic concepts of higher level variational and perturbative approximations will be introduced as well.

2.3.1 The Hartree-Fock approximation

The Hartree-Fock (HF) approximation (often referred to as molecular orbital approxima-

tion) plays an important role in computational chemistry and physics, constituting the basis of most of the advanced techniques. The simple picture of electrons occupying orbitals is a very useful and demonstrative approximation, however, lacks some features. In this subsection I will describe the main pillars of the HF theory which is a very important starting point for more accurate methods that include the effect of electron correlation [26].

The HF theory can be equated to single determinant theory, thus we are interested in finding a set of spin orbitals $\{\zeta_a\}$ such that the single determinant formed from these spin orbitals

$$|\Psi_0\rangle = |\zeta_1\zeta_2\cdots\zeta_a\zeta_b\cdots\zeta_N\rangle \tag{2.3.1.1}$$

is the best possible approximation to the ground state of the N-electron system described by the Hamiltonian $\hat{H}$. According to the variational principle, the best spin orbitals are those which minimize the electronic energy

$$V_0 = \langle\Psi_0|\hat{H}|\Psi_0\rangle \quad . \tag{2.3.1.2}$$

Applying the functional variational principle, one finds the following integro-differential equation, the Hartree-Fock equation for the best spin orbitals [26]:

$$\left[\hat{h}(1) + \sum_{b\neq a}\hat{\mathcal{F}}_b(1) - \sum_{b\neq a}\hat{\mathcal{K}}_b(1)\right]\zeta_a(1) = \epsilon_a\zeta_a(1) \quad . \tag{2.3.1.3}$$

In (2.3.1.3), $\hat{h}(1)$ contains the electronic kinetic energy and the nuclear-electronic attraction terms:

$$\hat{h}(1) = -\frac{1}{2}\nabla_1^2 - \sum_A \frac{Z_A}{r_{1A}} \tag{2.3.1.4}$$

while $\hat{\mathcal{F}}_b(1)$ and $\hat{\mathcal{K}}_b(1)$ are the coulomb and exchange operators, respectively. Their effect on a certain spin orbital, $\zeta_a(1)$ can be expressed as follows:

$$\hat{\mathcal{F}}_b(1)\zeta_a(1) = \left[\int d\mathbf{x_2}\zeta_b^*(2)r_{12}^{-1}\zeta_b(2)\right]\zeta_a(1) \tag{2.3.1.5}$$

$$\hat{\mathcal{K}}_b(1)\zeta_a(1) = \left[\int d\mathbf{x_2}\zeta_b^*(2)r_{12}^{-1}\zeta_a(2)\right]\zeta_b(1) \quad . \tag{2.3.1.6}$$

The HF equation, (2.3.1.3) can be written in a more compact form:

$$\hat{f}|\zeta_a\rangle = \epsilon_a|\zeta_a\rangle \tag{2.3.1.7}$$

with $\hat{f}$ being the Fock operator:

$$\hat{f}(1) = \hat{h}(1) + \hat{v}^{HF}(1) \tag{2.3.1.8}$$

and

$$\hat{v}^{HF}(1) = \sum_b \hat{\mathcal{F}}_b(1) - \hat{\mathcal{K}}_b(1) \tag{2.3.1.9}$$

the Hartree-Fock potential without restriction in the summation. The HF equation is an eigenvalue equation for the spin orbitals and energies. In practice it can be solved exactly only for atoms. A basis set is always introduced for expansion of the spin orbitals and the resulting matrix equations has to be solved. As the basis set approaches completeness, the spin orbitals approach the exact HF spin orbitals as well. It has not been emhasized so far, but (2.3.1.3) is rather a pseudo-eigenvalue problem, since the Fock operator has a functional dependence, through the coulomb and exchange operators on the $\{\zeta_a\}$ spin orbitals. Therefore the HF equations are nonlinear and have to be solved in an iterative manner.

2.3.2 Multi-reference methods

Although the HF approximation is very successful in many situations, it has its own limitations. It gives qualitatively wrong results for ionization potentials, or the restricted HF method can't handle the dissociation of molecules into open-shell systems. Though unrestricted HF gives a qualitatively correct description, the resulting energies are not accurate enough. The major drawback of HF emerges from the fact that only a single determinant is used for the description of the wavefunction. Thus electron correlation is completely neglected in this approximation. There exist many procedures for improving the HF method. In this subsection I will focus on two of them: the Configuration Interaction and the Multiconfiguration Self-Consistent Field theories. Both of them use a multideterminantal wavefunction ansatz, therefore electron correlation is taken into account in these approaches, which is defined as the difference between the exact nonrelativistic energy of the system ($\mathcal{E}_0$) and the HF energy (V_0) in the limit that the basis set approaches completeness:

$$E_{corr} = \mathcal{E}_0 - V_0 \quad . \tag{2.3.2.1}$$

The Configuration Interaction approximation is one of the formally simplest methods for calculating the correlation energy. It is based on the diagonalization of the N-electron Hamiltonian in a basis of N-electron Slater determinants. The exact wavefunction is represented as

a linear combination of N-electron trial functions and then the linear variational principle is applied. If the basis were complete, one would obtain exact energies not only for the ground state, but also for the excited states. In practice, however the size of the basis is limited and the length of the expansion has to be truncated too. A suitable set of N-electron functions can be formed from the ground state Slater determinant by removing electrons from certain occupied orbitals and putting them into virtual orbitals. By doing so one can group the singly, doubly, triply, etc. excited determinants and write the wavefunction ansatz [26]:

$$|\varphi_0\rangle = c_0|\Psi_0\rangle + \sum_{ar} c_a^r|\Psi_a^r\rangle + \sum_{\substack{a<b\\r<s}} c_{ab}^{rs}|\Psi_{ab}^{rs}\rangle + \sum_{\substack{a<b<c\\r<s<t}} c_{abc}^{rst}|\Psi_{abc}^{rst}\rangle + \cdots \tag{2.3.2.2}$$

where the a, b, c, ... indices refer to occupied orbitals, while r, s, t, ... label virtual orbitals in the determinants. Given some arbitrary 2K spin orbitals, we can construct $\binom{2K}{N}$ different N-electron Slater determinants. Unfortunately, even for small molecules and moderately sized basis sets this number becomes enormous. Thus for practical calculations one has to truncate the full Configuration Interaction ansatz of (2.3.2.2). A typical choice is when the trial function contains determinants which differ from Ψ_0 by at most two spin orbitals.

In order to give an expression for the correlation energy, one can turn to the linear variation principle. An equivalent formulation is to consider

$$\hat{H}|\varphi_0\rangle = \mathcal{E}_0|\varphi_0\rangle \tag{2.3.2.3}$$

where $|\varphi_0\rangle$ is given by (2.3.2.2) and then successively multiply this equation by $\langle\Psi_0|$, $\langle\Psi_a^r|$, $\langle\Psi_{ab}^{rs}|$ etc.. Before doing so, (2.3.2.3) can be rewritten as:

$$(\hat{H} - V_0)|\varphi_0\rangle = (\mathcal{E}_0 - V_0)|\varphi_0\rangle = E_{corr}|\varphi_0\rangle \quad . \tag{2.3.2.4}$$

As a result of the above-mentioned consecutive multiplications, we end up with a hierarchy of equations that must be solved simultaneously to get the correlation energy. This set of coupled equations is extremely large if all possible excitations are included, giving another reason for the need of truncation. A reasonable and computationally still viable truncation is obatined by considering single and double excitations in (2.3.2.2) along with the ground state determinant. It can be proved that single excitations do not give significant contribution to the correlation energy and by neglecting them the following pair of coupled equations holds

for the coefficients of double excitations:

$$\sum_{\substack{c<d\\t<u}} c_{cd}^{tu}\langle\Psi_0|\hat{H}|\Psi_{cd}^{tu}\rangle = E_{corr} \tag{2.3.2.5}$$

$$\langle\Psi_{ab}^{rs}|\hat{H}|\Psi_0\rangle + \sum_{\substack{c<d\\t<u}} c_{cd}^{tu}\langle\Psi_{ab}^{rs}|(\hat{H}-V_0)|\Psi_{cd}^{tu}\rangle = c_{ab}^{rs}E_{corr} \quad . \tag{2.3.2.6}$$

These two equations determine the correlation energy. After introducing matrix notation and solving the equation for E_{corr}, the following expression is given within the frames of doubles approximation:

$$E_{corr} \cong -\sum_{\substack{a<b\\r<s}} \frac{\langle\Psi_0|\hat{H}|\Psi_{ab}^{rs}\rangle\langle\Psi_{ab}^{rs}|\hat{H}|\Psi_0\rangle}{\langle\Psi_{ab}^{rs}|\hat{H}-V_0|\Psi_{ab}^{rs}\rangle} = \sum_{\substack{a<b\\r<s}} E_{corr}\binom{rs}{ab} \tag{2.3.2.7}$$

where $E_{corr}\binom{rs}{ab}$ is the contribution of the double excitation $|\Psi_{ab}^{rs}\rangle$ to the approximate correlation energy. E_{corr} of (2.3.2.7) can be calculated easily, therefore it can be used for determining the configurations that are important in the expansion.

As discussed above, the Configuration Interaction approximation uses the Hartree-Fock orbitals for the construction of the different determinants. These orbitals are frozen in the above approximation, hence only the determinant coefficients are optimized. In order to increase the flexibility of the wavefunction, the relaxation of the orbitals has to be considered as well. The Multiconfiguration Self-Consistent Field (MCSCF) method does take into account the optimization of spin orbitals. Thus the MCSCF wavefunction is a truncated Configuration Interaction expansion:

$$|\Psi_{MCSCF}\rangle = \sum_I c_I|\Psi_I\rangle \tag{2.3.2.8}$$

in which both the expansion coefficients, c_I and the orthonormal orbitals contained in $|\Psi_I\rangle$ are optimized. For a closed-shell system, if only one determinant is included in the expansion (2.3.2.8), the MCSCF method becomes identical to HF. The general equations that has to be solved to obtain the MCSCF wavefunction are significantly more complicated than the Hartree-Fock equations.

Size-consistency, an important property of electronic structure approximations, can be proved to be valid for the HF and the full Configuration Interaction methods. However the truncated versions of the latter approach lack this feature.

Further methods of the next subsections of this section will introduce size-consistent approximations (perturbative and coupled pair approaches) however the prize to pay is that they are not variational, namely their energy can be lower than the exact one.

2.3.3 Coupled cluster theory

In the last two decades, Coupled Cluster (CC) methods became a very important family of quantum chemistry approaches that account for electron correlation. The wavefunction ansatz is given by the effect of an exponential operator on a reference function (usually the HF ground state) [26]:

$$|\varphi_0^{CC}\rangle = e^{\hat{\mathcal{T}}}|\Psi_0\rangle \tag{2.3.3.1}$$

where the $\hat{\mathcal{T}}$ operator has the following form using the notations of second quantization:

$$\hat{\mathcal{T}} = \hat{\mathcal{T}}_1 + \hat{\mathcal{T}}_2 + \hat{\mathcal{T}}_3 + \cdots = \sum_{ar} t_a^r \{\hat{a}_r^\dagger \hat{a}_a\} + \frac{1}{4}\sum_{abrs} t_{ab}^{rs} \{\hat{a}_r^\dagger \hat{a}_a \hat{a}_s^\dagger \hat{a}_b\} + \frac{1}{36}\sum_{abcrst} t_{abc}^{rst} \{\hat{a}_r^\dagger \hat{a}_a \hat{a}_s^\dagger \hat{a}_b \hat{a}_t^\dagger \hat{a}_c\} + \cdots \tag{2.3.3.2}$$

with $\hat{a}_r^\dagger$ and $\hat{a}_a$ being the creation and annihilation operators, respectively. For example $\{\hat{a}_r^\dagger \hat{a}_a\}$ removes the occupied spin orbital with index a from the determinant and replaces it with an unoccupied spin orbital of index r. As a result, this operation describes the excitation of an electron between the mentioned orbitals. In (2.3.3.2) the t parameters are the so-called cluster amplitudes and in principle all possible excitations can be considered. In this case the Full-CC approximation is obtained which is computationally very expensive for systems having more than a couple of electrons. One of the great advantages of CC methods (versus Configuration Interaction and its truncated versions) originates from the use of the exponential operator. Using the power series of the exponential operator, e.g. quadruple excitations have $\frac{1}{2}\hat{\mathcal{T}}_2^2$ contributions, namely higher order excitations can be accounted for without increasing the number of parameters.

The equations of motion can be derived by inserting (2.3.3.2) into the Schrödinger equation. After multiplying from the left by $e^{-\hat{\mathcal{T}}}$ and then successively projecting on the different excited determinants, we obtain:

$$\langle \Psi_0 | e^{-\hat{\mathcal{T}}} (\hat{H} - V_0) e^{\hat{\mathcal{T}}} | \Psi_0 \rangle = E_{corr} \tag{2.3.3.3}$$

$$\langle \mathbf{\Psi} | e^{-\hat{\mathcal{T}}} (\hat{H} - V_0) e^{\hat{\mathcal{T}}} | \Psi_0 \rangle = 0 \tag{2.3.3.4}$$

where $\mathbf{\Psi}$ includes all the considered excited determinants, thus we have one equation for each determinant. In practical calculations truncated wavefunctions have relevance only. Widely used versions of the CC method are CCSD ($\hat{\mathcal{T}} = \hat{\mathcal{T}}_1 + \hat{\mathcal{T}}_2$, Singles and Doubles), CCSDT ($\hat{\mathcal{T}} = \hat{\mathcal{T}}_1 + \hat{\mathcal{T}}_2 + \hat{\mathcal{T}}_3$, Singles Doubles and Triples), CCSDTQ ($\hat{\mathcal{T}} = \hat{\mathcal{T}}_1 + \hat{\mathcal{T}}_2 + \hat{\mathcal{T}}_3 + \hat{\mathcal{T}}_4$, Singles Doubles Triples and Quadruples) and CCD ($\hat{\mathcal{T}} = \hat{\mathcal{T}}_2$, Doubles).

It is important to emphasize that CC methods are size-consistent due to the exponential ansatz, namely the energy of a system consisting of noninteracting particles is equal to the sum of the energies of the individual members.

2.3.4 Perturbative approach

In perturbation theory the total Hamiltonian of the system is partitioned into two terms: a zero-order part, $\hat{H}_0$, for which the eigenfunctions and eigenvalues are known, and a perturbation, $\hat{\Omega}$. Then the exact energy is expressed as an infinite sum of contributions of increasing complexity. The expressions for these terms contain the eigenvalues of $\hat{H}_0$ and matrix elements of the perturbation between the eigenfunctions of $\hat{H}_0$. If we choose $\hat{H}_0$ appropriately, then $\hat{\Omega}$ is small and the perturbation expansion converges quickly.

In this section I will introduce the basic concepts of the Rayleigh-Schrödinger perturbation theory (RSPT). Since we are interested in the correlation energy, a reasonable choice for $\hat{H}_0$ is the Hartree-Fock Hamiltonian. RSPT with this choice was first applied to N-electron systems by C. Møller and M. S. Plesset and therefore sometimes is referred to as Møller-Plesset perturbation theory (MPPT) [27].

The problem to solve is the following [26]:

$$\hat{H}|\varphi_i\rangle = (\hat{H}_0 + \hat{\Omega})|\varphi_i\rangle = \mathcal{E}_i|\varphi_i\rangle \tag{2.3.4.1}$$

where the eigenfunctions and eigenvalues of $\hat{H}_0$ are known:

$$\hat{H}_0|\Psi_i^{(0)}\rangle = V_i^{(0)}|\Psi_i^{(0)}\rangle \quad . \tag{2.3.4.2}$$

If $\hat{\Omega}$ is small, we expect that $|\varphi_i\rangle$ and $\mathcal{E}_i$ are close to $|\Psi_i^{(0)}\rangle$ and $V_i^{(0)}$, respectively. By introducing an ordering parameter λ (which will be equated to unity), it is possible to derive a procedure which can systematically improve the unperturbed eigenfunctions and

eigenvalues of $\hat{H}_0$:

$$\hat{H} = \hat{H}_0 + \lambda\hat{\Omega} \quad . \tag{2.3.4.3}$$

After expanding the exact eigenvalues and eigenfunctions in terms of λ, we get:

$$\mathcal{E}_i = V_i^{(0)} + \lambda V_i^{(1)} + \lambda^2 V_i^{(2)} + \cdots \tag{2.3.4.4}$$

$$|\varphi_i\rangle = |\Psi_i^{(0)}\rangle + \lambda|\Psi_i^{(1)}\rangle + \lambda^2|\Psi_i^{(2)}\rangle + \cdots \quad . \tag{2.3.4.5}$$

Substituting (2.3.4.4) and (2.3.4.5) into (2.3.4.1) and equating the coefficients of λ^n, we find a set of equations for the different energy and wavefunction contributions. Projecting each of these equations on $\langle\Psi_i^{(0)}|$ and using the intermediate normalization:

$$\langle\Psi_i^{(0)}|\Psi_i^{(n)}\rangle = 0 \qquad\qquad n = 1, 2, 3, ... \tag{2.3.4.6}$$

the following expressions are obtained for the energy contributions up to third order:

$$V_i^{(0)} = \langle\Psi_i^{(0)}|\hat{H}_0|\Psi_i^{(0)}\rangle \tag{2.3.4.7}$$

$$V_i^{(1)} = \langle\Psi_i^{(0)}|\hat{\Omega}|\Psi_i^{(0)}\rangle \tag{2.3.4.8}$$

$$V_i^{(2)} = \langle\Psi_i^{(0)}|\hat{\Omega}|\Psi_i^{(1)}\rangle \tag{2.3.4.9}$$

$$V_i^{(3)} = \langle\Psi_i^{(0)}|\hat{\Omega}|\Psi_i^{(2)}\rangle \quad . \tag{2.3.4.10}$$

It is seen that the zero-order energies are simply the energies of the unperturbed problem, while the first-order contributions are diagonal matrix elements of the perturbation between the eigenfunctions of the unperturbed problem. However, beyond first order we need the different wavefunction corrections as well, for the calculation of the energy terms.

In order to determine the first, second, third, ... etc. order wavefunction corrections (and correspondingly the second, third, fourth, ... etc. order energy corrections) one has to turn to the previously mentioned set of equations (obtained after equating the coefficients of λ's) and carry out some substitutions and expansions consecutively.

In the end, the second and third order energy terms will have the following forms:

$$V_i^{(2)} = {\sum_n}' \frac{|\langle\Psi_i^{(0)}|\hat{\Omega}|\Psi_n^{(0)}\rangle|^2}{V_i^{(0)} - V_n^{(0)}} \tag{2.3.4.11}$$

$$V_i^{(3)} = {\sum_{nm}}' \frac{\langle\Psi_i^{(0)}|\hat{\Omega}|\Psi_n^{(0)}\rangle\langle\Psi_n^{(0)}|\hat{\Omega}|\Psi_m^{(0)}\rangle\langle\Psi_m^{(0)}|\hat{\Omega}|\Psi_i^{(0)}\rangle}{(V_i^{(0)} - V_n^{(0)})(V_i^{(0)} - V_m^{(0)})} - V_i^{(1)}{\sum_n}' \frac{|\langle\Psi_i^{(0)}|\hat{\Omega}|\Psi_n^{(0)}\rangle|^2}{(V_i^{(0)} - V_n^{(0)})^2} \quad . \tag{2.3.4.12}$$

The prime on the summation serves as a reminder that the term n=i (and m=i) is excluded. Higher order terms can also be derived, however in practical calculations mostly second and third order perturbative approximations are applied. A benefit of RSPT is that it is size-consistent, however as mentioned above, not variational. Unfortunately this method is only applicable in the case of small perturbations.

2.4 Nuclear dynamics

In quantum molecular dynamics, the aim is to directly solve the time-dependent Schrödinger equation for the nuclear motion on the coupled surfaces for the starting conditions appropriate to an experiment. In general, the equation to be solved can be written (using atomic units) [6]:

$$i\frac{\partial}{\partial t}\chi(\vec{R},t) = \hat{H}\chi(\vec{R},t) \quad . \tag{2.4.1}$$

Here the nuclear Hamiltonian, $\hat{H}$ (defined in (2.1.12) or (2.1.15)) can either be in the adiabatic or in the diabatic form and the components of χ correspond to the wavefunctions on the different electronic states. The most direct way to solve this equation is to express $\hat{H}$ and χ in a basis set. Assuming f nuclear degrees of freedom and n_k (k=1, ... f) basis functions, ϕ_{j_k} on the k^{th} degree of freedom, R_k, the component of the wavefunction in a certain electronic state, q can be expanded as follows:

$$\chi^{(q)}(\vec{R},t) = \sum_{j_1=1}^{n_1} \cdots \sum_{j_f=1}^{n_f} B^{(q)}_{j_1 \ldots j_f}(t)\phi^{(1)}_{j_1}(R_1)\cdots\phi^{(f)}_{j_f}(R_f) \tag{2.4.2}$$

where B contains the time-dependent coefficients of the time-independent basis functions. Inserting (2.4.2) into (2.4.1) and applying the variational principle, we obtain the following equation for the coefficients [28]:

$$i\frac{d}{dt}B_I = \sum_J H_{IJ}B_J \tag{2.4.3}$$

where

$$H_{IJ} = \langle \phi^{(1)}_{i_1}\cdots\phi^{(f)}_{i_f}|\hat{H}|\phi^{(1)}_{j_1}\cdots\phi^{(f)}_{j_f}\rangle \tag{2.4.4}$$

and the composite indices, J=$(j_1, j_2, ...j_f)$ were introduced. Eq. (2.4.3) is a very simple first-order differential equation with constant coefficients. It has the formal solution (for

time-independent Hamiltonians):

$$B(t) = e^{-i\hat{H}t} B(0) \quad . \tag{2.4.5}$$

However, (2.4.3) is difficult to solve because of the large number of coupled equations. One of the simplest propagation methods is the time-dependent Hartree approach (TDH). In this case the wavefunction is a simple product of time-dependent basis functions, one for each degree of freedom:

$$\chi(\vec{R}, t) = b(t)\phi_1(R_1, t) \cdots \phi_f(R_f, t) = b(t)\Phi(t) \quad . \tag{2.4.6}$$

This representation is not unique (because $\phi_1\phi_2 = (\phi_1/c) \cdot (\phi_2 \cdot c)$ for any complex number c$\neq$ 0). To arrive at unique equations of motion one has to introduce constraints, which remove the non-uniqueness but do not narrow the variational space. Such a constraint is:

$$i \left\langle \phi_k(t) | \dot{\phi}_k(t) \right\rangle = g_k(t) \tag{2.4.7}$$

with g_k real (for the sake of norm conservation), but otherwise arbitrary. Applying the same steps as before, we obtain the equations of motion, now not only for the coefficient b, but for the basis functions as well:

$$i \, \dot{\phi}_k = (\mathcal{H}^{(k)} - E + g_k)\phi_k \tag{2.4.8}$$

$$i \, \dot{b} = (E - \sum_{k=1}^{f} g_k) b \tag{2.4.9}$$

with

$$E = \left\langle \Phi | \hat{H} | \Phi \right\rangle \quad \text{and} \quad \mathcal{H}^{(k)} = \left\langle \Phi^{(k)} | \hat{H} | \Phi^{(k)} \right\rangle \quad . \tag{2.4.10}$$

Here $\Phi^{(k)}$ is a product of the ϕ_j functions where j=k is omitted (j=1,2, ... (k-1), (k+1), ... f). Concerning g_k, it can be proved that its various choices merely shift phase-factors from b to ϕ_k and vice-versa.

The TDH solution is approximate because of the very restricted form of the wavefunction. To overcome the limitations of TDH, one can turn to a multi-configurational ansatz and write the WF as:

$$\chi(\vec{R}, t) = \sum_{j_1=1}^{n_1} \cdots \sum_{j_f=1}^{n_f} B_{j_1 \ldots j_f}(t) \phi_{j_1}^{(1)}(R_1, t) \cdots \phi_{j_f}^{(f)}(R_f, t) \quad . \tag{2.4.11}$$

Following a procedure very similar to the one of the TDH case, the equations of motion for the multi-configuration time-dependent Hartree (MCTDH) situation can be derived. These are of the following (more complicated) form [28]:

$$i\,\dot{B}_J = \sum_L \left\langle \Phi_J | \hat{H} | \Phi_L \right\rangle B_L - \sum_{k=1}^{f} \sum_{l=1}^{n_k} \hat{g}^{(k)}_{j_k l} B_{J^k_l} \tag{2.4.12}$$

$$i\,\dot{\boldsymbol{\phi}}^{(k)} = (\hat{g}^{(k)}\mathbf{1})\boldsymbol{\phi}^{(k)} + (1-\hat{P}^{(k)})\{\hat{\boldsymbol{\rho}}^{(k)^{-1}}\left\langle \hat{H} \right\rangle^{(k)} - \hat{g}^{(k)}\mathbf{1}\}\boldsymbol{\phi}^{(k)} \tag{2.4.13}$$

where $\boldsymbol{\phi}^{(k)}$ contains the basis functions of the k^{th} DOF, $\hat{P}^{(k)}$ is the MCTDH projector, $\hat{\boldsymbol{\rho}}$ is a density matrix and $\left\langle \hat{H} \right\rangle^{(k)}$ defines the mean-field with respect to the so-called single-hole functions. A full account of the technical aspects of the above method can be found in e.g. Refs. [28, 29]. Here I would only like to notice that the multi-configuration time-dependent Hartree method developed by the Heidelberg group [30, 31] is possibly the most powerful and flexible wavepacket propagation method.

One of its major advantage is that a discrete variable representation (DVR) basis is used. These are orthonormal functions that approximate delta functions on points in space. The wavefunction is then effectively represented on a set of grid points. The potential operator is simple to evaluate as it is diagonal in this basis. At the same time the construction of the basis allows easy evaluation of the kinetic energy operator integrals. The kinetic energy is evaluated using a Fast-Fourier Transform (FFT). Combined with powerful integration schemes, the grid-based methods have become the standard approaches for wavepacket propagation. The method is not only easy to implement, but the results are easy to visualize. The wavepacket is initially set up on the grid and, driven by the system Hamiltonian, flows through space. Properties of interest can of course then be extracted from it as a function of time. The most important dynamical features are discussed in the next subsection.

2.4.1 Dynamical properties

In this subsection a short overview of the most important dynamical properties will be given. During the course of time evolution, wavepackets are propagated on the electronic potential energy surfaces. Starting from a given initial wavefunction at t=0, we can investigate the extent that the wavefunction at time t is identical to the initial function. This

can be done by evaluating the overlap between $\chi(t=0)$ and $\chi(t)$ which is measured by the autocorrelation function:

$$C(t) = |\langle \chi(\vec{R}, t=0) | \chi(\vec{R}, t) \rangle| \quad . \tag{2.4.1.1}$$

The population on a diabatic surface belonging to a certain electronic state can be determined as the norm of the wavefunction after projection. For a certain electronic state, q the diabatic state population is then given by:

$$L_{diab}^{(q)}(t) = \langle \chi_{diab}^{(q)}(\vec{R}, t) | \chi_{diab}^{(q)}(\vec{R}, t) \rangle \quad . \tag{2.4.1.2}$$

If we have n electronic surfaces, then the sum of the diabatic state populations of the individual states will always give 1. One more dynamical feature of a molecuar system which is worth mentioning is the photoabsorption spectrum. Perhaps the easiest experimental observable to obtain is a photoabsorption spectrum. The absorption spectrum, $\sigma(\omega)$, can be calculated from the Fourier transform of the previously defined autocorrelation function [31]:

$$\sigma(\omega) \propto \omega \int_{-\infty}^{\infty} dt C(t) e^{i(V_0+\omega)t} \tag{2.4.1.3}$$

with V_0 being the ground state energy. In the result section of chapter VI., dynamical calculations for a real system, the butatriene molecule will be presented in terms of the above-mentioned dynamical properties as a function of time.

3. Conical intersections and the Berry phase

In this chapter I am intending to give an overview on the relation of conical intersections and the so-called geometric phase effect. The latter one is an interesting phenomena that carries evidence on the presence of a conical intersection in the system. It was first pointed out by Longuet-Higgins and Herzberg that a real electronic wavefunction changes sign when traversing around a conical intersection [21, 22]. Mead and Truhlar incorporated this geometric phase effect into a single electronic state problem and Berry generalized the theory. Because of his work this effect is often called the Berry phase [23]. Since the total wavefunction must be single-valued, the electronic wavefunction in the adiabatic representation should be multiplied by a phase factor ensuring that the total wavefunction remains single-valued. As a consequence, the geometric phase can affect the nuclear dynamics even when a single potential energy surface is considered. The geometric phase effect can be considered as a signature of the conical intersections and its presence is a proof that a true conical intersection has been found [8].

The first section of this chapter discusses the topological line integral technique, an effective method for calculating the Berry phase in situations, where the two electronic states under investigation can be considered decoupled from the remaining part of the manifold. In section 3.2 my own results (based on publication [II]) are presented for the H_2CN molecule. Here the value of the Berry phase is determined for several situations giving evidence that two CIs are formed upon the distortion from the linear arrangement of the molecule.

3.1 The line integral method and the Berry phase

The topological line integral technique makes possible the calculation of the topological or Berry phase using nonadiabatic coupling terms obtained by e.g. *ab initio* calculations. A very detailed description of this method is published in Refs. [32, 33], here I would like to give only a brief summary of its main steps.

As discussed already in section 2.1, the nonadiabatic coupling vector, $\vec{\tau}$ appears in the kinetic energy operator resulting the so-called momentum coupling (see the dressed kinetic energy term in eq. (2.1.12)). Because of the singularity of $\vec{\tau}$ at CIs, it is desirable to

transform (2.1.12) to another form, in which the coupling is in the potential term. To do so, one has to find the proper adiabatic-to-diabatic transformation, $\hat{A}$. After inserting the diabatic wavefunction (2.1.13) into (2.1.12) one finds the following criterion for $\hat{A}$ to be fulfilled [7, 25]:

$$(\nabla\hat{A} + \vec{\tau}\hat{A}) = 0 \tag{3.1.1}$$

where

$$\vec{\tau}_{ij}(s) = \left\langle \xi_i | \nabla \xi_j \right\rangle \tag{3.1.2}$$

is the well-known nonadiabatic coupling vector. It can be proved that the solution of (3.1.1) can be written in the form:

$$A(s_0, s) = \wp \quad \exp\left(- \int_{s_0}^{s} \vec{\tau}(s')\ \mathrm{d}\vec{s'} \right) A(s_0) \tag{3.1.3}$$

where $\wp$ is the ordering operator and the integration is carried out along a line, Γ between s_0 and s. In the special case, when two electronic states (say a P subspace) can be considered decoupled from the remaining part of the manifold (the complementer Q space), namely $\vec{\tau}_{ij} \approx 0 \quad (i\epsilon P \quad \text{and} \quad j\epsilon Q)$, the ADT matrix has the simple form:

$$A(s_0, s) = \begin{pmatrix} \cos\gamma_{12}(s) & -\sin\gamma_{12}(s) \\ \sin\gamma_{12}(s) & \cos\gamma_{12}(s) \end{pmatrix} \tag{3.1.4}$$

where γ_{12} is the ADT angle calculated according to:

$$\gamma_{12}(s) = \int_{s_0}^{s} \vec{\tau}_{12}(s')\ \mathrm{d}\vec{s'} \quad . \tag{3.1.5}$$

Here $\vec{\tau}_{12}$ is evaluated using the adiabatic ξ_1 and ξ_2 electronic wavefunctions.
A similar expression is given for the Berry phase, α_{12} for a closed contour, Γ:

$$\alpha_{12} = \oint_{\Gamma} \vec{\tau}_{12}(s)\ \mathrm{d}\vec{s} \quad . \tag{3.1.6}$$

It is important to notice here that our assumption that two electronic states are separated within the manifold is indeed justified in the vicinity of a conical intersection. The validity of this guess will be demonstrated later by numerical analysis as well.
As mentioned already, the corresponding adiabatic states change sign while being transported continuously along a closed contour enclosing the point of intersection. As a consequence of the sign change, it can be proved that the value of the Berry phase is:

$$\alpha_{12} = \pi \times \begin{cases} 2n+1 & \text{if } \Gamma \text{ encircles odd number of CIs} \\ 2n & \text{if } \Gamma \text{ encircles even number of CIs} \end{cases} \qquad n = 0, \pm 1, \pm 2... \quad . \quad (3.1.7)$$

In other words, for a single CI case the value of the Berry phase is equal to π. Previously it has been shown that this technique can be applied for Renner-Teller (see section 4.1) intersections as well [34] and the value of the topological phase for that situation is equal to 2π. It is worth noting here that α=2π does not ensure that the path surrounds a Renner-Teller intersection, it could also be the fingerprint of two conical intersections. To clarify the source of α=2π one needs to study the order of the degeneracy or (if there are two CIs) to find a - smaller - path for which the topological phase is only π.

3.2 Results for the H_2CN molecule

A couple of years ago an interesting connection between CIs and RT intersections has been revealed [34–38]. Halász and co-workers have found that CIs can be formed in polyatomic systems exhibiting the RT effect when these molecules are bent away from their linear configuration losing both the axis, and planar symmetries. Recently, several valuable new results have been achieved in this subject. Among other things it has been proved both analytically [39] and numerically [40] that not only one but two conical intersections are formed after losing the Renner-Teller character of the molecule. A significant part of the results refers to the $C_2H_2^+$ molecule, for which even the migration of the CIs has been revealed [41]. Some other systems, including the non-symmetric H_2CN molecule have also been investigated. In the first numerical calculations there was no success to find a pair of CIs in the molecular plane for this system [42–44]. Later Bene and colleagues revealed the existence of a pair of CIs outside the plane of the molecule and provided a good estimate for the positions of the pair of degeneracies [45].

Based on this line, our aim was to determine the positions of CIs more accurately and to calculate nonadiabatic coupling terms and the corresponding topological phase for the first time surrounding only a single CI from the pair of CIs.

Our results clearly confirm the fact that after losing the Renner-Teller character in a

molecular system always two single CIs are created. These two aligned CIs can be located either in the molecular plane or outside of it, the corresponding nonadiabatic coupling terms and Berry phase can always be calculated along a closed contour enclosing only one of the CIs. Since the Berry phase [23] can be considered as a clear fingerprint of conical intersections, its presence in a molecular system is a proof that a true conical intersection has been found.

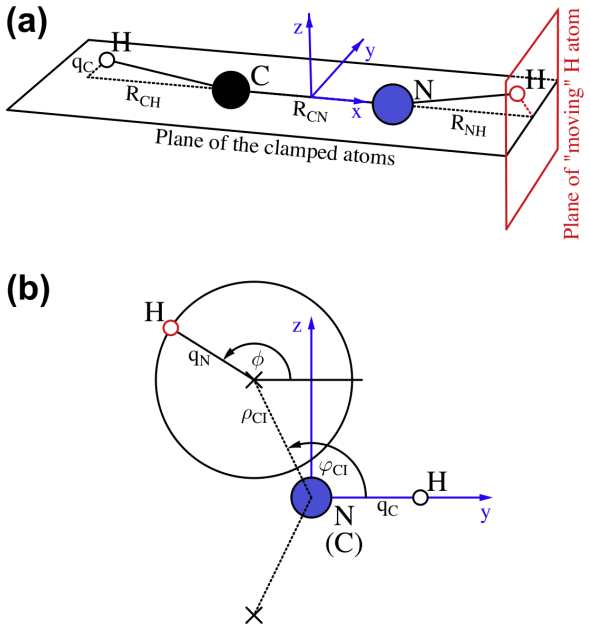

Figure 1: Configuration of the H_2CN molecule. (a) The nonlinear arrangement is obtained by displacing the H atoms perpendicular to the original molecular axis. (b) The position of one of the CIs is characterized by the φ_{CI} and ρ_{CI} coordinates, while the other CI is located symmetrically on the other side of the plane. ϕ and q_N are used to describe the position of the 'moving' H atom in the NACT and Berry phase calculations.

Calculations of the NACTs and the positions of the CIs were both carried out at the state-averaged CASSCF [46–50]/6-311G** level of theory using an active space with all the 11 valence electrons distributed on ten orbitals. The positions of CIs were determined for two different displacements of the clamped H atom: q_C=0.01 Å and q_C=0.1 Å (Fig. 1(a)).

For q_C=0.01 Å we found that the CIs are positioned at φ_{CI}=±116.1° with ρ_{CI}=0.012 Å, while for the larger displacement with q_C=0.1 Å the corresponding values are φ_{CI}=±115.6° and ρ_{CI}= 0.12 Å (Fig. 1(b)). The ± signs indicate that one of the CIs is located above the

plane of the molecule (+) while the other one is placed under this plane (–).

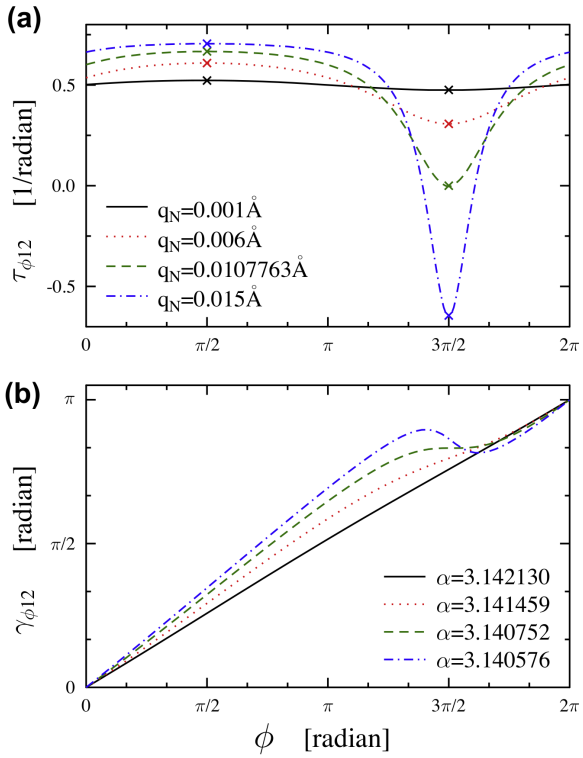

Figure 2: (a) *Ab initio* nonadiabatic coupling terms and (b) the adiabatic-to-diabatic transformation angles are presented for four different paths surrounding only one CI ($q_N < 2\rho_{CI} \cdot \sin\varphi_{CI}$). Here the value of q_C is equal to 0.01 Å and α is the value of the topological or Berry phase. See Fig. 1(b) for the definition of the ϕ angle and the q_N radius. The lines represent *ab initio* results, while the markers denote the results of the vector-algebra model for ϕ=$\pi/2$ and ϕ=$3\pi/2$ situations.

After that we calculated the nonadiabatic coupling terms and the adiabatic-to-diabatic transformation angles. Performing the integration over a closed contour, this latter quantity provides the value of the topological or Berry phase. Figures 2-5 show the results for these quantities for several different situations. In all figures the center of the circles along which the above-mentioned quantities were calculated is the position of the CI which is placed above the xy plane. In Fig. 2(a) the nonadiabatic coupling terms and in Fig. 2(b) the adiabatic-to-diabatic transformation angles with the corresponding Berry phases are displayed for the displacement of q_C=0.01 Å and for four different q_N radii. We notice that in all the studied cases the value of the Berry phase is equal to π as expected since these circles surround only a single CI from the evolved pair of CIs. A different situation is encountered in case of

larger q_N radius (Fig. 3). Here the radii q_N=0.025 Å and q_N=0.040 Å were large enough to encircle both CIs from the pair of CIs. The value of the Berry phases are ca. 2π as is expected for cases where the circles surround two conical intersections.

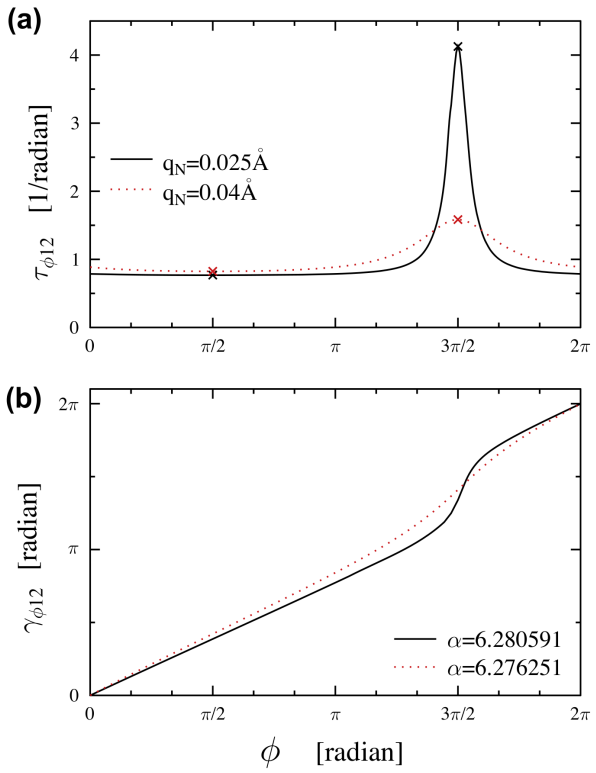

Figure 3: (a) *Ab initio* nonadiabatic coupling terms and (b) the adiabatic-to-diabatic transformation angles are presented for two different paths surrounding both CIs ($q_N > 2\rho_{CI} \cdot \sin\varphi_{CI}$). For more details see Fig. 2.

Fig. 4 and 5 present similar results, but calculated for q_C=0.1 Å. It is noticed that the characteristic shapes of these figures are very similar to those displayed in Fig. 2 and 3, except that, in the present case the values of the Berry phases are differing more from π or 2π. This larger deviation from the expected values only indicates that the two-state approximation is less accurate for circles surrounding a larger area (as we are not so close to the singularity of the NACT between the two studied electronic states, the couplings to other states start to play a role).

It can be noticed that the smallest radius provides a nearly flat NACT curve, while increasing the value of q_N, a (negative) peak starts to develop around ϕ=$3\pi/2$. If there are several CIs between the same two states using the model developed in Ref. [51] one can

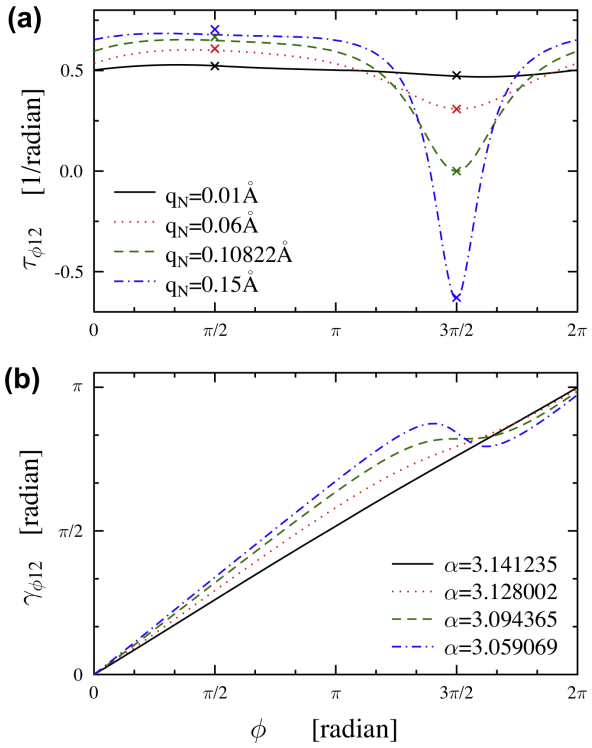

Figure 4: (a) *Ab initio* nonadiabatic coupling terms and (b) the adiabatic-to-diabatic transformation angles are presented for four different paths surrounding only one CI ($q_N < 2\rho_{CI} \cdot \sin\varphi_{CI}$). Here the value of q_C is equal to 0.1 Å and α is the value of the topological or Berry phase. See Fig. 1(b) for the definition of the ϕ angle and the q_N radius. The lines represent *ab initio* results, while the markers denote the results of the vector-algebra model for ϕ=$\pi/2$ and ϕ=$3\pi/2$ situations.

calculate the NACT with a simple vector-algebra from the so called 'virgin' distribution of the CIs which is the angular NACT around the CI for an extremely small radius. As for the smallest studied radii we have a nearly flat shape and because of the symmetry of the system here we can assume that the 'virgin' distribution is flat for both CIs: $\tau^v_{\phi 12}(q,\phi)= 0.5$. According to the model, the real NACT could be approximated by the vectorial sum of the 'virgin' fields 'generated' by the two CIs. For a given point a CI 'generates' a NACT which is perpendicular to the segment between the point and the CI and its absolute value is inversely proportional to the distance of this segment: $|\vec{\tau}^v_{12}|=\tau^v_{\phi 12}(q,\phi)/q$. When the studied point is on the line connecting the two CIs (ϕ=$\pi/2$ or ϕ=$3\pi/2$) the 'generated' NACT vectors of the two CIs are parallel and we only need to do some simple algebra with the distances from

the two CIs:

$$\tau^{m}_{\phi 12} = 0.5 + \frac{0.5 \cdot q_N}{(q_N + 2 \cdot \rho_{CI} \cdot \sin\varphi_{CI} \cdot \sin\phi)} \quad . \tag{3.2.1}$$

Here the first term comes from the CI, which is the center of the circle and the denominator of the second term is the distance of the actual point from the other CI ($\sin\phi = \pm 1$ as $\phi = \pi/2$ or $\phi = 3\pi/2$). These predicted values from the model are displayed in panels (a) of Figs. 2-5 with markers. In the case of $\phi = 3\pi/2$ the predicted angular NACT will have a singularity at $q_N = 2\rho_{CI} \cdot \sin\varphi_{CI}$.

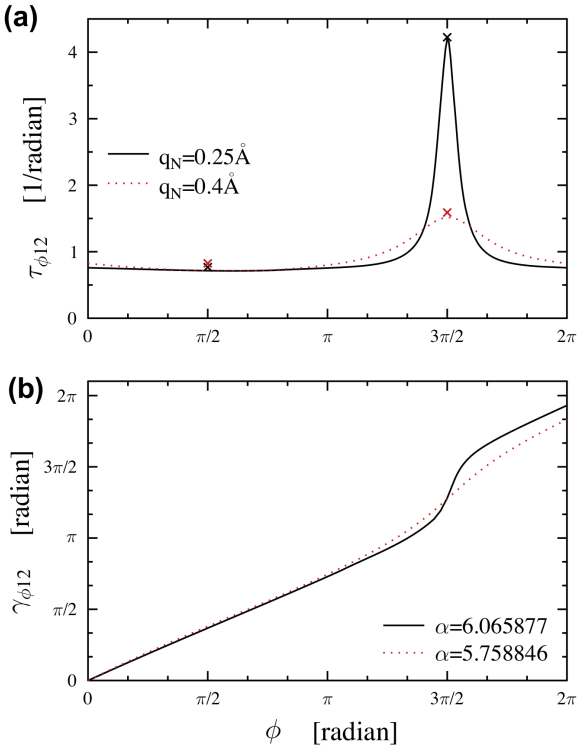

Figure 5: (a) *Ab initio* nonadiabatic coupling terms and (b) the adiabatic-to-diabatic transformation angles are presented for two different paths surrounding both CIs ($q_N > 2\rho_{CI} \cdot \sin\varphi_{CI}$). For more details see Fig. 4.

This singularity gives an explanation for the pronounced single peaks around $\phi = 3\pi/2$ in the calculated NACTs. To make a more detailed comparison with the *ab initio* calculations, we have also used the model to calculate the NACT along complete paths. The curves are displayed in Fig. 6. The parameters for these model calculations are the distance of the two CIs and the radius of the studied circle. To make the results more comparable to the *ab*

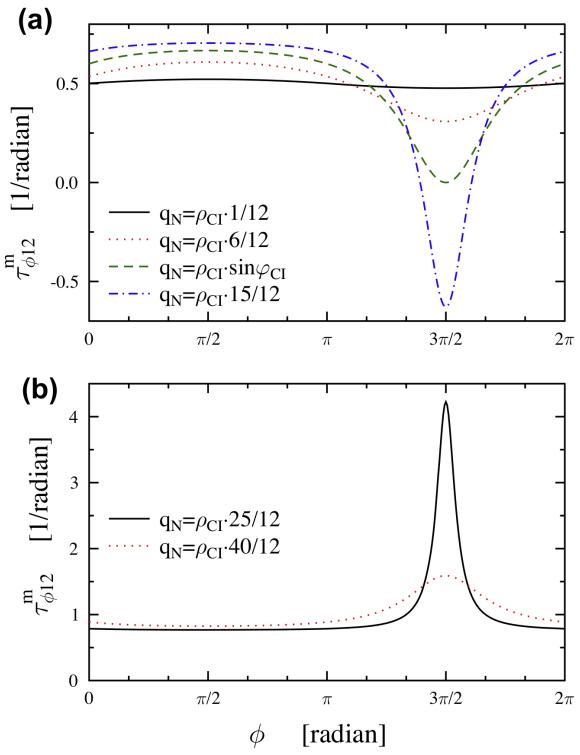

Figure 6: Nonadiabatic coupling terms calculated by vector-algebra from the flat 'virgin' distribution of the two CIs for φ^m_{CI}=115.6° and different radii. (a) The path surrounds only one CI ($q_N < 2\rho_{CI} \cdot \sin\varphi^m_{CI}$). (b) The path surrounds both CIs ($q_N > 2\rho_{CI} \cdot \sin\varphi^m_{CI}$).

initio calculations, we described these parameters in terms of ρ_{CI} and φ_{CI}. We expressed the radii of the circles in terms of ρ_{CI} in order to get a more general result comparable to *ab initio* calculations with both studied q_C values. For the value of φ_{CI} in the model calculations we chose φ_{CI}=115.6° in order to make it clear that the larger deviations from the model in the case of q_C=0.1 Å are not related to the wrong parametrization of the model. The predictions of the model are fitting well for the *ab initio* results, especially for the case of q_C=0.01 Å in spite of the minor difference (ca. 0.5°) in the parameter of φ_{CI}. The slightly higher deviation from the model calculations for the case of q_C=0.1 Å (see, e.g. the distance of the *ab initio* results from the markers at ϕ=π/2 on Fig. 5(a)) is related to the larger area surrounded by the paths which implies that the two-state approximation is less accurate and the influence of other CIs - not considered here - are not so negligible as in case of the smaller q_C.

In the topological study carried out for the H_2CN molecule, my contribution was multiple: After localizing the conical intersections in the system, I calculated the corresponding *ab initio* nonadiabatic coupling terms along the closed circular contours. For the calculation of the adiabatic-to-diabatic transformation angles and related Berry phases, I wrote a program code implementing the topological line integral method. In this code, the processing of the pure NACTs (including the treatment of the sign changes of the NACTs) had to be considered as well.

4. Jahn-Teller and Renner-Teller intersections

The Jahn-Teller (JT) effect describes the distortion of a non-linear molecule if two electronic states are degenerate. The effect is named after Hermann Arthur Jahn and Ede Teller, who proved the theorem using group theory [52]. The problem was first discussed in 1934 when E. Teller and Lev Landau had many discussions on the stability of the CO_2 molecule. Teller's student E. Renner showed that a linear molecule, which has degenerate electronic states, should be stable, but Landau had objections. His arguments were that in the degenerate electronic state the symmetry on which the degeneracy is based will be destroyed. Teller first showed that this is not true for collinear configuration of nuclei. But the question was if there are some other exceptions. Teller and Jahn proved that this is the only case [53]. The JT effect can be summarized in one sentence as follows: a geometrical configuration of a molecule in which the electronic states are degenerate cannot be stable (on symmetry grounds alone) unless when the configuration of nuclei is collinear.

In this chapter I am going to discuss the relation of Renner-Teller type and Jahn-Teller intersections (conical intersections induced by symmetry, as the involved electronic states belonging to the same irreducible representation are degenerate as long as the symmetry is present in the system). After introducing the basics of the Renner-Teller effect, a short argument will be given on the entanglement of the RT and JT degeneracies. As a result of the formulations, a coupling parameter, η is presented. Finally a numerical study is carried out for a tri-atomic system to demonstrate the viability of the theory. My own results concerning the Renner-Teller/Jahn-Teller $F+H_2$ system are presented in sections 4.3, 4.4 and they are based on publications [III] and [IV], respectively.

4.1 The Renner-Teller effect

In 1934, Renner published a detailed study of a linear polyatomic molecule, originally characterized by the z component of the electronic orbital angular momentum, $\Lambda\hbar$ (where $\Lambda \neq 0$) and by a nuclear angular momentum component, $l\hbar$ associated with the bending vibrations of the molecule, both defined with respect to the molecule axis (considered to be the z-axis) [24]. To be more specific, in this study Renner concentrated on those states

that split to become two (coupled) states when moving away from collinearity. Thus, if we consider e.g. a Π-state characterized by the quantum number $\Lambda = 1$ and a single eigenfunction, $\xi_{\Lambda=1}(\vec{s}_e|\vec{s})$, then after moving away from collinearity, one encounters two eigenfunctions, namely $\xi^{\pm}_{\Lambda=1}(\vec{s}_e|\vec{s})$ related to the two decoupled states (in this notation $\vec{s}_e$ and $\vec{s}$ stand for the collective electronic and nuclear coordinates, respectively).

Taking this model one step further and assuming the deviation from collinearity to be small enough (thus, the coordinate $\vec{s}$ is removed only slightly from the collinear arrangement) we can define two eigenfunctions, one symmetric and an antisymmetric with respect to the molecular plane. These functions are:

$$\xi_1 = \frac{1}{\sqrt{2}}(\xi^+_\Lambda + \xi^-_\Lambda) \quad \text{and} \quad \xi_2 = \frac{1}{\sqrt{2}i}(\xi^-_\Lambda - \xi^+_\Lambda) \quad . \tag{4.1.1}$$

Then the z component of the electronic orbital angular momentum operator is:

$$\left\langle \xi_1 | \hat{L}_z | \xi_2 \right\rangle \approx i\hbar\Lambda \quad . \tag{4.1.2}$$

If we consider cilindrical coordinates around the molecular z-axis with q denoting the radius (the extent that the system is removed from collinearity) and φ describing the angle around the axis, then we can make the following observation: rotating the electron system by a certain φ^* is equivalet to the rotation of the nuclei by $-\varphi^*$. This fact indicates that the z component of the electronic orbital angular momentum is proportional to the nonadiabatic coupling term corresponding to the rigid rotation around the axis (the φ component):

$$\tau_\varphi(q \to 0) = \left\langle \xi_1 | \frac{\partial}{\partial\varphi} \xi_2 \right\rangle_{q\to 0} = -\frac{i}{\hbar} \left\langle \xi_1 | \hat{L}_z | \xi_2 \right\rangle_{q\to 0} = \Lambda \quad . \tag{4.1.3}$$

Now using this NACT, one can calculate the Berry phase for Renner-Teller systems too. This can be done by applying the previously introduced line integral method. For a linear RT molecule the Berry phase is given by:

$$\alpha(\Gamma) = \oint_\Gamma \vec{\tau}(\vec{s})\, \mathrm{d}\vec{s} = \int_0^{2\pi} \tau_\varphi(q,\varphi)\, \mathrm{d}\varphi = 2\pi \tag{4.1.4}$$

where Γ is a closed circle around the RT axis. This result is in correspondence with the previously discussed topological (or Berry) phase for systems of this kind.

4.2 Coupling of RT and JT degeneracies

In this section I am going to introduce a theory for calculating the adiabatic-to-diabatic transformation angle (sec. 3.1) in a situation where a Renner-Teller system is entangled with Jahn-Teller intersections. With the help of ADT angles one can then derive diabatic potential energy surfaces and thus get insight into the dynamics of the molecular system. As a showcase example, the tri-atomic Renner-Teller F+H_2 system will be applied, for which the geometry arrangement is presented in Fig.7.

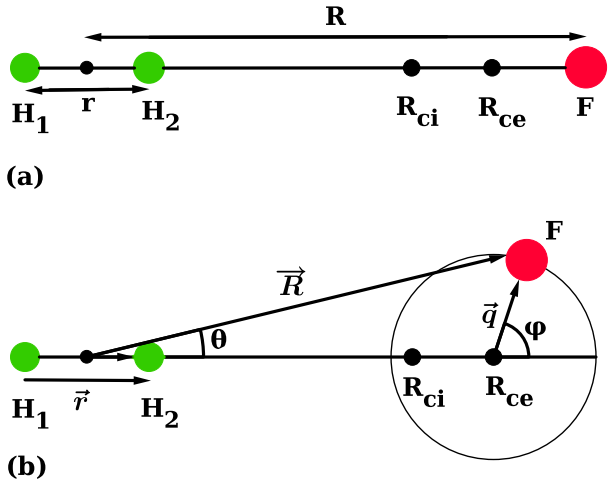

Figure 7: System of coordinates for F+H_2. R_{ci} is the point of (1,2) CI and R_{ce} is the center of all circular contours. Panel (a) depicts the linear RT arrangement, while in panel (b) the $(\vec{R}, \theta | r)$ and $(\vec{q}, \varphi | r)$ coordinates are compared.

Studies on the entanglement of RT and JT degeneracies were performed in the past for contours that surround the RT seam located along the collinear axis [36]. Our study is characterized by planar contours that intersect the collinear axis, thus forming a unique type of RT nonadiabatic coupling terms expressed in terms of Dirac-δ functions. Consequently, to calculate the required adiabatic-to-diabatic (mixing) angles, a new approach is developed. During this study the existence of a novel molecular parameter, η is revealed which yields the coupling between the RT and the JT NACTs. This parameter is found to be a pure number, $\eta = 2\sqrt{2}/\pi$ (and therefore independent of any particular molecular system) and is designated as Renner-Jahn coupling parameter (RJCP).

The planes under consideration are formed by the three atoms (a fluorine and two hydro-

gens in our case) and are parameterized via values of r, the interatomic distance of H_2. The ($\vec{R}$,θ) grid points describe the polar coordinates of the F atom with respect to the center of mass of the H_2 molecule on that plane.

The approach to be presented is based on three (or more) interacting electronic states and therefore requires treating the adiabatic-to-diabatic transformation matrices, A(s) rather than the ordinary ADT (mixing) angles, $\gamma(s)$. The literature contains numerous studies based on these matrices, also in the case when both RT and JT NACTs are incorporated in the ADT matrices [36, 37, 42, 43]. Their main shortcoming is that the ADT matrices are calculated for grids on a series of planes perpendicular to the collinear axis instead of the required grid on the tri-atomic plane (dynamical treatments are carried out on tri-atomic planes). In other words, those approaches demand intricate transformations from these numerous grids to the tri-atomic grid - a process that severely complicates the dynamical treatment.

In what follows, we suggest calculating the ADT matrices for the tri-atomic grid directly. Another reason for this choice is that, for each value of the vibrational coordinate r, such a plane contains all JT intersections, as well as the collinear axis (with all RT degeneracy points). Therefore the corresponding planar grid points are exposed to all the topological effects. As discussed in sec. 3.1, the A(s) transformation matrix can be obtained by solving the following differential equation:

$$\nabla A(s) + \tau(s)A(s) = 0 \tag{4.2.1}$$

where $\tau(s)$ is an antisymmetric matrix containing the above-mentioned NACTs and s represents the collection of internal nuclear coordinates. As detailed in sec. 2.1, by the proper adiabatic-to-diabatic transformation, $\tau(s)$ (which often contains singular elements) can be eliminated from the kinetic energy operator of the Schrödinger equation eventuating off-diagonal elements in the potential part. The relation between the diabatic and adiabatic potential matrices was given as follows:

$$W(s) = A(s)^{\dagger}V(s)A(s) \quad . \tag{4.2.2}$$

A possible way to solve (4.2.1) is as follows: Since A(s) is an orthogonal matrix, it can be presented in terms of Euler kind of angles and consequently its diagonality is guaranteed (for the sake of single-valuedness of the diabatic potential W(s)) if and only if these angles, at the end of a closed contour, become integer multiples of π.

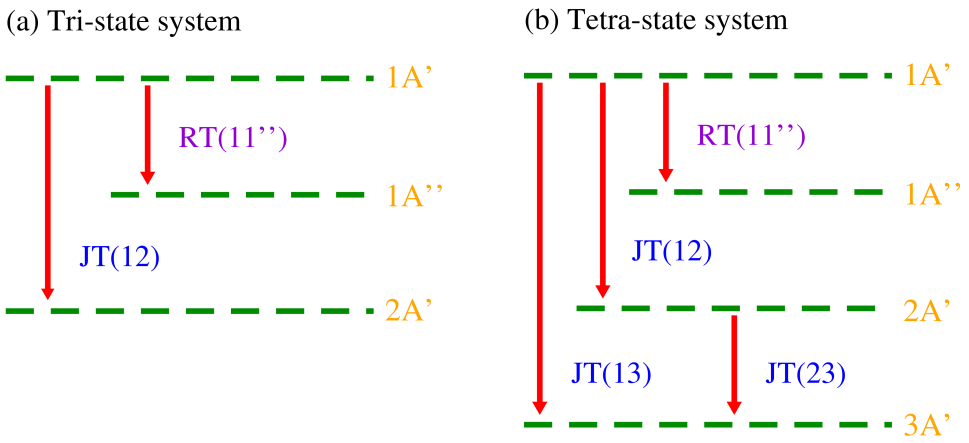

Figure 8: Schematic representation of the two RT/JT models: (a) the tri-state RT/JT model; (b) the tetra-state RT/JT model.

The form of the NACT matrix

In what follows, I am going to discuss the situation where only three electronic states are taken into account (see Fig.8 (a)). Similar but more complex results hold for the tetra-state (see Fig.8 (b)) case. Considering two A'-states and one A"-state, the NACT matrix has the form [III]:

$$\tau(s) = \begin{pmatrix} 0 & \tau_{11"} & \tau_{12} \\ -\tau_{11"} & 0 & 0 \\ -\tau_{12} & 0 & 0 \end{pmatrix} \tag{4.2.3}$$

where τ_{12} is of Jahn-Teller type between 1A' and 2A', $\tau_{11"}$ is of Renner-Teller type between 1A' and 1A" and $\tau_{21"}$ is assumed to be 0. For reasons of convenience the following form of $\tau(s)$ is preferred:

$$\tau(s) = \begin{pmatrix} 0 & \tau_{12} & \tau_{11"} \\ -\tau_{12} & 0 & 0 \\ -\tau_{11"} & 0 & 0 \end{pmatrix} \tag{4.2.4}$$

which is obtained by permuting between the last two rows and then between the last two columns (it is important to mention that the solution of (4.2.1) is not affected by these permutations).

The ADT matrix and the privileged angle

Concerning the form of the ADT matrix, I would refer to sec. 3.1, where it was pointed out that in the simplest case, namely when two electronic states are considered, the A

matrix can be represented simply by an ADT (mixing) angle, γ_{12} (eq. (3.1.4)). In the case that the two states are separated from the manifold (in the investigated region), quantized topological phase is obtained ($\alpha = n\pi, \quad n = 0, \pm1, \pm2, ...$) and A is diagonal. If the two-state topological phase is not equal to $n\pi$ in the considered region, we are forced to include three states or sometimes more to guarantee that the relevant topological phase is integer multiple of π.

For the three-state situation, A(φ,q) is a 3 x 3 orthogonal matrix and therefore its nine elements can be presented in terms of the three quasi-Euler angles [54]. As in case of the ordinary Euler matrix, the orthogonal A matrix is presented as a product of three rotation matrices $Q_{ij}(\gamma_{ij})$ (i<j=2,3), where the product $A=Q_{kl}Q_{mn}Q_{pq}$ can be written in any order. Substituting this product into (4.2.1) yields three coupled first-order differential equations for the three corresponding quasi-Euler angles, γ_{ij}. In several recent studies [42, 43], physical meaning was attributed only to one of the three ADT angles, γ_{ij}, privileged with an equation that contains the corresponding NACT, τ_{ij} as a free isolated term (there is one equation like that in every group of three coupled equations). In what follows, γ_{12} is assumed to be such an angle and we consider for this purpose the product: $A=Q_{12}(\gamma_{12})Q_{13}(\gamma_{13})Q_{23}(\gamma_{23})$. Substituting this product into (4.2.1) yields three first order equations, of which two equations (for γ_{12} and γ_{13}) form a closed subgroup of two coupled equations [55]:

$$\frac{\partial}{\partial\varphi}\gamma_{12} = -\tau_{12} - \tan\gamma_{13}(\tau_{23}\cos\gamma_{12} + \tau_{13}\sin\gamma_{12}) \tag{4.2.5}$$

$$\frac{\partial}{\partial\varphi}\gamma_{13} = \tau_{23}\sin\gamma_{12} - \tau_{13}\cos\gamma_{12} \quad . \tag{4.2.6}$$

These two equations are solved with the aim of calculating the privileged ADT angle $\gamma_{12}(\varphi, q)$. The introduction of the privileged angle enables the extension of the earlier defined two-state topological phase, α_{12} to three-state systems. A straightforward choice is the end-of-the-contour value of the angle γ_{12}. Thus, $\alpha_{12}(q)=\gamma_{12}(\varphi = 2\pi, q)$.

Inclusion of the Renner-Teller effect

Whereas the calculation of two-state JT NACTs along circular contours (Γ) in the triatomic plane is well known, one has to find the proper treatment of the RT NACT ($\tau_{11''}$) in this plane. Since the collinear axis is an infinite long interval, each circle intersects this line at two points (at $\varphi = 0\,\text{and}\,\pi$). At each such intersection point, along a short interval perpendicular to the axis, is formed a spiky non-zero NACT (in this case an angular NACT)

with features reminiscent of a Dirac-δ function. Thus, the first tendency is to assume the angular RT NACTs in the plane take the form:

$$\tau_{11^{\circ}}(\varphi|q,\Gamma) = \frac{\pi}{2}\delta(\varphi - \vartheta) \tag{4.2.7}$$

for a Γ circle with radius q (ϑ designates the intersection points). (4.2.7) yields a quantized topological phase ($=\pi$) to be expected for an undisturbed RT effect along Γ. By the existence of a JT intersection on the collinear axis, the RT effect is most likely weakened (or eventually intensified). Consequently, the pure RT quantization is affected and a way to incorporate this possibility is to extend (4.2.7) by adding a factor, η, thus:

$$\tau_{11^{\circ}}(\varphi|q,\Gamma) = \frac{\pi}{2}\eta\delta(\varphi - \vartheta) \tag{4.2.8}$$

where η is a parameter to be determined theoretically and will be termed as the Renner-Jahn coupling parameter.

In order to derive the corresponding differential equations for the tri-state RT/JT coupled system, we consider the NACT-matrix given in (4.2.4) and substitute its relevant elements into the general equations (4.2.5) and (4.2.6). It can be shown that the solution of the equation for γ_{13} is proportional to the Heaviside step function (Θ):

$$\gamma_{13}(\varphi) = \Theta(\varphi - \pi)\gamma_{13}^{(0)}(\varphi) \tag{4.2.9}$$

with

$$\gamma_{13}^{(0)}(\varphi) = -\eta\frac{\pi}{2}\cos\{\gamma_{12}(\varphi = \pi)\} \quad . \tag{4.2.10}$$

The solution for γ_{12} is also a step function of a somewhat more involved form:

$$\gamma_{12}(\varphi) = -\int_0^{\varphi} \tau_{12}(\varphi')\,\mathrm{d}\varphi' + \Theta(\varphi - \pi)\chi(\varphi = \pi) \tag{4.2.11}$$

where

$$\chi(\varphi = \pi) = -\eta\frac{\pi}{2}\tan\{\gamma_{13}^{(0)}(\varphi = \pi)\}\sin\{\gamma_{12}(\varphi = \pi)\} \quad . \tag{4.2.12}$$

This latter term, $\chi(\varphi = \pi)$ causes a shift in the privileged angle, γ_{12} for $\varphi \geq \pi$. For the whole approach to be meaningful, this vertical shift has to fulfill two conditions:

(1) Since the diabatic potentials have to be single-valued at every point (also at $\varphi = \pi$), $\chi(\varphi = \pi)$ has to guarantee the equality: $\sin[\gamma_{12}(\varphi = \pi)] = \sin[\gamma_{12}(\varphi = \pi) + \chi]$ and a similar equality (up to a sign) for the cosine function.

(2) Since $\gamma_{12}(\varphi = 2\pi) = \pm n\pi$ is supposed to occur for any closed contour, the vertical shift $\chi(\varphi = \pi)$ has to guarantee the following quantization condition for the relevant topological phase, α:

$$\alpha(q) = -\int_0^{2\pi} \tau_{12}(\varphi')\,\mathrm{d}\varphi' + \chi(\varphi = \pi) = \pm n\pi \quad . \tag{4.2.13}$$

Based on the above two conditions, the value of the Renner-Jahn coupling parameter, η can be derived (see for instance publication [III]) and is found to be a pure number:

$$\eta = \frac{2\sqrt{2}}{\pi} = 0.9003 \tag{4.2.14}$$

independent of any parameter of the molecular system. All the arguments in this section can be repeated for tetra-state systems and very similar results will hold with the same value of η. In other words, the transition from a tri-state system to a tetra-state system leaves RJCP unaffected.

4.3 Results for the F+H_2 system (JT NACTs and ADT angles)

As mentioned earlier, numerical calculations on the F+H_2 system will be carried out so as to show the viability of the theory outlined in the previous section. The F+H_2 system was treated by numerous groups during the last half-century. The numerical study by Stark and Werner [56] produced not only up-to-date ground state (adiabatic) potential for this system, but also revealed the existence of a JT intersection located on the collinear axis in the vicinity of R$\sim$5.5 au (mentioned earlier while constructing the model) and derived the first diabatic potentials for this system.

The study to be presented here is carried out for planar arrangement as formed by assuming r(=r_{HH}) to be fixed at r = 1.4 au (see Fig.7). In this treatment are calculated only the JT NACTs (using MOLPRO [57]) and the corresponding ADT angles. For this purpose are considered the three lowest A' states coupled at three collinear JT intersection points: the (1,2) CI point is located at the vicinity of R $\sim$5.5 au; the (2,3) CI point located at the vicinity of R=$\sim$1.9 au and the (3,4) CI point located at the vicinity of R=$\sim$1.8 au (see Fig.7). The (1,2) CI is formed by a Σ-state, assigned as 2A' and one of the two Π-states (with the same symmetry) assigned as 1A' (see Fig.8).

The RT degeneracy is formed by two Π-states (designated as 1A' and 1A" in Fig.8) along the HHF axis. The corresponding RT NACTs required for the present study are not calculated but assumed to be quasi-Dirac-δ functions as discussed earlier.

All the calculations are done along closed circular contours (the centers being at the same fixed point on the collinear axis at R = 6 au) in such a way that the whole region of interest is covered.

JT NACTs along closed circles

In Fig.9 are presented angular JT NACTs as calculated along four different (closed) circles with the radii: q=0.4, 3.0, 3.7 and 4.0 au. In panel (a) is presented one NACT, namely $\tau_{12}(\varphi|q = 0.4\text{au})$ whereas all the other panels present three NACTs, namely $\tau_{12}(\varphi|q)$, $\tau_{13}(\varphi|q)$ and $\tau_{23}(\varphi|q)$ (that couple the three lower A' states) calculated along circles with larger radii: q=3.0, 3.7 and 4.0 au.

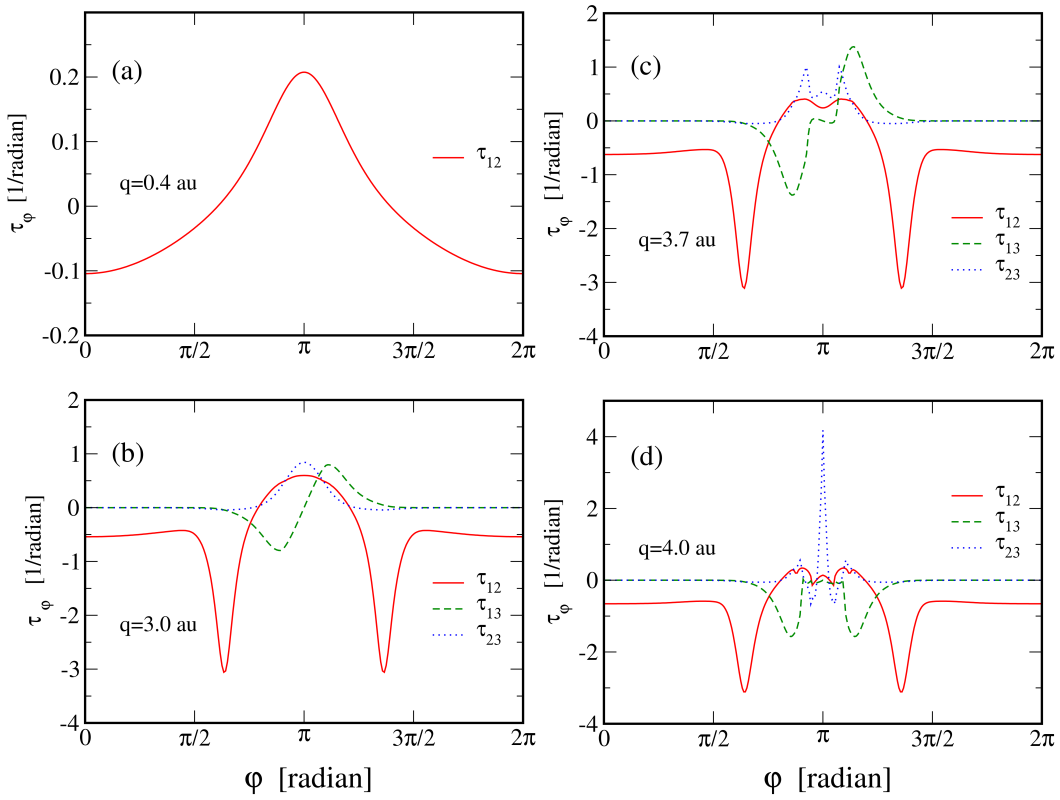

Figure 9: Angular NACTs for several circular contours at R_{ce}=6 au: (a) for q=0.4 au; (b) for q=3.0 au; (c) for q=3.7 au; (d) for q=4.0 au.

The feature that characterizes the NACT for q=0.4 au is that the circle does not surround the point of CI which is located at a distance of 0.5 au from the center of the circle. In all

other cases the circles surround the CI point and therefore the various τ_{12}'s exhibit a slightly more complicated structure. As for the two NACTs that couple the third state, the following can be said: (a) $\tau_{13}(\varphi|q)$ hardly changes as q increases; (b) $\tau_{23}(\varphi|q)$ changes significantly and becomes spikier. The reason is associated with the fact that at {R $\sim$ 1.8 au, θ= 0}$\equiv$ {q $\sim$ 4.2 au, $\varphi = \pi$} (see Fig.7) are located two additional JT intersections (as already mentioned earlier): a (2,3)CI and a (3,4)CI. As a result, the more remote is the center of the circle from these CIs, the spikier (as a function of φ) is the corresponding NACT, $\tau_{23}(\varphi|q)$. These spiky NACTs may lead to inaccuracies in calculating the corresponding ADT angles.

(1,2) ADT angles along closed circles

In Fig.10 are presented the (vertical) shifted (1,2) ADT angles, $\gamma_{12}(\varphi|q)$, as calculated according to the recipe in eqs. (4.2.11) and (4.2.12). Curves for nine q values in the range 0.4 au $\leq$ q $\leq$ 5.0 au are given.

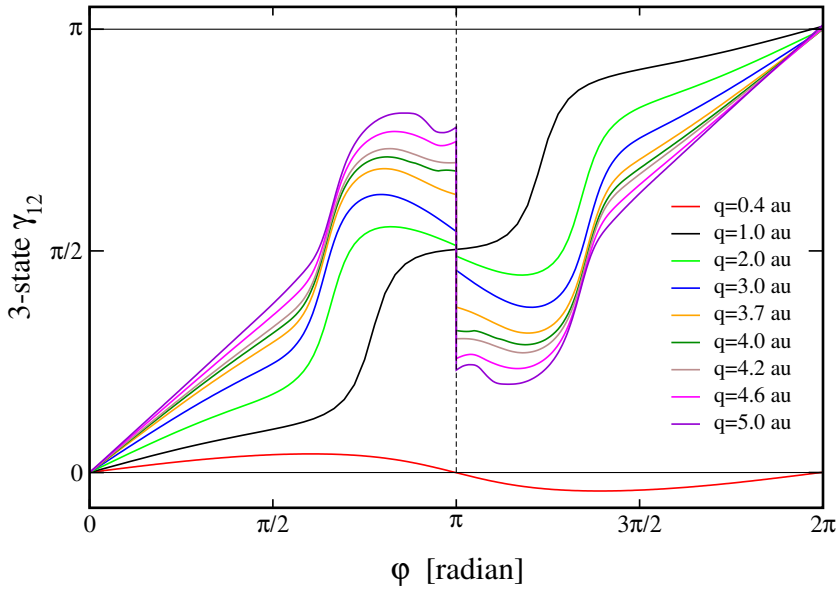

Figure 10: The tri-state ADT (mixing) angle, $\gamma_{12}(\varphi|q)$, calculated employing the RT/JT Eqs. (4.2.11) and (4.2.12). Results are shown for q values in the interval 0.4 au – 5.0 au.

Three types of curves can be distinguished: (i) The curve for q = 0.4 au is not shifted (in other words, the shift is zero) and its topological phase, $\alpha_{12}(q)$ is zero which results from the fact that the circle does not surround the (1,2) CI. (ii) The curve for q = 1.0 au is not shifted (or the shift is negligibly small) and is characteristic for the situation that the circle surrounds the (1,2) CI and therefore yields: $\alpha_{12}(q) = \pi$. (iii) In all other cases the circles surround the (1,2) CI and are shifted downwards (at $\varphi = \pi$). These two facts are the reason

that all the topological phases $\alpha_{12}(q)$ are correctly quantized (namely, become equal to π when $\varphi = 2\pi$). It is important to emphasize again that the downwards shifts for the various cases were calculated according to the formula in (4.2.12) where η is given by (4.2.14) and $\gamma_{12}(\varphi = \pi|q)$ is the corresponding privileged ADT angle. In other words, no artificial fitting is done.

Fig.10 reveals one interesting and important feature: The φ-dependence of the various curves becomes similar and the curves are converging to each other as the radius of the circles increases. This phenomenon is general but is enhanced in the interval $\pi/2 < \varphi < 3\pi/4$. Figure 11 shows schematically the region (in the square) where the convergence is most efficient. As it happens this is the region where the chemical reaction takes place. In other words, it overlaps with the transition region from the reagents arrangement to the products arrangement.

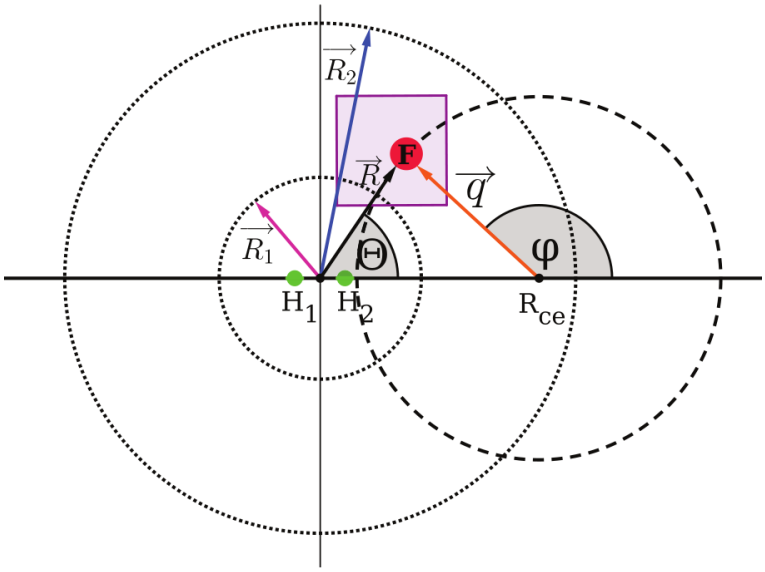

Figure 11: The transition region, presented as a square, from reagents channel to products channel.

Concerning the tetra-state results (that are not presented here), a comparison between privileged ADT angles, $\gamma_{12}(\varphi|q)$ as calculated once employing three states and once employing four states can be found in Fig.6 of publication [III]. Those ADT angles are calculated along circles with the following radii: q = 3.0, 3.7 and 4.0 au and the results are well converged for all the three cases.

In recent studies for the F+H_2 system [58, 59] only one JT NACT ($\tau_{12}(\varphi|q)$) was employed and following the corresponding expression for the two-state case - eq. (3.1.6) - quantized

topological angles were obtained only along circles with small radii (q < 2.0 au). To improve the quantization for circles with larger radii (q > 2.0 au), the addition of another A' state as well as its two corresponding NACTs, $\tau_{13}(\varphi|q)$ and $\tau_{23}(\varphi|q)$ was carried out in publication [III]. After that by solving the relevant equations for the three-state JT situation, we obtained the corresponding ADT angles. Fig.12 presents the comparison between the two JT ADT angles, $\gamma_{12}(\varphi|q)$ as calculated for q = 4.0 au (once by solving the two-state equation and once by solving the three-state equations).

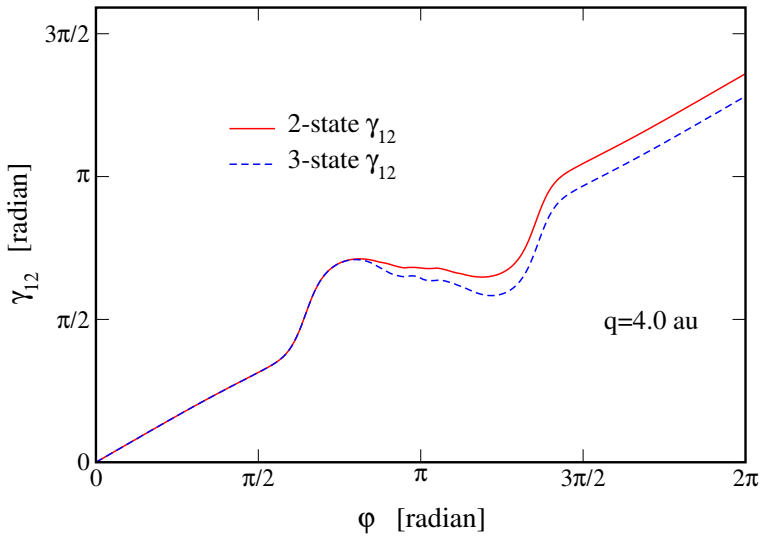

Figure 12: Comparison between the two-state and the three-state ADT (mixing) angles, $\gamma_{12}(\varphi|q)$, calculated for a circular contour at R = 6 au with radius q = 4.0 au.

It is well noticed that the two kinds of calculations yield similar values for the topological phases, $\alpha_{12}(q)$ but which differ significantly from π. In other words, increasing the JT subspace from two states to three did not yield the expected quantization (unlike in numerous other cases).

This fact led to the conclusion that the sharp increase of $\gamma_{12}(\varphi|q)$ in the region of $\pi/2 < \varphi < 3\pi/4$ is not caused by the existence of additional JT intersections (between higher states) but due to another factor, eventually, the RT degeneracy which is formed between the two Π-states. To test this possibility, a new methodology was developed which enabled the numerical study of the entangled RT/JT system. This entangled system lent itself from the start to yield the desired improvement in the quantization (a feature required for guaranteeing single-valued diabatic PESs).

The methodology presented here revealed the existence of a novel molecular parameter, η, responsible for the intra-planar coupling between the RT and the JT NACTs. This parameter was found to be a pure number $\eta = 2\sqrt{2}/\pi (=0.9003)$. At the start η was expected to be dependent on the NACTs which would make it system dependent. So far this parameter was not studied for other systems but the fact that the theoretical derivation yields a pure number implies that η is, probably, a kind of a universal molecular constant, at least as far as tri-atomic systems are concerned. This conclusion is further supported by the fact that an identical value for η is obtained for a tetra-state system.

4.4 Results for the F+H_2 system (Potential surfaces)

Having the three-state ADT angles calculated according to the new approach outlined in sec. 4.2, it is now possible to derive reliable single-valued diabatic potentials for the F+H_2 system. In recent articles it was suggested to apply an approach based on complementary line integrals [60], but this technique has one significant drawback, namely, it is approximate. The theory presented here for incorporating RT and JT NACTs has the advantage that both types of degeneracies are taken into account. As a result of it, very accurate ADT angles were obtained (quantized topological phases were given even for large circular radii) therefore one can expect accurate diabatic potential surfaces accordingly. Thus, the main goal is to present the aforementioned RT/JT PESs. There is another aim as well, namely, to find out to what extent the topological features of this system may affect the Born-Oppenheimer approximation for F+H_2.

I would refer to a recent article by Lipoff and Herschbach [61] in which they distinguish between bare and dressed potentials (while referring to the reactive F+H_2 system). Following this presentation, the bare PES is the one obtained from the electronic structure calculations (in other words, the BO lowest adiabatic PES) and the dressed PES is the effective potential felt by the reactants while approaching each other at very low temperatures (as encountered, e.g., in cold reactions). Following this study the authors concluded that the dressed potential contains important physical information concerning the low energy dynamics.

This idea was adopted by Baer et al. in a recent publication [60] with a certain twist. That work is not really about the bare potential but rather about the comparison between

two types of dressed adiabatic potentials: the ordinary one as formed by the lowest BO adiabatic PES and the second as formed by the two lowest dressed diabatic potentials (see Ref. [60] for details). The latter one therefore contains the relevant topological effects. In that study, which was based on complementary line integrals, the effect of the topological features on the lowest adiabatic PES was found very mild, thus the conclusion was that the topological effects are not expected in this system. A similar study is carried out here for the RT/JT effect but, as will be seen, with different consequences.

In order to give a basis to the study concerning dressed diabatic potential surfaces, I would start with some definitions: Given two adiabatic PESs, $V_1(\theta, R|r)$ and $V_2(\theta, R|r)$, the corresponding bare diabatic potentials, $W_1(\theta, R|r)$, $W_2(\theta, R|r)$ and $W_{12}(\theta, R|r)$ are derived from the following set of equations [7]:

$$W_1(\theta, R|r) = V_1(\theta, R|r)\cos^2\gamma(\theta, R|r) + V_2(\theta, R|r)\sin^2\gamma(\theta, R|r) \tag{4.4.1}$$

$$W_2(\theta, R|r) = V_1(\theta, R|r)\sin^2\gamma(\theta, R|r) + V_2(\theta, R|r)\cos^2\gamma(\theta, R|r) \tag{4.4.2}$$

$$W_{12}(\theta, R|r) = \frac{1}{2}\{V_2(\theta, R|r) - V_1(\theta, R|r)\}\sin(2\gamma(\theta, R|r)) \tag{4.4.3}$$

where the $\gamma(\theta, R|r)$ angles are extracted, by interpolation/extrapolation, from the values of $\gamma(\varphi, q|r)$.

In general, dressed potentials are formed by three dimensional nuclear vib-rotational eigenfunctions [61]. However, here (like in Ref. [60]) two dimensional rotational eigenfunctions will be employed for fixed values of r. Consequently the dressed diabatic potentials and coupling term are derived by the expressions:

$$\tilde{W}_j(R|r) = \left\langle \zeta_{0j}(\theta|R, r)|W_j(\theta|R, r)|\zeta_{0j}(\theta|R, r)\right\rangle \tag{4.4.4}$$

$$\tilde{W}_{12}(R|r) = \left\langle \zeta_{01}(\theta|R, r)|W_{12}(\theta|R, r)|\zeta_{02}(\theta|R, r)\right\rangle \tag{4.4.5}$$

where $\zeta_{0j}(\theta|R, r)$ (j=1,2) are the lowest rotational eigenfunctions of the two relevant diabatic potentials, $W_j(\theta|R, r)$ (j=1,2). The corresponding 2 x 2 dressed diabatic potential matrix is as follows:

$$\tilde{W}(R|r) = \begin{pmatrix} \tilde{W}_1(R|r) & \tilde{W}_{12}(R|r) \\ \tilde{W}_{12}(R|r) & \tilde{W}_2(R|r) \end{pmatrix} \quad . \tag{4.4.6}$$

This matrix is then diagonalized to calculate the lower eigenvalue, V_d(R|r), which is defined as the lowest adiabatic-via-dressed-diabatic potential.

In the numerical study the focus will be on two kinds of dressed adiabatic potentials: the just mentioned $V_d(R|r)$ and $V_a(R|r)$, which is the ordinary lowest dressed adiabatic potential given in the form:

$$V_a(R|r) = \left\langle \zeta_{01}(\theta|R,r)|V_1(\theta|R,r)|\zeta_{01}(\theta|R,r)\right\rangle \tag{4.4.7}$$

where $V_1(\theta|R,r)$ is the bare adiabatic potential and $\zeta_{01}(\theta|R,r)$ is the corresponding lowest rotational eigenfunction of $V_1(\theta|R,r)$.

All the numerical calculations leading to dressed adiabatic and dressed diabatic potential curves are carried out for three different values of the vibrational coordinate, r (r=1.4 au, 1.6 au and 1.8 au). The (vertical) shifted (1,2) ADT angles, $\gamma_{12}(\varphi, q|r)$ necessary for calculating the diabatic potential surfaces are presented in Fig.13. These angles are calculated according to the recipe in eqs. (4.2.9)-(4.2.12). Panel (a) contains results for r=1.4 au, while panels (b) and (c) for r=1.6 au and 1.8 au, respectively. The radius of the circles is in the range: 0.4 au≤q≤5 au for all the three cases.

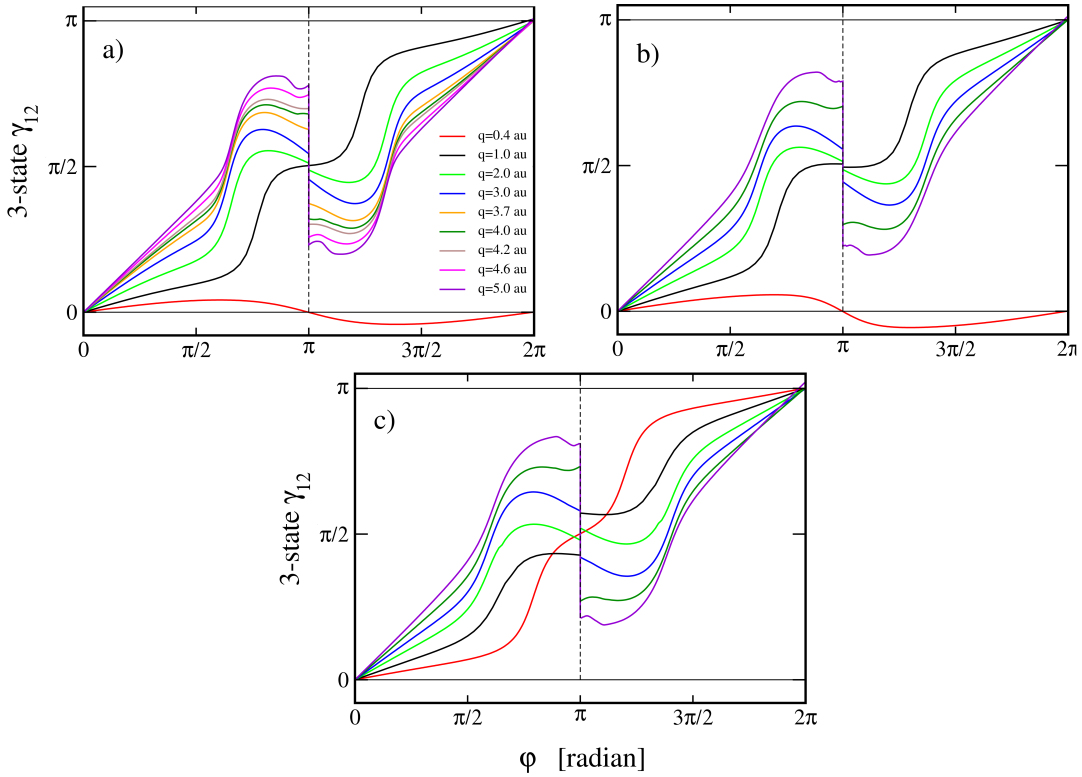

Figure 13: Tri-state ADT angle, $\gamma_{12}(\varphi|q)$, for several circular contours, calculated considering the RT/JT topological effect. Results are shown for r = 1.4 au (a), r = 1.6 au (b) and r = 1.8 au (c).

The important feature to notice is that the geometrical phase, $\alpha(q|r)$, for most curves is

practically π (thus they all surround one (1,2) CI). There are two exceptions, namely the curves formed in cases {r = 1.4 au, q = 0.4 au} and {r = 1.6 au, q = 0.4 au}. Here $\alpha(q|r)$= 0 is given, which implies that the relevant curves do not surround the (1,2) CI.

The second feature to notice is that except for the two lowest q-curves (namely, q = 0.4 au and 1.0 au) all other curves are shifted downward (at $\varphi = \pi$) to a varying degree. It is important to emphasize again that these shifts are calculated according to (4.2.12).

Another feature to notice is that the φ-dependence of the various curves becomes similar as the radius of the circles increases. This phenomenon is general and can be observed for all the three r values.

In Figure 14 are compared the equi-potential lines for the two lower potentials, the adiabatic one, $V_1(R, \theta|r)$ and the diabatic one, $W_1(R, \theta|r)$ as calculated for r (=r_{HH}) = 1.4 au (panle [A]), 1.6 au (panel [B]) and 1.8 au (panel [C]). It is seen that the two potentials differ significantly from each other although their main feature is similar, they both are characterized by a single potential barrier. This is in contrast to what was encountered in case the diabatic potentials were constructed employing complementary line integrals [60], which possess a typical saddle structure with the mini/max point located on the collinear axis (instead of a simple potential barrier).

In Figure 15 three panels are given, (a)-(c), presenting in each case three adiabatic potential curves as a function of R: (i) the lower dressed adiabatic potential, $V_a(R, r)$ (see eq. (4.4.7)); (ii) the lower adiabatic via dressed diabatic potential, $V_d(R, r)$ (see eqs. (4.4.1)-(4.4.6)) and (iii) the corresponding bare potential, $V_1(R, \theta = 0|r)$. It is important to emphasize that the values of all three potential curves in each panel are calculated by assuming the potential $V_1(R = 10\text{au}, \theta = 0|r)$, for all r values equal to zero.

The main feature to be seen is that in each panel the three potential curves differ (sometimes quite significantly) from each other. This applies not only to the (collinear) bare potential, but also to the comparison between two types of dressed adiabatic potentials. Two main features are noticed: (1) The smaller the interatomic distance of H_2, the larger the deviations are between the two dressed curves. (2) As R approaches the asymptotic region, the two dressed curves tend to overlap.

As a summary, one can say that the main goal, namely to reveal to what extent topological features of the F+H_2 system affect the lowest adiabatic PES has been succesfully carried out. This was done by comparing two types of dressed adiabatic potentials, namely $V_a(R, r)$ and

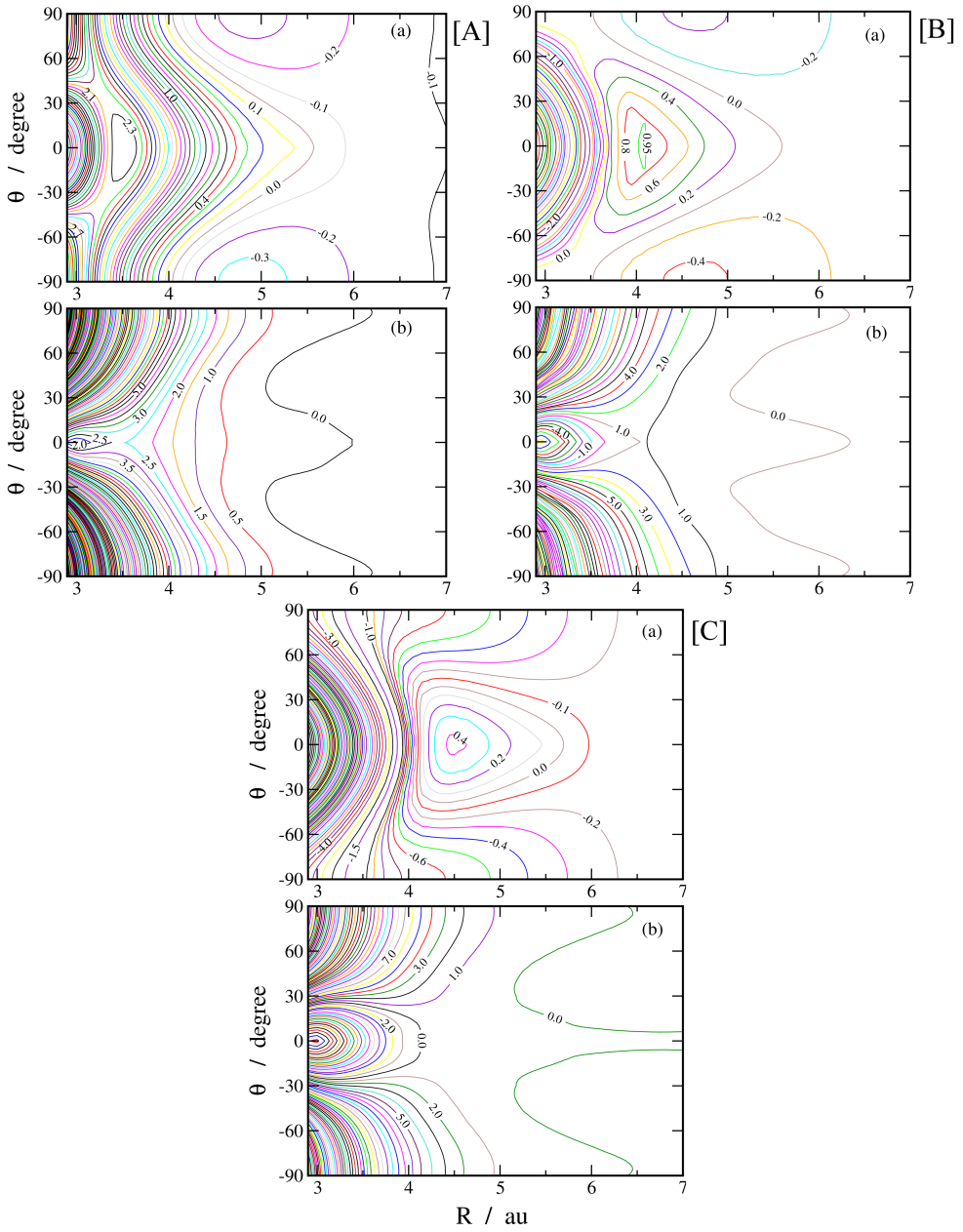

Figure 14: Equi-potential lines (in Kcal/mol) of two potential surfaces, $V_1(R,\theta)$ (shown in subpanels (a)) and $W_1(R,\theta)$ (presented in subpanels (b)). Panels [A], [B] and [C] correspond to three different values of r: 1.4 au, 1.6 au and 1.8 au, respectively.

$V_d(R,r)$ as calculated for three different values of the H_2 interatomic distance r. A similar study was done some time ago [60] employing complementary line integrals. In that case, a nice fit was obtained between the two types of dressed potentials for all three vibronic situations. In the present case we face a somewhat different situation: in two cases (for r =

1.4 au and r = 1.6 au) the two types of dressed potentials differ significantly, whereas in the third case (r = 1.8 au) they deviate only slightly. Actually, the situation is more severe (as expressed just by the absolute numbers) because the large deviations take place in situations with higher probability. In other words, the system is more likely to be, during the (low energy) interaction, in the interval 1.3 au $<$ r $<$ 1.5 au rather than, for instance, at r $\sim$ 1.8 au.

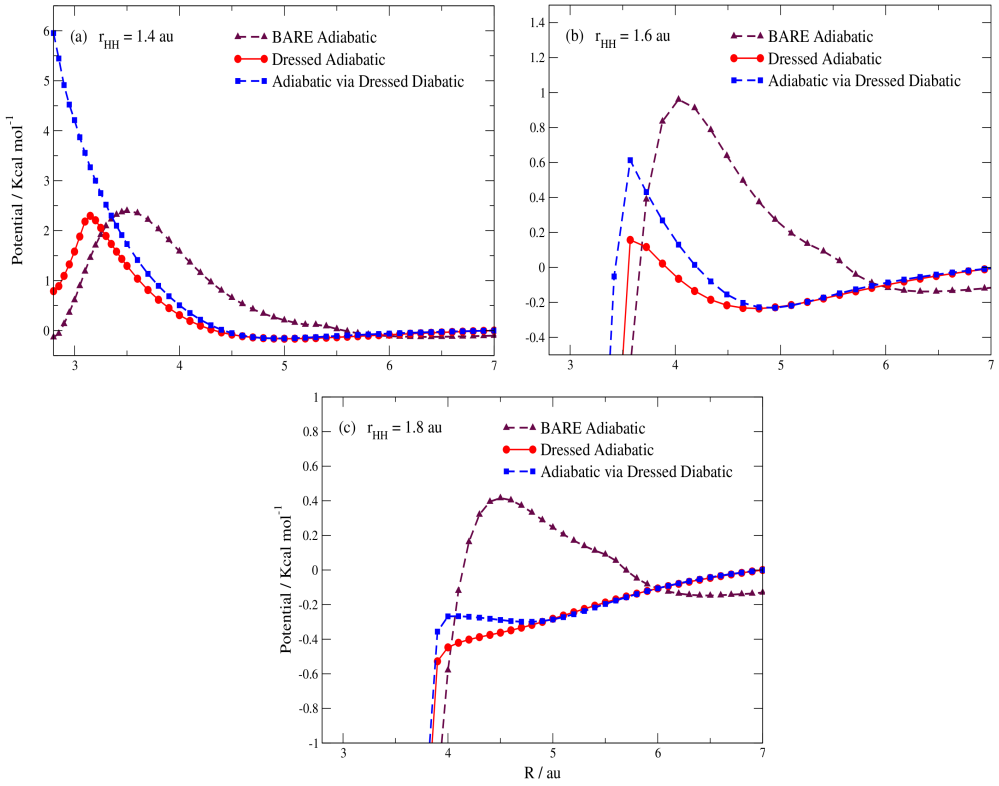

Figure 15: Potential curves for fixed vibrational coordinates (r=r$_{HH}$ and $\theta = 0$): (i) the bare adiabatic potential V$_1(R, \theta|r)$; (ii) the dressed adiabatic potential V$_a(R|r)$; (iii) and the adiabatic via dressed diabatic potential V$_d(R|r)$. The results for r$_{HH}$ = 1.4 au, 1.6 au and 1.8 au are shown in panels (a), (b) and (c), respectively.

The main conclusion of the present study is different form that of Ref. [60]: Including the RT effect in the numerical treatment (in addition to the JT intersections) yields dressed potential curves that deviate significantly from each other, thus indicating that topological effects most likely influence processes taking place on the lower adiabatic PES. In other words, this study seems to imply that the BO approximation may not be valid for the title system in general and in particular not for (ultra) cold reactions.

In the extensive topological study carried out for the $F+H_2$ system, my primary task was the numerical testing of the previously developed method for the description of the entanglement between RT and JT type intersections. Within the frames of the numerical study, I wrote program codes for processing NACTs (derived from *ab initio* calculations) and for implementing the new approach. The latter contribution included the solution of the coupled differential equations obtained for the privileged ADT angles.

In the potential surface study for $F+H_2$, I calculated the diabatic potential energies for the different vibrational coordinates of the system. For doing that, the adiabatic energies and the previously derived ADT angles have been used. In order to cover the whole chemical volume of interest, I developed a code for the interpolation and extrapolation of the ADT angles.

5. Molecular switches

Molecular switches are closely related to nonadiabatic phenomena. As will be detailed later, their operation is based on electronic structure degeneracies (CIs) and they provide the basis for other molecular level devices. In this chapter I am going to give a fundamental introduction to switching systems emphasizing their importance and wide-range applications in practice. Section 5.1 gives a brief historical overview of molecular switches by presenting their most important utilities (such as in electronics, medicine or informatics) and the main milestones of their evolution. Mostly experimental results are demonstrated in this part.

In section 5.2 I summarize the theoretical background of molecular switch systems by pointing out the most important criteria exposed to them. My own results concerning the theoretical investigation of switching properties for several molecules are presented in sections 5.3 and 5.4. These results are based on publications [V] and [VI], respectively.

5.1 Historical overview

The photo-induced switching of a molecule between its two stable and well-separated conformers is a typical photochemical reaction that may involve strong nonadiabatic relaxation dynamics at conical intersections [62]. Molecules exhibiting such processes are termed as molecular switches. Systems of this kind are of great research interest [62–76] nowadays because of their wide-range applications. Owing to their small size, switches play a fundamental role in miniaturization opening new horizons in e.g. medicine, information technology or materials science.

In the field of molecular nanotechnology and supramolecular chemistry, the control of dynamics (translational and rotational motion) is one of the most challenging goals toward future nanoscale machines and molecular electronics. The Feringa group of Groningen achieved remarkable results in this area in the last 20 years.

In 1991, Feringa reported the first optical molecular switches [77] in which chirality is controlled by light. These systems also allowed for the first time unidirectional control of rotary motion. These and related molecular switches were used by the group for data storage [78] at the molecular level and for the control of organization [79]. They were able to

demonstrate the modulation of electronic conductance [80, 81] (opto-electronic switching) at the single molecular level and in large array devices. In related studies Feringa could show that liquid crystals can be switched photochemically [82–84] and reversible LCD color pixel generation was achieved (in cooperation with Philips). The design and synthesis of the first light-driven unidirectional rotary motor was arguably the most spectacular achievement from the Feringa group which resulted in world-wide media attention. Major advances and other works have been published on molecular motors in recent years including chemical driven translational and unidirectional rotary motors, light-driven motors bound to surfaces, dramatic speed enhancement of molecular motors and the discovery of rotation of microscale objects using nanoscale motors [79–81, 85–88].

In cooperation with BioMade, a channel protein based switchable nanovalve was constructed that can be opened and closed by light or pH change. Current studies aim at using this nanovalve in controlled drug release systems [79, 85].

As mentioned already, bistable optical switches are promising candidates for high density data storage, with each molecule representing an elementary bit memory unit. There have been numerous attempts to store data on molecular level [64, 89–102], one of the most promising is presented in Ref. [64]. In 2006, Green et al. produced a memory device that potentially fulfilled the needs of the semiconductor industry outlined for 2020. Their memory array was no bigger than a single white blood cell containing 160 000 memory elements, each with an area of only 30 nanometres square, ca. 40 times smaller than those in existing devices at that time. Their memory unit stores the zeroes and ones of binary information in the switchable states of organic molecules. The system, described in detail in Ref. [64], brings the idea of molecular memories a step closer to reality. Although it may have a very high 'bit density' (10^{11} memory elements per square centimetre), this super-memory isn't going to appear in a laptop very soon. The researchers are frank about its current shortcomings, not denying that the memory cells stop working after being switched just ten times [103]. This may imply that we do have to wait until 2020 to see molecular devices with this bit density actually being used.

Computer memories have been reaching higher bit densities for decades, but it is becoming even tougher to keep up with the industry's long-term trends. Today's lithographic techniques for carving silicon into circuit patterns are unlikely to deliver the 2020 target of memory cells just 30 nm or so apart. That is one reason why researchers have begun to think

seriously about building memory devices from the bottom up using individual molecules. Green's work is a proof-of-concept, showing that molecular memory cells can be made with a bit density of $10^{11}/\text{cm}^2$. It's worth taking seriously, because in terms of miniaturization, the computer companies know that this density is what they want to achieve by 2020, although they're still unsure of the best way to do it. There are several possible alternatives, such as storing data in magnetic or ferroelectric cells or by reversibly altering the atomic structure of thin solid films. Some of these approaches are already well advanced, and the route Green is offering (a curious hybrid of silicon-based microfabrication and organic chemistry) is widely seen as an outside contender [103].

Today's dynamic random-access memories (DRAMs), which are used in most electronic devices lose charge and have to be refreshed thousands of times a second, making them power-consuming. Moreover DRAM loses all information after power is switched off. As a result of it, the operating system must be reloaded from the hard drive during start-up, eventuating in long boot-up times. In an ideal case RAM would be non-volatile, meaning that the data don't evaporate the moment power is off.

Flash memory is a form of non-volatile RAM, but it has several drawbacks: writing data is very slow, its switching lifetime is limited to around 100 000 cycles and the data do leak away eventually. This means that flash memory is not an appropriate option for computers. The molecular memory unit produced by Green et al. isn't truly non-volatile so far - the molecules begin to switch states spontaneously after an hour or so, which may be improved by modifying the molecular structure in order to make the two states more stable.

There are several other non-volatile memories currently being developed such as Magnetic RAM (MRAM) which stores data magnetically, so it requires no power (in 2006, a chip with a capacity of 4 million bits and a switching time of 35 nanoseconds was achieved). Another type is ferroelectric RAM (FeRAM), in which the switching is done by altering the polarization state of a ferroelectric material. FeRAM is already produced by Samsung (64-million-bit chip with a cell spacing of 45 nm) for applications like smart cards.

The contest of different approaches in any area of science is always beneficial. In the field of non-volatile memory devices, molecular level applications will probably play an important role by the end of this decade.

5.2 Switch properties

In a recent publication Sobolewski revealed the main criteria of molecular switch systems [62]. It was shown that the potential energy profiles of the ground and low-lying electronically excited states are highly relevant in this context. (1) It turned out that the molecule must have two well-defined stable conformers on the ground state PES. These minima have to be separated by a sufficiently large energy barrier (>1.0 eV) so as to avoid thermal interconversion. (2) Another requirement to be fulfilled by switching systems is photochromism, i.e. the excitation energies of the first excited states of the two conformers have to differ significantly (> 0.5 eV). This property allows distinction between the two stable forms. (3) The existence of a conical intersection between the ground and first excited states is a crucial condition. Through the point of CI, the molecule can return to its ground state on the femtosecond time scale accomplishing very fast switching. (4) The S_0-S_1 CI is supposed to occur on the minimum of the S_1 surface. In addition, the two isomers should have barrierless access to the CI from the Franck-Condon region of the corresponding excited state.

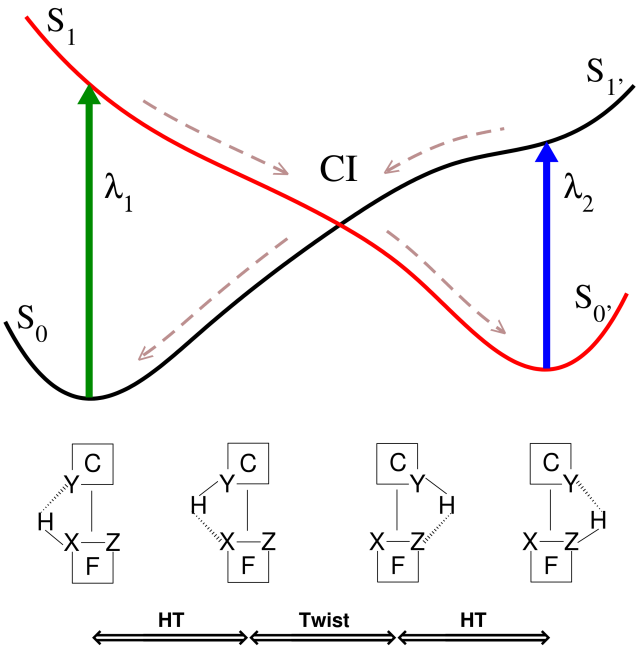

Figure 16: Schematic representation of the potential energy profiles of a bistable molecular system which can be controlled by the ESIHT reaction.

When investigating molecular switch properties, it is very important to find the proper microscopic process that can lead the system from one conformer to the other. This can typically be photo-induced ring opening/closure, cis-trans isomerization, photo-induced electron transfer, or the so-called excited state intramolecular hydrogen transfer (ESIHT) etc.. Since the switching occurs upon some external stimuli (e.g. light), the molecule must be able to survive consecutive excitations, i.e. photo-induced degradation should not occur. This requirement is fulfilled by a certain group of organic systems. Molecules possessing proton-donating and proton-accepting moieties linked by a hydrogen bond exhibit stability when irradiated many times. In such systems, the typical relaxation mechanism after optical excitation is the excited state intramolecular hydrogen transfer. ESIHT plays a key role in photostabilizers as well [104].

The characteristic behaviour of molecular switches exhibiting ESIHT reaction is presented in Fig.16. As a result of optical excitation in the enol form (λ_1), the system starts to approach the CI on S_1. Meanwhile, a H atom is transferred from the proton-donating moiety (X on frame=F) to the proton-accepting part (Y on crane=C) and the crane starts to rotate with respect to the frame. At the CI, the system decays (with a certain probability) to the ground state of the keto conformer. At the end of the reaction, the crane is twisted 180 degrees compared to the initial arrangement. In the case that the frame has a proton-accepting part too, the H atom will be transferred from the crane to this part of the frame (Z on F) resulting in the stable keto form. Reverse switching can be achieved by irradiation at a different wavelength (λ_2).

5.3 Results for two pyrimidine derivatives

When we started investigating molecular photo-switch properties, it was very important to find appropriate candidate systems. As mentioned already, Sobolewski and co-workers have studied several systems with the intention of finding molecular switch features. In one of their recent works [66] they suggest some molecules as possible candidate switching systems. Their proposal is mainly based on CC2 [105, 106] level electronic structure calculations carried out in ground state optimized structures, investigating the ESIHT process.

Following this line we selected an apparently suitable system, the 8-(pyrimidine-2-

yl)quinolin-ol molecule (PQol, Fig. 17) which can be considered as a composition of a pyrimidine crane and a double-ring frame component. After carrying out an extensive electronic structure study of PQol, we constructed a simpler system: the 2-(4-nitropyrimidine-2-yl) ethenol molecule (NPE, Fig. 20) which can be considered as a model of PQol. By doing so we were able to perform more accurate *ab initio* calculations and to test our methodologies more reliably. The related results are summarized in publication [V].

The PQol molecule

We began with the examination of the potential photo-switch functionality of PQol (see Fig. 17). Ref. [62] proposes the possibility of excited state intramolecular hydrogen transfer being promoted by the frame-crane torsion (α). This photochemical mechanism is assumed to connect the two stable, planar forms of the molecule (see Fig. 18). More specifically, Ref. [62] suggests that the ESIHT process is induced by the torsion of the molecular crane (pyrimidine ring) relative to the two-ring frame component.

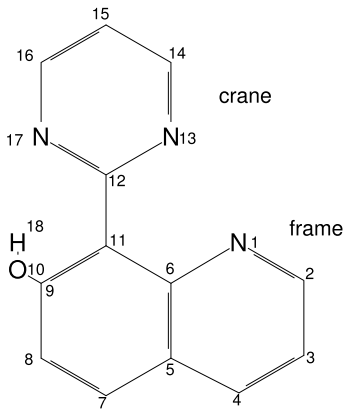

Figure 17: Ground state equilibrium geometry of the PQol molecule.

The projected driving coordinate for the hydrogen transfer is the $C_9C_{11}C_{12}N_{13}$ dihedral angle. Initially, a 0_{10}-$H_{18} \cdots N_{17}$ hydrogen bond is formed at the educt geometry. After absorbing light this hydrogen bond breaks and the new $O_{10} \cdots H_{18}$-N_{17} bond forms then the crane part of the molecule subsequently starts to rotate around the C_{11}-C_{12} double bond. This photochemical process implies that the value of the dihedral angle (α) changes from 0 to 180 degree. At the final position of the dihedral angle ($\alpha = 180°$), firstly the N_{17}-$H_{18} \cdots N_1$ hydrogen bond is formed, but this geometry still represents an intermediate conformer.

The final structure is realized by reformation of this hydrogen bond to establish the N_{17} · · · H_{18}-N_1 connection. In this final state the H_{18} atom is reattached to the molecular frame although now in a different position.

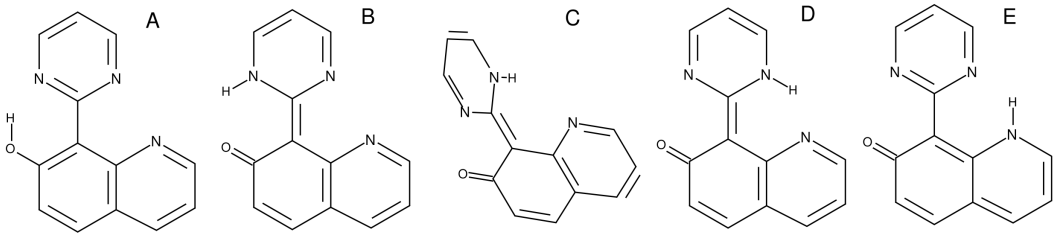

Figure 18: Different geometries of the PQol molecule appearing along the ESIHT reaction path. (A-B): Planar intramolecular hydrogen transfer; (C): Intermediate twisted geometry; (D-E): Planar intramolecular hydrogen transfer.

We have optimized the ground state geometries of PQol at the MP2 [27] level of theory by freezing the torsion angle, α at the values 0°, 90°, 180°. At α=180°, the terminal structure corresponding to H_{18} attached to N_1 as well as the upstream intermediate with N_{17}-H_{18} bond have been optimized in S_0 with the MP2 method. The geometry optimization of the α=90° conformer has been performed by fixing α and all other dihedral angles at the adjustments of the planar conformers and by varying all other coordinates. The intermediate geometries have been determined by linear interpolation to obtain the ground state potential energy profile (PEP). In Fig. 19 the ground state PEP along the above discussed reaction path is displayed. Note that two, well-separated minima have been found on the PEP of the ground state and they are separated from each other by a barrier exceeding 1 eV, which is sufficiently large to prevent thermal interconversion of the molecule, a necessary condition for a photo-switch system. The vertical excitation energies, oscillator strengths and dipole moments obtained at the optimized geometry of both conformers are presented in Table I. The optical transition to the lowest excited singlet state at the terminal structure has a moderate oscillator strength in the UV range of the spectrum (f = 0.12066, E = 3.962 eV).

The first excited state is essentially dark in absorption from the ground state (f = 0.00278, E = 4.464 eV) at the educt geometry. However, for the second excited state the value of the oscillator strength is reasonably large at this starting geometry (f = 0.39741, E = 5.302 eV). Let us consider the two stable forms of our bistable molecule, and assume

Table I: Vertical excitation energies ($\triangle E$) given in eV, oscillator strengths (f), and dipole moments (μ) given in Debye of PQol, calculated with the state-averaged CASSCF(15/22)/aug-cc-pVDZ+ECP approach at the ground state equilibrium (conformers No. 1 and 10) geometries.

State	$\triangle E$ (eV)	f osc. str.	μ(Debye)
conformer 1 (0°)			
$1A'$	0.000	—	1.222
$1A''$ $\{n_1 \rightarrow \pi_1^*\}$	4.464	0.00278	4.964
$2A'$ $\{\pi_3 \rightarrow \pi_1^*\}$	5.302	0.39741	1.547
$2A''$ $\{n_1 \rightarrow \pi_2^*\}$	5.873	0.00620	3.777
$3A'$ $\{\pi_2 \rightarrow \pi_1^*\}$	6.270	0.41769	0.805
$4A'$ $\{\pi_1 \rightarrow \pi_1^*\}$	6.814	0.25499	1.551
conformer 10 (180°)			
$1A'$	0.726[a]	—	9.372
$2A'$ $\{\pi_3 \rightarrow \pi_1^*\}$	3.962	0.12066	6.612
$3A'$ $\{\pi_2 \rightarrow \pi_1^*\}$	5.038	0.44060	6.705
$4A'$ $\{\pi_3 \rightarrow \pi_2^*\}$	5.847	0.58983	4.657
$5A'$ $\{\pi_2 \rightarrow \pi_2^*\}$	6.799	0.74548	8.034
$6A'$ $\{\pi_1 \rightarrow \pi_1^*\}$	7.622	0.22044	6.605

[a] Energy relative to the ground state global minimum.

that it can be excited from the ground states to the first excited ones by wavelengths λ_1 and λ_2, respectively. In order for this molecule to perform as a photoreversible switchable system another necessary condition has to be fulfilled: the wavelengths λ_1 and λ_2 have to be reasonably different. The implication hereof is that, the system should be switchable from one state to another by two photon energies that are markedly different from each other. As can be seen from Table I, this requirement is fulfilled by PQol, but only in the special situation that the energies for transitions between ground and first excited state (at the product structure) as well as between ground and second excited state (at the initial structure) are shifted with respect to each other by more than 1.0 eV. At the educt geometry the second excited state has to be taken into account since the oscillator strength of the first

excited state is practically zero. In order to further investigate the photo-switch potential of this compound the energy profiles of the lowest-lying excited singlet states have been evaluated as a function of the twisting coordinate. The profiles are shown in Fig. 19 with diabatic connections at eigenvalue crossings.

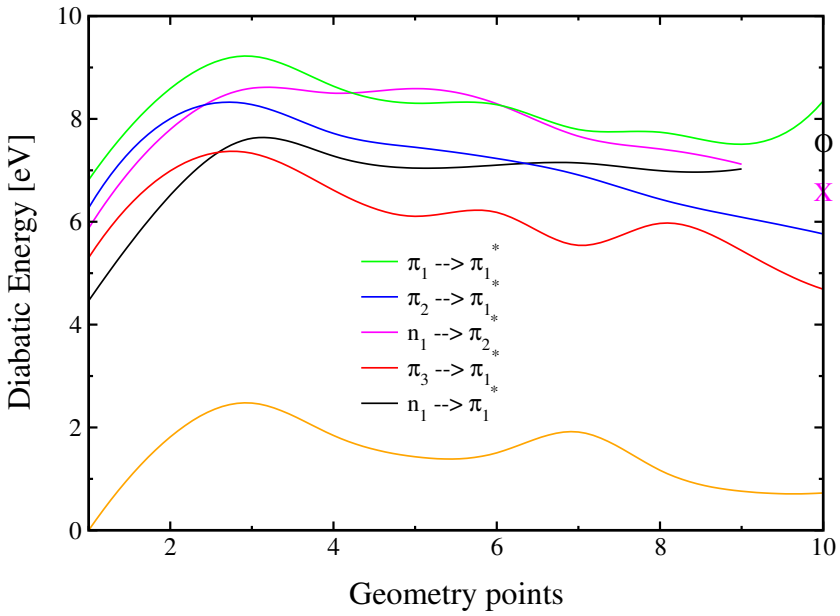

Figure 19: Potential energy profiles of the six lowest-lying singlet states of PQol (with diabatic connection at eigenvalue crossings) obtained at the state-averaged CASSCF(15/22)/aug-cc-pVDZ+ECP level of theory.

While the ground state PEP shows a sufficiently large barrier between the two minima to prevent the system from thermal interconversion, the CASSCF calculations do not predict a stabilization of excited states at nonplanar conformations. As further substantination of this, Fig. 19 indicates that no avoided crossing between the ground and first excited state exists along the pathway. The presence of the circle and cross marks at the final geometry (point 10) is due to the fact that n$\rightarrow\pi^*$ excitation is not present at that point (since the lone pair on N_1 doesn't exist), therefore a direct diabatic connection cannot be made. The relatively limited collection of data obtained in this section does not suggest effective photo-switch functionality of PQol. The system has two well-defined ground state minima which are separated from each other by a sufficiently large energy barrier to prevent thermally induced isomerization and the energy of relevant transitions of the two conformers are also different enough from each other for selective excitation of one isomer. However, the excited

state energy profiles do not indicate the existence of nonplanar minima and the first excited state does not form a pronounced avoided crossing with the ground state potential as well.

The NPE molecule

NPE represents a simplified version of PQol (Fig. 20), but a similar repulsion between nitrogen lone pair electrons can be excluded in the case of NPE. The smaller size of the system allows for, in relative terms, a more comprehensive active space. In addition, we were able to perfom more detailed numerical studies.

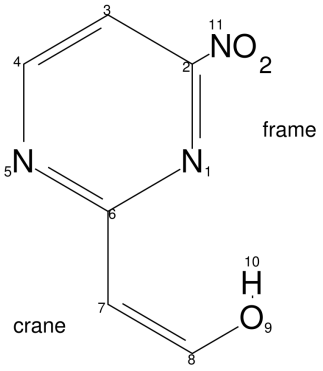

Figure 20: Ground state equilibrium geometry of the NPE molecule.

The coordinate characteristic for the reaction path (Fig. 21) is the torsion of the C_2OH_3 molecular crane about the molecular frame component. In this case the driving coordinate for the hydrogen transfer reaction is the α, $N_1C_6C_7C_8$ dihedral angle.

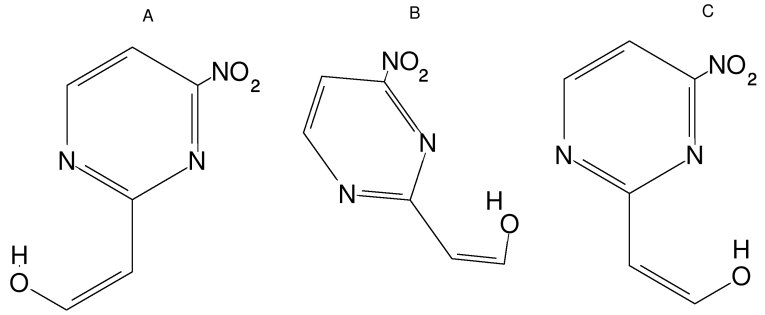

Figure 21: Different geometries of the NPE molecule appearing along the ESIHT reaction path. (A): Starting planar geometry; (B): Intermediate twisted geometry; (C): Terminal planar geometry.

In order to define the reaction coordinate, we have optimized the ground state geometries

Table II: Vertical excitation energies ($\triangle E$), oscillator strengths (f) (obtained with and without ECP) and dipole moments (μ) of NPE, calculated with the CASSCF(10/12)/aug-cc-pVDZ method (applying maximum possible weights for the respective states in the wavefunction optimization) at the ground state equilibrium geometries of the planar conformers with 0° and 180° dihedral angles.

State	$\triangle E$ (eV)		f osc. str.		μ(Debye)
	no ECP	with ECP	no ECP	with ECP	
conformer A					
(0° dihedral angle)					
$1A'$	0.018[b]	0.020[c]	—	—	3.365
$1A''$ $\{n_2 \rightarrow \pi_2^*\}$	4.555	4.346	0.00834	0.00818	3.783
$2A'$ $\{\pi_4 \rightarrow \pi_2^*\}$	4.583	4.400	0.04360	0.04561	6.410
$2A''$ $\{n_2 \rightarrow \pi_1^*\}$	5.530	5.451	0.00182	0.00123	2.029
$3A'$ $\{\pi_4 \rightarrow \pi_1^*\}$	5.845	5.877	0.40933	0.38698	7.093
$3A''$ $\{n_1 \rightarrow \pi_2^*\}$	6.567	6.248	0.00272	0.00410	4.167
conformer C					
(180° dihedral angle)					
$1A'$	0.000	0.000	—	—	5.135
$2A'$ $\{\pi_4 \rightarrow \pi_2^*\}$	4.562	4.507	0.01373	0.02908	7.603
$1A''$ $\{n_2 \rightarrow \pi_2^*\}$	4.736	4.576	0.00787	0.00791	8.703
$2A''$ $\{n_2 \rightarrow \pi_1^*\}$	5.408	5.336	$9.5\text{x}10^{-6}$	$3\text{x}10^{-6}$	7.308
$3A'$ $\{\pi_4 \rightarrow \pi_1^*\}$	5.764	5.788	0.47319	0.46132	7.271
$3A''$ $\{n_1 \rightarrow \pi_2^*\}$	6.647	6.415	0.00181	0.00145	6.003

[b] Energy relative to the ground state global minimum without using ECP.

[c] Energy relative to the ground state global minimum in case of using ECP.

at the MP2 level of theory for different values of the dihedral angle (α=0°, 30°, 60°, 90°, 120°, 150°, 180°).

During the geometry optimizations along the reaction path, all the parameters were varied except for the dihedral angles. After determining the two planar equilibrium structures of the molecule (at α=0° and α=180°) we investigated the six lowest-lying singlet states of

the molecule employing the CASSCF(13/18) method. For efficiency reasons we investigated the performance of the replacement of 1s basis functions by effective core potentials (ECPs) on C, N and O atoms. The comparison was based on CASSCF(10/12) results, obtained at the terminal structures of NPE with the full aug-cc-pVDZ basis set. Employing ECPs reduces the number of basis functions in the aug-cc-pVDZ basis representation from 321 to 309. The vertical excitation energies, oscillator strengths and dipole moments obtained with and without ECP approximation are tabulated in Table II for the two planar equilibrium geometries. The presented values are in good agreement with each other. Based on these results it can be expected that if the ECP approximation works for this small system, it will also work for similar, but larger molecules. By comparing the transition energies between the ground and the first excited states at the two stable forms, it can be calculated that they are shifted relative to each other by only ca. 0.2 eV. This is hardly sufficient to meet one of the criteria that determines the photo-switch performance of a molecule.

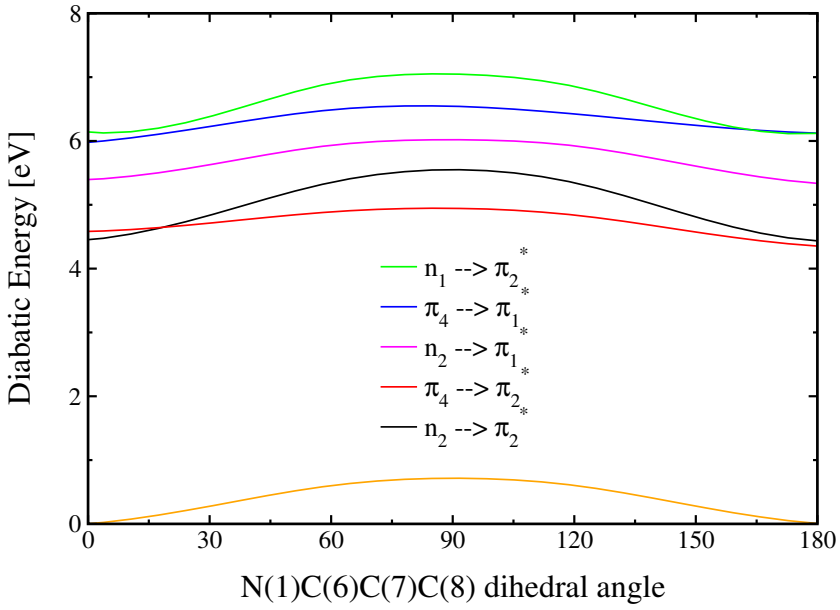

Figure 22: Potential energy profiles of the six lowest-lying singlet states of NPE, obtained at the state-averaged CASSCF(13/18)/aug-cc-pVDZ level of theory. The potential energy functions are diabatically connected at eigenvalue crossings.

Further we computed the five lowest-lying excited singlet states at the optimized ground state structures to investigate if any of them would be stabilized by the torsion. The obtained PEPs, with diabatic connections at eigenvalue crossings, are displayed in Fig. 22. The

ground state PEP shows a sufficiently large barrier between the two ground state minima to prevent the system from thermally induced isomerization. However, like in the case of PQol, no stabilization of excited states at nonplanar conformations are apparent. There are also no avoided crossings between the ground and first excited states along this coordinate.

5.4 Results for several quinoline compounds

According to the suggestion of a recent publication [66] we intended to study the effect of different chemical substituents on the aforementioned molecular switch features (see Sec. 5.2), considering the ESIHT reaction mechanism (Fig. 23). Based on electronic structure information, Ref. [66] suggests several functional groups to be substituted to a 7-hydroxyquinoline frame as crane fragments in order to provide a better performance of switch molecules. The π-electron donating NH_2 group is proposed to be linked to the frame so as to amplify the shift of the electron density from the frame toward the crane, while the presence of π-electron withdrawing BH_2 or CN groups on the molecular crane is supposed to pull the electron density from the frame.

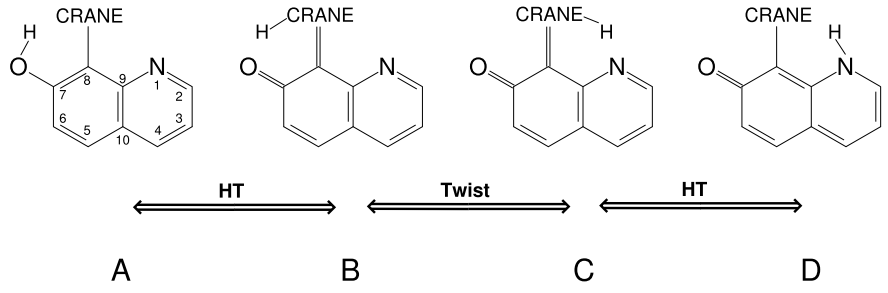

Figure 23: Geometries appearing along the ESIHT reaction path.

We started our investigations with the 7-hydroxyquinoline-8-carboxamide molecule (7HQ8CA, see Fig. 24(a)) which can be considered as being composed of a carboxamide crane moiety attached to the 7-hydroxyquinoline frame at position 8. After this the replacement of NH_2 by BH_2 and CN has been sequentially studied (Fig. 24(c) and Fig. 24(e)). In addition, the impact of a NH_2 group linked to the frame at position 4 has also been investigated for the three cases (Fig. 24(b), Fig. 24(d) and Fig. 24(f)). The studied systems can be associated with the following abbreviations:

7HQ8CA	7-hydroxyquinoline-8-carboxamide	Fig. 24(a)
4A7HQ8CA	4-amino-7-hydroxyquinoline-8-carboxamide	Fig. 24(b)
7HQ8CB	7-hydroxyquinoline-8-carboxyboryl	Fig. 24(c)
4A7HQ8CB	4-amino-7-hydroxyquinoline-8-carboxyboryl	Fig. 24(d)
7HQ8CC	7-hydroxyquinoline-8-carboxycyanide	Fig. 24(e)
4A7HQ8CC	4-amino-7-hydroxyquinoline-8-carboxycyanide	Fig. 24(f)

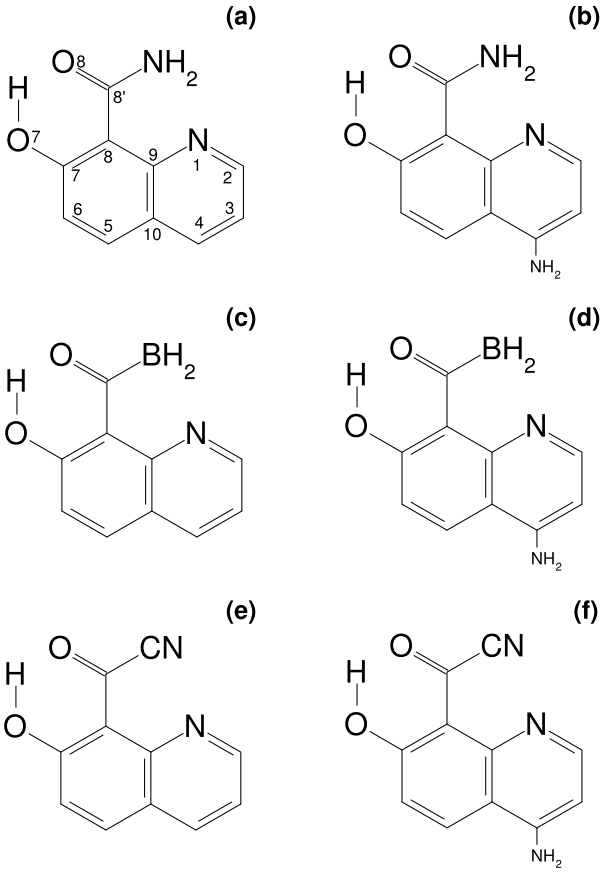

Figure 24: Ground state equilibrium structures of the investigated systems. Numbering of the atoms is common for all the molecules.

According to the preliminary geometry optimizations carried out in the ground state at the MP2/def-SV(P) level of theory, it was obvious that all the six systems possess two well-defined tautomeric minima corresponding to A and D in Fig.23. As a next step, it was

Table III: Vertical excitation energies (ΔE) and oscillator strengths (f) of the 7HQ8CA and 4A7HQ8CA molecules calculated at the CC2/cc-pVDZ level in the ground state equilibrium geometries. The equilibrium structures have been optimized by the MP2/def-SV(P) method.

	7HQ8CA		4A7HQ8CA		
State	ΔE [eV]	f	ΔE [eV]	f	State
Enol conf.					
S_0	0.0	—	0.0	—	S_0
$\pi_1\pi_1^*$	4.002	0.11114	4.073	0.08880	$\pi_1\pi_1^*$
$n_1\pi_1^*$	4.694	0.00111	4.520	0.11173	$\pi_2\pi_1^*$
$\pi_2\pi_1^*$	4.797	0.00751	4.869	0.00163	$n_2\pi_1^*$
$n_2\pi_1^*$	4.859	0.00023	4.897	0.00039	$n_1\pi_1^*$
$\pi_1\pi_2^*$	5.353	0.20538	5.229	0.17262	$\pi_3\pi_1^*$
Keto conf.					
S_0	0.307[a]	—	0.251[a]	—	S_0
$\pi_1\pi_1^*$	3.097	0.12517	3.345	0.10357	$\pi_1\pi_1^*$
$n_3\pi_1^*$	3.428	0.00016	3.646	0.00004	$n_3\pi_1^*$
$\pi_1\pi_3^*$	4.261	0.16201	4.222	0.07308	$\pi_1\pi_3^*$
$n_3\pi_3^*$	4.578	0.00012	4.648	0.00012	$n_3\pi_3^*$
$n_2\pi_1^*$	4.717	0.00479	4.882	0.40088	$\pi_2\pi_1^*$

[a] Energy relative to the ground state global minimum.

important to explore and compare the spectra of both isomers of each molecule. By doing so one can reveal information about some switch requirement mentioned in Sec. 5.2. Table III contains the CC2/cc-pVDZ quality vertical excitation energies and oscillator strengths (relative to the ground state) of the 5 lowest-lying electronically excited states of the 7HQ8CA and 4A7HQ8CA molecules calculated at the two stable (enol and keto) ground state conformers. For comparison, Table IV and Table V display identical parameters determined with the same methods but for the 7HQ8CB/4A7HQ8CB and 7HQ8CC/4A7HQ8CC pairs, respectively.

In Table III the $\pi_1\pi_1^*$ state corresponds to the HOMO-LUMO excitation with both orbitals

Table IV: Vertical excitation energies (ΔE) and oscillator strengths (f) of the 7HQ8CB and 4A7HQ8CB molecules calculated at the CC2/cc-pVDZ level in the ground state equilibrium geometries. The equilibrium structures have been optimized by the MP2/def-SV(P) method.

	7HQ8CB		4A7HQ8CB		
State	ΔE [eV]	f	ΔE [eV]	f	State
Enol conf.					
S_0	0.0	—	0.0	—	S_0
$n_a\pi_a^*$	2.856	0.00002	2.993	0.00015	$n_a\pi_a^*$
$\pi_a\pi_a^*$	3.723	0.10999	3.957	0.11241	$\pi_a\pi_a^*$
$n_a\pi_c^*$	3.777	0.00084	4.114	0.00114	$n_a\pi_c^*$
$n_a\pi_b^*$	4.435	0.00005	4.441	0.10388	$\pi_b\pi_a^*$
$\pi_b\pi_a^*$	4.559	0.01611	4.472	0.00775	$n_a\pi_b^*$
Keto conf.					
S_0	0.533[a]	—	0.486[a]	—	S_0
$n_a\pi_a^*$	2.363	0.00018	2.678	0.00038	$n_a\pi_a^*$
$\pi_a\pi_a^*$	2.881	0.11946	3.243	0.10023	$\pi_a\pi_a^*$
$n_a\pi_b^*$	3.183	0.00058	3.408	0.00033	$n_a\pi_b^*$
$\pi_a\pi_b^*$	4.147	0.05760	4.162	0.01211	$\pi_a\pi_b^*$
$n_a\pi_c^*$	4.218	0.00062	4.268	0.00053	$n_a\pi_c^*$

[a] Energy relative to the ground state global minimum.

being localized on the frame moiety. The n_1 orbital is a lone pair on the N atom of the double ring, while n_2 and n_3 are localized on the crane part. Both π_2 and π_3 are mainly spread over the frame, while the π_2^* and π_3^* MOs have large amplitudes on the frame and crane components as well.

In Table IV the $\pi_a\pi_a^*$ electronic state is identified as the HOMO-LUMO transition where both MOs are on the frame part. n_a resides on the crane, while all the remaining orbitals presented in Table IV are localized on the frame, π_b^* and π_c^* possessing significant densities on the frame-crane bridge as well.

Most of the molecular orbitals in Table V are again localized on the frame with the

Table V: Vertical excitation energies (ΔE) and oscillator strengths (f) of the 7HQ8CC and 4A7HQ8CC molecules calculated at the CC2/cc-pVDZ level in the ground state equilibrium geometries. The equilibrium structures have been optimized by the MP2/def-SV(P) method.

	7HQ8CC		4A7HQ8CC		
State	ΔE [eV]	f	ΔE [eV]	f	State
Enol conf.					
S_0	0.0	—	0.0	—	S_0
$n_A\pi_A^*$	3.825	0.06818	3.724	0.14768	$\pi_A\pi_A^*$
$\pi_A\pi_A^*$	3.880	0.07809	3.866	0.02474	$n_A\pi_A^*$
$n_B\pi_A^*$	4.221	0.00132	4.014	0.09022	$\pi_B\pi_A^*$
$\pi_B\pi_A^*$	4.525	0.17669	4.236	0.00228	$n_B\pi_A^*$
$\pi_A\pi_B^*$	4.794	0.01000	4.759	0.03333	$\pi_A\pi_B^*$
Keto conf.					
S_0	0.269[a]	—	0.192[a]	—	S_0
$n_C\pi_A^*$	3.080	0.00135	3.110	0.00076	$n_C\pi_A^*$
$\pi_A\pi_A^*$	3.286	0.12867	3.429	0.12490	$\pi_A\pi_A^*$
$n_C\pi_B^*$	3.603	0.04237	3.697	0.19246	$\pi_A\pi_B^*$
$\pi_A\pi_B^*$	3.619	0.19932	3.914	0.00157	$n_C\pi_B^*$
$n_A\pi_B^*$	4.283	0.00041	4.299	0.00141	$n_A\pi_A^*$

[a] Energy relative to the ground state global minimum.

following exceptions: n_A and n_C are completely localized on the crane, n_B is the lone pair of the double ring N atom, while π_A^* and π_B^* are spread over not only the frame, but also the frame-crane link.

As can be noticed, the difference between the first excitation energies of the enol and keto conformers is larger than 0.5 eV in all the cases, except for 4A7HQ8CB. This implies that apart from 4A7HQ8CB the remaining systems fulfill the photochromism criterion outlined for switch molecules. To determine the extent that the electronic states can be populated, oscillator strengths must be considered. The first excited states of the 7HQ8CA and 4A7HQ8CA systems have relatively high oscillator strengths in both the enol and keto

conformers (Table III). However, in case of the 7HQ8CB and 4A7HQ8CB systems, S_1 is essentially a dark state for both conformers. Although, population of the S_1 state still might be possible from e.g. the second excited state which possesses considerable oscillator strengths (Table IV). The enol conformers of 7HQ8CC and 4A7HQ8CC are directly excitable, while their keto forms only indirectly (via e.g. a CI between the first and second excited states).

Since low-lying electronic states play the key role in the photophysics of molecular switches, we have investigated the ground and first excited states along the aforesaid ESIHT reaction path. After excitation, the system evolves on the S_1 surface. Therefore, ground state PESs calculated in S_1-optimized structures are more relevant than the ones determined in S_0-optimized geometries. It was demonstrated several times that the difference between ground state PESs calculated in S_0 and S_1-optimized geometries is approximately a vertical shift in energy [62, 65, 66].

As for driving coordinates, the following displacements were utilized: the O_7H distance, the $C_9C_8C_{8'}O_8$ dihedral angle between the frame and crane components and the N_1H distance (Fig. 24).

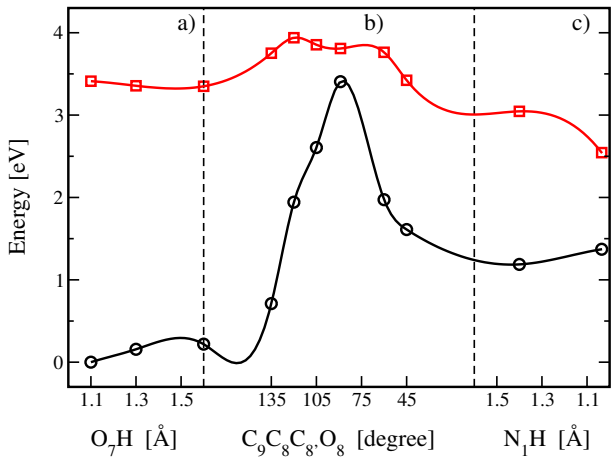

Figure 25: Potential energy profiles of the 7HQ8CA molecule in the ground and first excited states calculated at the CC2/cc-pVDZ level of theory. The geometries along the reaction path were optimized in the first excited state with the CC2/def-SV(P) method.

Fig. 25 reveals the S_0 and S_1 energy profiles of the 7HQ8CA system determined in the CC2/def-SV(P) optimized geometries of the S_1 state. The energy values were obtained using the CC2/cc-pVDZ method. For the 7HQ8CB and 7HQ8CC molecules, Fig. 26 and Fig. 27 provide the same kind of information.

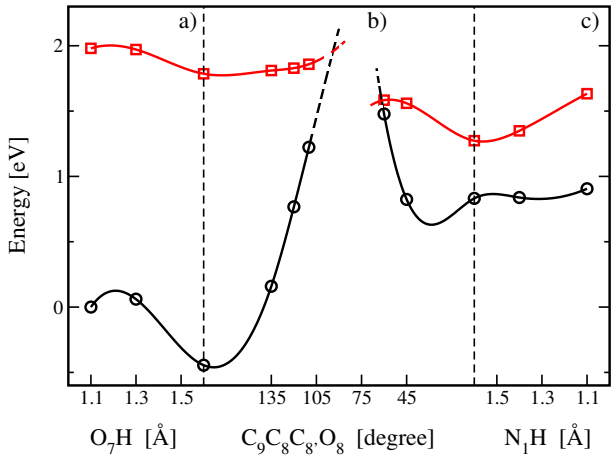

Figure 26: Same as in Fig. 25 but for the 7HQ8CB molecule.

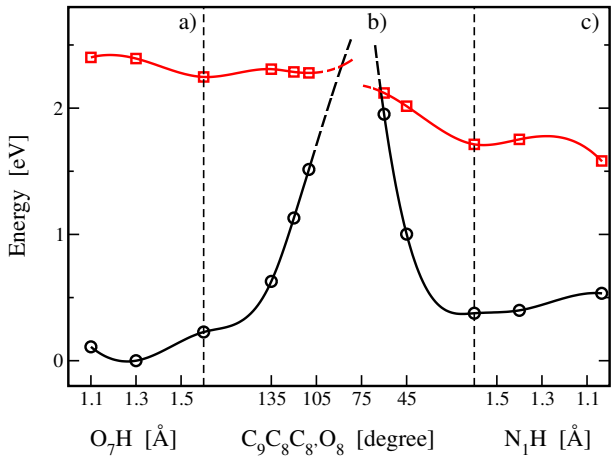

Figure 27: Same as in Fig. 25 but for the 7HQ8CC molecule.

It is seen that the A→B reaction on S_1 is exoenergetic for all the three systems, while the D→C process is exoenergetic only for 7HQ8CB. A common feature of the three systems is that the ground state is significantly increased upon the frame-crane twist with a maximum at near perpendicular arrangement. As a result, the ground state enol and keto conformers are well separated from each other. The smallest barrier occurs in the case of 7HQ8CB (ca. 1 eV). These energy barriers are high enough to prevent the systems from thermal interconversions. Moreover, it is very likely that they become even larger if the ground state surfaces calculated in S_0-optimized structures are considered.

In most of the cases, the excited state surfaces are also risen, but only slightly. The outcome is that S_0 and S_1 approach each other. This is especially pronounced for 7HQ8CB

and 7HQ8CC. In the vicinity of the 90 degree twist, dashed segments indicate that CC2 calculations failed to converge in this region (Fig. 26 and Fig. 27). Concerning the NH_2 substituted (at position 4) counterpart systems, we have obtained very similar potential energy profiles (differences are less than 0.1 eV). The related figures are shown in the Supplementary Information belonging to publication [VI].

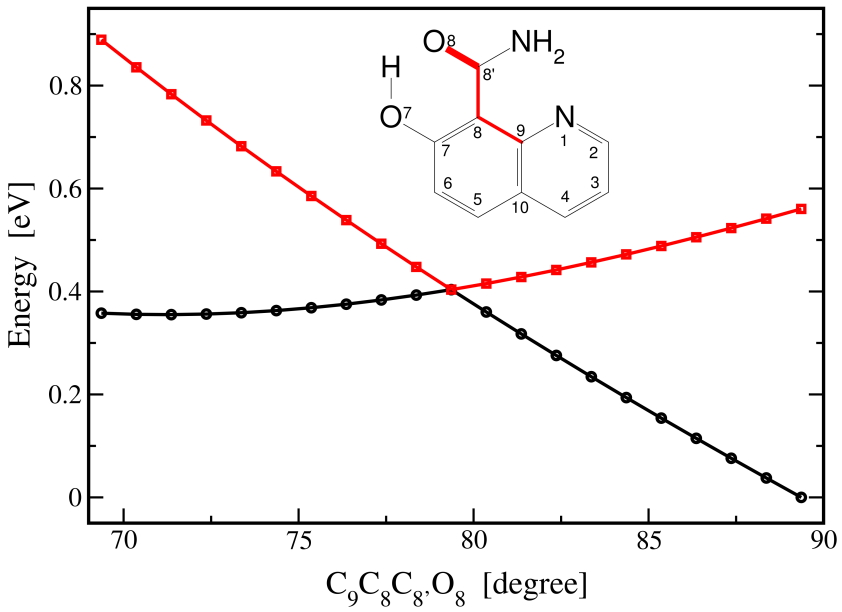

Figure 28: CASSCF(6/5)/6-31G* quality energy profiles of the ground and first excited states of the 7HQ8CA molecule in the vicinity of the conical intersection. The inset contains the structure of the system highlighting the $C_9C_8C_{8'}O_8$ dihedral angle with red.

In order to find conical intersections between the studied electronic states, we have applied the CASSCF method. CASSCF, being a multi-reference electronic structure method, is capable of treating the mixture of electronic states in the region of CIs. Starting from CC2/def-SV(P) optimized structures we were able to localize CIs at CASSCF(2/2)/6-31G* level of theory for all the six molecules. Applying larger active space (CASSCF(6/5)/6-31G*), we have managed to determine the point of CIs more accurately. The values of the driving coordinates at the optimized conical intersections can be found in Table VI. The frame-crane torsion angles were found to be in the range of 79-99 degrees, while the O_7H and N_1H distances were between 3.15-3.45 Å and 3.3-3.9 Å, respectively.

For the 7HQ8CA system, Fig. 28 presents the CAS(6/5) energy profiles of the two lowest electronic states in the vicinity of the conical intersection. In Fig. 29 the S_0 and S_1 surfaces

are shown as a function of the $C_9C_8C_{8'}O_8$ dihedral angle and the $C_{8'}O_8$ distance in the vicinity of the conical intersection. Structure and geometry parameters belonging to the optimized intersections can be found in the Supplementary Information of publication [VI].

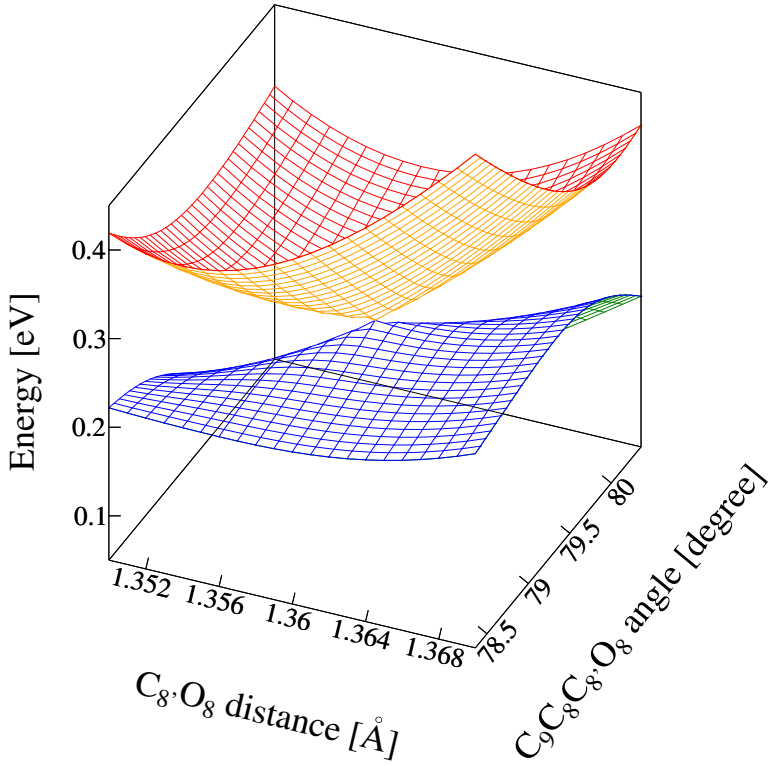

Figure 29: Potential energy surfaces of the ground and first excited electronic states of the 7HQ8CA molecule in the vicinity of the conical intersection. The energy values have been calculated at the CASSCF(6/5)/6-31G* level of theory.

The HOMO/LUMO molecular orbitals at the conical intersections are also shown in the Supplementary material, here we just depict the ones for the 7HQ8CA and 4A7HQ8CA systems in Fig. 30. These singly occupied orbitals are orthogonal to each other and account for the major part of the excitations.

After investigating the switching properties of the discussed systems, we can state that our efforts were successful. To the best of our knowledge, we localized conical intersections for the first time in these molecules, which is presumably the most important criterion outlined to switch systems. The presence of CIs is not only interesting in the context of switching, but opens up new horizons in the dynamical treatment of these systems.

Table VI: Values of the driving coordinates at the conical intersections.

Molecule	O_7H [Å]	$C_9C_8C_{8'}O_8$ [degree]	N_1H [Å]
7HQ8CA	3.157	79.363	3.893
4A7HQ8CA	3.136	79.255	3.894
7HQ8CB	3.433	91.219	3.334
4A7HQ8CB	3.237	98.379	3.499
7HQ8CC	3.399	91.439	3.411
4A7HQ8CC	3.385	91.270	3.406

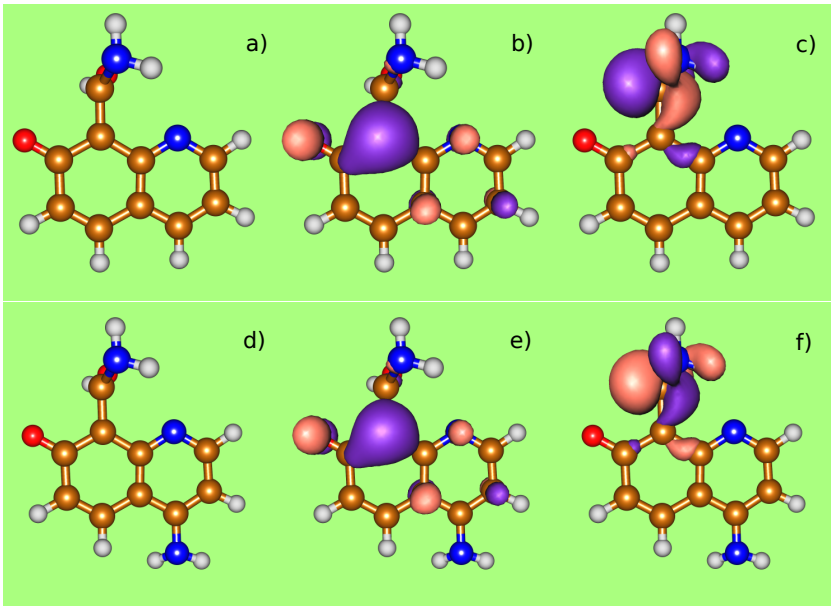

Figure 30: Geometries of the 7HQ8CA (a) and 4A7HQ8CA (d) molecules at the S_0-S_1 conical intersections. The corresponding HOMO (panels (b) and (e)) and LUMO (panels (c) and (f)) orbitals are also presented.

According to the potential energy landscapes of Fig. 25 – Fig. 27 one can expect that the 7HQ8CA/4A7HQ8CA and 7HQ8CC/4A7HQ8CC pairs will probably be switchable only in one direction (enol→ keto) while the 7HQ8CB/4A7HQ8CB pair is most likely suitable for reversible switching. However, in order to fully confirm our predictions concerning the photo-switch behaviour of the studied molecules, quantum dynamical calculations on the S_0 and S_1 electronic surfaces are necessary, which can be the subject of a future work.

In the *ab initio* studies carried out for the pyrimidine and quinoline compounds, I optimized the geometries of the molecules both in the ground and excited electronic states. Then in these geometries I calculated the electronic properties (including vertical excitation energies, dipole moments and oscillator strengths relative to the ground states) applying high-level techniques. After constructing the reaction paths, I produced the potential energy profiles of the low-lying electronic states for the investigated molecules. Furthermore, for the quinoline systems I optimized the conical intersections and investigated the behaviour of the relevant molecular orbitals.

6. Effective-mode dynamical calculations

In this chapter I would like to introduce a very efficient method that can be used for describing the nuclear motion of molecules when the BO approximation breaks down and the nuclear and electronic motions are strongly coupled. Section 6.1 describes the starting model, the so-called linear vibronic coupling (LVC) Hamiltonian, which was developed in the 1980's and has been successfully applied many times.

The next section presents the quadratically extended vibronic coupling (QVC) Hamiltonian and the related three-effective-mode formalism. The introduction of effective modes allows for the investigation of short-time dynamics in large systems. It is also useful because instead of treating all the modes, only three effective modes are needed for describing the dynamics at short times.

My own results (based on publication [I]) are presented in section 6.3. Here the application of the QVC 3-effective-mode model to the butatriene molecule is carried out and a detailed comparison to the exact 18-mode, a 5-mode LVC and the LVC three-effective-mode results is presented in terms of autocorrelation functions, photoelectron spectra and diabatic state populations. For the numerical analysis, the multi-configuration time-dependent Hartree method has been used [30, 31], which is one of the most powerful techniques currently available. It can propagate multidimensional wavepackets and handle the multi-mode quantum dynamics of polyatomic molecules with controllable accuracy up to 20-30 modes.

6.1 The vibronic coupling model

Vibronic coupling (VC) in a molecule involves the interaction between electronic and nuclear vibrational motions. The term "vibronic" originates from the combination of the terms "vibrational" and "electronic". Vibronic coupling is neglected within the Born-Oppenheimer approximation. This effect is crucial to the understanding of nonadiabatic processes, especially near conical intersections.

The expansion of the diabatic potential matrix, W provides an ideal starting point for a simple, general model Hamiltonian for the description of the topology around a conical intersection. If W is known (which is very rarely true for real polyatomic systems) then of course the approximation is unnecessary. Instead of expanding the diabatic potential around the intersection, the expansion point is chosen to be the ground state equilibrium geometry

(the Franck-Condon point). This allows a good simultaneous description of the ground and excited states, which is required for a dynamical simulation.
The VC model Hamiltonian then reads [6]:

$$H^{VC} = H^{(0)} + W^{(1)} + W^{(2)} + W^{(3)} + \quad ... \tag{6.1.1}$$

where the zero-order term is the ground state Hamiltonian of a harmonic oscillator. The diabatic operator matrices, $W^{(n)}$ constitute terms to fit the model potentials to the excited state manifold potential energy functions as closely as possible. Its elements can be determined by *ab initio* calculations.

It has been shown in many works that the above model is ideally suited for processes in which the excitation occurs from the ground state into a manifold where the conical intersection is close to the Franck-Condon point (cations of butatriene, ethylene, benzene etc.). In such cases the transfer to the CI and motion through it dominates the dynamics and this is well-described by a short expansion. Often only a first-order diabatic matrix is required. In some studies the second-order terms were also included in the model (pyrazine and allene) and their effect was shown to have a great impact on the spectrum.

6.2 The effective-mode formalism

In 2005, Cederbaum and co-workers performed a remarkable work, called the three-effective-mode model, for describing the short-time dynamics through CIs in truly large molecular systems [107]. This approach is based on the LVC Hamiltonian and concerns only two-state intersections but can be generalized to an arbitrary number of states [108]. It both gives a detailed analysis of the different modes of a macromolecule or a molecule embedded in an environment and proposes a scheme for treating them accordingly. This is achieved by an appropriate decomposition of the Hamiltonian.

In this approach, all the modes of the macrosystem were decomposed into a system part and an environment part and then, applying an orthogonal transformation, a new scheme was suggested for further decomposition of the environment modes. Finally, only three effective modes from the environment were obtained, which together with the system modes steer the short-time dynamics in macrosystems [109, 110]. The obtained method allows for accurate quantum dynamical calculations on a short time scale in the close vicinity of conical intersections, describing the effect of the environment with only three effective modes instead

of handling all environmental modes explicitly. As a continuation of this work, a further step was suggested by the construction of new additional effective modes, which facilitated the accurate description of intermediate-time dynamics [108, 111, 112].

By obtaining another conceptually different extension of the presently described effective-mode scheme, Vibók and collegues worked out an alternative approach that has been used previously by Burghardt and collaborators [113–117].

Vibók et al. gave a further development of the three-effective-mode model. Instead of the linear vibronic coupling Hamiltonian [3] that has been used before, the quadratic vibronic coupling Hamiltonian [118] was applied to obtain the appropriate quadratically extended three-effective-mode equations. This QVC Hamiltonian accounts for not only the frequency changes in the interacting electronic manifold but also (implicitly) for a dependence of the vibronic coupling constants on the coordinates of the totally symmetric modes [118]. This can give rise to rather complex potential energy surfaces and extend considerably the range of applications compared to that of the more traditional LVC scheme (see chapter seven of Ref. [5]).

Indeed, the QVC approach has been applied successfully in the past to reproduce a number of complex photoelectron spectra [119–122]. Therefore, it seems very relevant to investigate how it performs in the effective-mode framework. The remaining part of this section is devoted to the derivation of the QVC three-effective-mode Hamiltonian.

The N-mode QVC Hamiltonian for a two-state conical intersection situation in diabatic representation can be written as [I]:

$$H^{QVC} = \begin{pmatrix} E_1 & 0 \\ 0 & E_2 \end{pmatrix} + \sum_{k=1}^{N} H_k + \frac{1}{2} \sum_{k,l=1}^{N} H_{k,l} \tag{6.2.1}$$

where

$$H_k = \frac{\omega_k}{2}(p_k^2 + \chi_k^2)\mathbf{1} + \begin{pmatrix} \kappa_k^{(1,1)}\chi_k & \kappa_k^{(1,2)}\chi_k \\ \kappa_k^{(2,1)}\chi_k & \kappa_k^{(2,2)}\chi_k \end{pmatrix} \tag{6.2.2}$$

and

$$H_{k,l} = \begin{pmatrix} \gamma_{kl}^{(1,1)}\chi_k\chi_l & \gamma_{kl}^{(1,2)}\chi_k\chi_l \\ \gamma_{kl}^{(2,1)}\chi_k\chi_l & \gamma_{kl}^{(2,2)}\chi_k\chi_l \end{pmatrix} \quad . \tag{6.2.3}$$

Here χ_k is the coordinate of the kth vibrational mode, p_k is the canonical momentum and **1** is the 2×2 unit matrix. Each individual Hamiltonian, H_k is built up of three different parts: the first term is a harmonic 0^{th}-order Hamiltonian with frequency ω_k, the second one represents the linear elements which couple the two electronic states, while the third contribution contains the quadratic and bilinear terms. The quantities $\kappa_k^{(i,i)}$, $\gamma_{kl}^{(i,i)}$ and $\kappa_k^{(i,j)}$, $\gamma_{kl}^{(i,j)}$ (i≠j) are the intrastate and interstate coupling constants, respectively.

Partitioning the full Hamiltonian in (6.2.1) into a system Hamiltonian, H_{system} and a bath Hamiltonian, H_{bath} can be arbitrary:

$$H = H_{system} + H_{bath} \tag{6.2.4}$$

where

$$H_{system} = \begin{pmatrix} E_1 & 0 \\ 0 & E_2 \end{pmatrix} + H_S(y_1, y_2, ..., y_{N_S}) \tag{6.2.5}$$

and

$$H_{bath} = \sum_{k=1}^{N_B} \frac{\omega_k}{2}(p_k^2+\chi_k^2)\mathbf{1} + \sum_{k=1}^{N_B} \begin{pmatrix} \kappa_k^{(1,1)}\chi_k & \kappa_k^{(1,2)}\chi_k \\ \kappa_k^{(2,1)}\chi_k & \kappa_k^{(2,2)}\chi_k \end{pmatrix} + \frac{1}{2}\sum_{k,l=1}^{N_B} \begin{pmatrix} \gamma_{kl}^{(1,1)}\chi_k\chi_l & \gamma_{kl}^{(1,2)}\chi_k\chi_l \\ \gamma_{kl}^{(2,1)}\chi_k\chi_l & \gamma_{kl}^{(2,2)}\chi_k\chi_l \end{pmatrix} \tag{6.2.6}$$

If the system is a large polyatomic molecule, the most relevant modes can be collected into H_{system}, while the remaining part to H_{bath}. However, if the system is a small molecule embedded in an environment, the partition is apparent.

Let us decompose the operator H_{bath} into two parts. For doing so, it is useful to introduce a unitary transformation of the bath modes that splits H_{bath} into components H_{eff} and V_{bath}:

$$H_{bath} = H_{eff} + V_{bath} \tag{6.2.7}$$

In this separation, the sum of the H_{system} and H_{eff} Hamiltonians:

$$H' = H_{system} + H_{eff} \tag{6.2.8}$$

steers the short-time dynamics of the system, while the remaining part, V_{bath}, has to be taken into account only at later times. It is noticed that H_{eff} consists of only three (effective) modes, which couple the two electronic states. Let us define the elements:

$$\sum_{k=1}^{N_B} \kappa_k^{(1,1)} \chi_k = \bar{\kappa}^{(1,1)} \tilde{X}_1$$
$$\sum_{k=1}^{N_B} \kappa_k^{(1,2)} \chi_k = \sum_{k=1}^{N_B} \kappa_k^{(2,1)} \chi_k = \bar{\kappa}^{(1,2)} \tilde{X}_2 \tag{6.2.9}$$
$$\sum_{k=1}^{N_B} \kappa_k^{(2,2)} \chi_k = \bar{\kappa}^{(2,2)} \tilde{X}_3$$

which appear in H_{bath} as effective modes.

The expressions:

$$\bar{\kappa}^{(1,1)} = (\sum_{k=1}^{N_B} (\kappa_k^{(1,1)})^2)^{\frac{1}{2}}$$
$$\bar{\kappa}^{(1,2)} = (\sum_{k=1}^{N_B} (\kappa_k^{(1,2)})^2)^{\frac{1}{2}} \tag{6.2.10}$$
$$\bar{\kappa}^{(2,2)} = (\sum_{k=1}^{N_B} (\kappa_k^{(2,2)})^2)^{\frac{1}{2}}$$

denote the effective coupling constants [108–111]. First, they are not orthogonal to each other, secondly they do not have any physical importance either. Nevertheless, these terms can be written as linear combinations of three orthogonal modes. Their construction is as follows [108–111]:

$$\begin{aligned} (X_1, X_2, X_3)^T &= U_{3\times 3}(\tilde{X}_1, \tilde{X}_2, \tilde{X}_3)^T \\ &= U_{3\times 3} V_{3\times N_B} (\chi_1, \chi_2, ..., \chi_{N_B})^T \\ &= T_{3\times N_B} (\chi_1, \chi_2, ..., \chi_{N_B})^T \end{aligned} \tag{6.2.11}$$

Here, the X_1, X_2, and X_3 vectors are normalized and orthogonal to each other and $U_{3\times 3}$ is a matrix that orthogonalizes the X_l (l=1,2,3) modes. Combining $U_{3\times 3}$ with the matrix $V_{3\times N_B}$, one can obtain the $T_{3\times N_B}$ transformation matrix ($U_{3\times 3}^{-1} = V_{3\times N_B}\ T_{3\times N_B}^T$) between the initial environmental modes and the corresponding orthonormalized ones. The $V_{3\times N_B}$ transformation matrix gives the connection between the initial environmental modes and the intermediate normalized ones:

$$(\tilde{X}_1, \tilde{X}_2, \tilde{X}_3)^T = V_{3\times N_B}(\chi_1, \chi_2, ..., \chi_{N_B})^T \tag{6.2.12}$$

where

$$V_{3\times N_B} = \begin{pmatrix} \frac{\kappa_1^{(1,1)}}{\bar{\kappa}^{(1,1)}} & \cdots & \frac{\kappa_{N_B}^{(1,1)}}{\bar{\kappa}^{(1,1)}} \\ \frac{\kappa_1^{(1,2)}}{\bar{\kappa}^{(1,2)}} & \cdots & \frac{\kappa_{N_B}^{(1,2)}}{\bar{\kappa}^{(1,2)}} \\ \frac{\kappa_1^{(2,2)}}{\bar{\kappa}^{(2,2)}} & \cdots & \frac{\kappa_{N_B}^{(2,2)}}{\bar{\kappa}^{(2,2)}} \end{pmatrix} \quad . \tag{6.2.13}$$

By applying the transformation $\mathrm{T}_{3\times N_B}$ to the original modes of the environment, the expressions $\sum_{k=1}^{N_B} \kappa_k^{(i,j)} \chi_k$ and $(1/2)\sum_{k,l=1}^{N_B} \gamma_{kl}^{(i,j)} \chi_k \chi_l$ of H_{bath} in (6.2.6) can be written as:

$$\sum_{k=1}^{N_B} \kappa_k^{(i,j)} \chi_k = \bar{\kappa}^{(i,j)} \sum_{k=1}^{3} K_k^{(i,j)} X_k \tag{6.2.14}$$

$$\frac{1}{2}\sum_{k,l=1}^{N_B} \gamma_{kl}^{(i,j)} \chi_k \chi_l = \sum_{k=1}^{N_B} \frac{d_{kk}^{(i,j)}}{2} X_k^2 + \sum_{\substack{k,l=1 \\ k<l}}^{N_B} d_{kl}^{(i,j)} X_k X_l \tag{6.2.15}$$

with the coefficients $\mathrm{K}_k^{(i,j)}$ and $\mathrm{d}_{kl}^{(i,j)}$ given by:

$$K_k^{(i,j)} = \sum_{l=1}^{N_B} \frac{\kappa_l^{(i,j)}}{\bar{\kappa}^{(1,1)}} t_{kl} \qquad \text{and} \qquad d_{kl}^{(i,j)} = \sum_{m,m'=1}^{N_B} \gamma_{mm'}^{(i,j)} t_{km} t_{lm'} \tag{6.2.16}$$

where t_{kl} is the element of the matrix $\mathrm{T}_{3\times N_B}$. It can be proved that the resulting forms of H_{eff} and V_{bath} in (6.2.7) are given as follows:

$$H_{eff}^{(i,j)} = \epsilon_{eff}^{(i,j)} + H_A^{(i,j)} + H_B^{(i,j)} + H_C^{(i,j)} + H_D^{(i,j)} + H_E^{(i,j)} \tag{6.2.17}$$

$$V_{bath}^{(i,j)} = \epsilon_{bath}^{(i,j)} + H_b^{(i,j)} + H_c^{(i,j)} + H_d^{(i,j)} + H_e^{(i,j)} \quad . \tag{6.2.18}$$

A detailed description of the different componets in (6.2.17) and (6.2.18) can be found in publication [I]. More on this subject is provided in Ref. [123] and in the supplementary material of publication [I] as well.

It is worth noting here that only three modes form the H_{eff} Hamiltonian. The remaining N_B-3 modes (N_B is the number of bath modes) of the environment are collected in V_{bath}. In the calculations V_{bath} is often taken out completely (like in our case too), since it does not couple directly to the electronic subsystem.

6.3 Results for the butatriene molecule

To show the viability of the QVC three-effective-mode method, one has to find a numerically solvable sample system. For this purpose, the butatriene molecule (C_4H_4; point group: D_{2h}) was chosen as a showcase example. The first two bands of its photoelectron spectrum have been analyzed *ab initio* in Ref. [124] using the 18-mode QVC Hamiltonian and the vibronic structure of the corresponding experimental bands have been reproduced remarkably well. In particular, for low vibronic energies (corresponding to the electronic ground state of the radical cation), a regular progression of the torsional mode was observed, which reflects the twisted equilibrium structure of the radical cation. For higher energies (corresponding to the first excited electronic state), this structure becomes irregular owing to a conical intersection.

Geometry parameters of the various characteristic points of the potential energy surfaces (minima, saddle points, and the conical intersection) have been obtained and discussed in Ref. [124]. From the good agreement between experimental and theoretical photoelectron spectra, one can conclude that these data give a faithful representation of the two states of the radical cation. This underlines the flexibility of the QVC model and its ability to reproduce complex potential energy surfaces as well.

The full 18-mode QVC Hamiltonian is presented in Ref. [124]. In our decomposition of $H = H_{system} + H_{bath}$ and $H_{bath} = H_{eff} + V_{bath}$, we put all the 18 modes of the molecule into H_{bath}. It means that all the vibrational modes are subsummed into the bath part, such that the system part corresponds to the bare electronic subsystem. Therefore, we deal with a zero ($N_S = 0$) number of system modes and only three effective modes describe the short-time dynamics of this molecule.

In our investigations the focus is on the autocorrelation functions, the photoelectron

spectra and the diabatic populations. The autocorrelation was calculated according to:

$$C(t) =< 0|\exp(-iHt)|0 > \tag{6.3.1}$$

while the photoelectron spectrum is given by the Fourier transform of the autocorrelation function obtained from a long propagation in real time. For the diabatic state populations the following formula was applied:

$$L^{(q)}(t) =< \psi^{(q)}(t)|\psi^{(q)}(t) > \tag{6.3.2}$$

where $L^{(q)}(t)$ is the probability of being on the ground (q=G) or excited (q=E) state diabatic surface and $\psi^{(q)}$ is the diabatic nuclear wavefunction for the ground (q=G) or excited (q=E) electronic state.

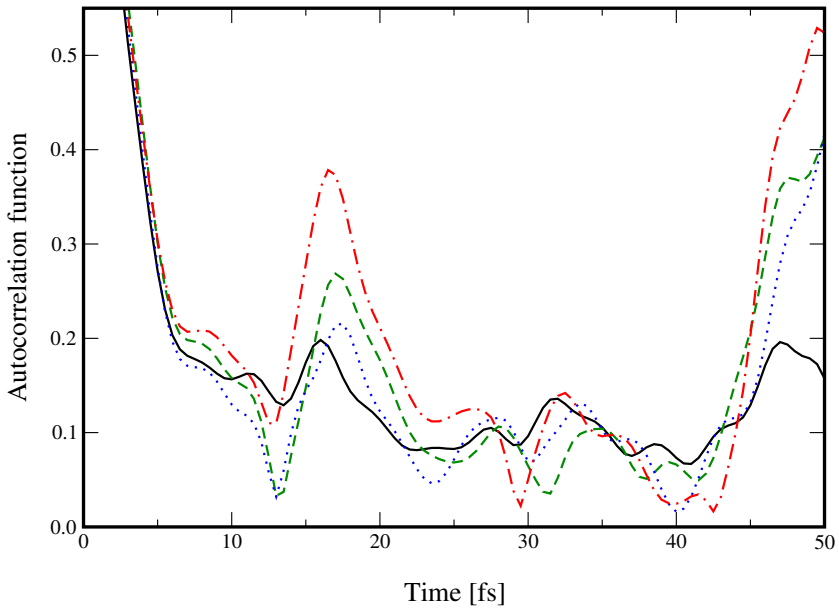

Figure 31: Autocorrelation functions for the butatriene molecule up to 50 fs. The D_1 state is initially excited. Solid line: exact 18-mode result. Dashed line: result for the linear vibronic coupling model (5-mode). Dotted line: result for the three-effective-mode model. Dash-dotted line: result for our quadratically extended three-effective-mode approach.

Four different computations were done and compared to each other: (A) an exact calculation based on the QVC Hamiltonian taking into account all the 18 modes of butatriene [124], which serves us as a reference; (B) a calculation where only the LVC part of the Hamiltonian was used. For this situation, due to symmetry, only five vibrational modes are relevant. The

coupling parameters for the LVC and QVC calculations were taken from Ref. [124]; (C) a calculation using the effective-mode method based on the LVC Hamiltonian. Here, only three effective modes were considered to describe the short-time dynamics; (D) a calculation with our effective-mode formalism based on the QVC Hamiltonian [123]. These modes are, of course, different from those used in (C) as they come from different Hamiltonians. All the calculations are performed for the initial excitation of the upper (D_1) state.

Fig. 31 shows the autocorrelation functions up to 50 fs for the four different calculations described above, which are abbreviated as the 18-mode, 5-mode, 3(LVC)-mode and 3(QVC)-mode cases, respectively. By comparing the curves, we notice that all of them are in pretty good agreement up to 6 fs and then they continue more or less similar to each other up to 12 fs. The 3(QVC)-mode curve is in reasonably good agreement with the 18-mode one up to 14 fs. The other two curves, the 5-mode and 3(LVC)-mode go together up to 14 fs, but they deviate from the former two.

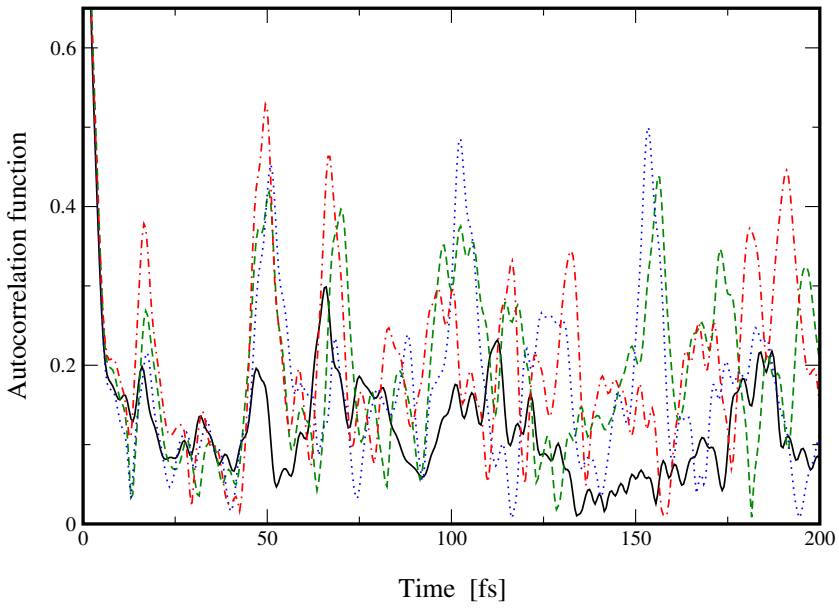

Figure 32: Autocorrelation functions for the butatriene molecule up to 200 fs. The definition of the different curves is the same as in Fig. 31.

Then, at around 14 fs, a recurrence occurs between ca. 14-20 fs for each of the four functions. This recurrence is the smallest for the 18-mode curve and largest for the 3(QVC)-mode one. At longer times, after 20 fs the curves go again roughly together on the same interval up to 43 fs and a recurrence occurs again from 43 fs onward. To see the structure of

the autocorrelation functions for a longer time period, the same kind of curves are presented in Fig. 32 until 200 fs.

We conclude that overall the 3(QVC) approach is slightly better on a very short time scale, but after 12-14 fs, the structure of its curve only roughly follows the shape of the other two (5-mode and 3(LVC)-mode) approximations. It qualitatively reproduces the result of the exact short-time dynamics of the 18-mode calculation for propagation times of 14-43 fs. After 60 fs this tendency holds again. Overall, we see a slight improvement in the structure of the 3(QVC)-mode function and it reproduces the global shape of the 18-mode curve with a reasonable accuracy.

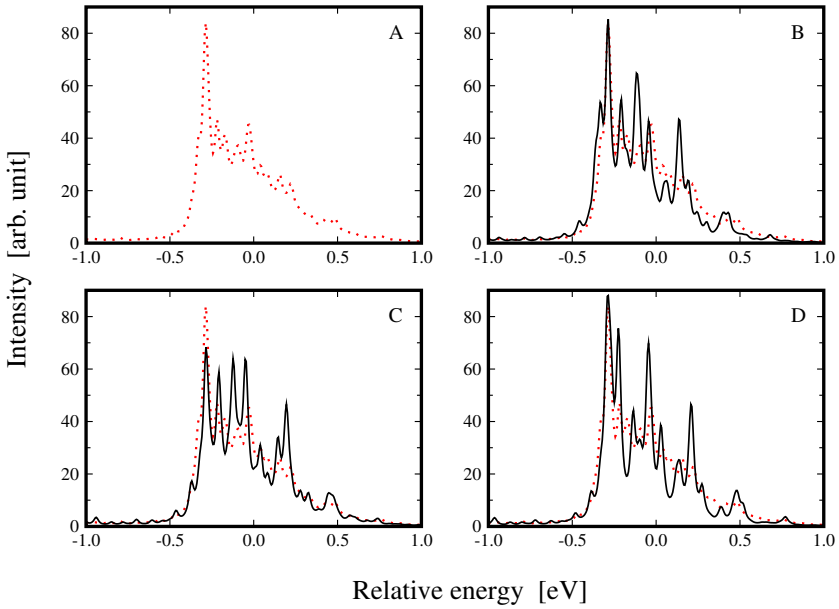

Figure 33: Spectra for the butatriene molecule. All panels display the result for the exact 18-mode model (with dotted lines in the background). Panel A: result for the exact 18-mode model. Panel B: result for the linear vibronic coupling model (5-mode). Panel C: result for the three-effective-mode model. Panel D: result for our quadratically extended three-effective-mode approach.

In panels (A)-(D) of Fig. 33, the photoelectron spectrum is presented for the four models. In Fig. 33(A) the exact 18-mode curve is shown and for the sake of comparison, panels (B)-(D) also include this curve. As expected, the spectrum calculated by the 5-mode model (see Fig. 33(B)) most closely resembles the exact one. However, the global shape of the exact spectrum is also more or less reproduced by the 3(QVC)-mode formula. Some oscillations appear in particular within the -0.1-0.2 eV interval, but the picture is definitely closer to the

exact one than that obtained by the 3(LVC)-mode approach (see Fig. 33(C)). Apart from these oscillations, one can see that the position of the maximum, the width, and even the main asymmetry of the spectrum are qualitatively reproduced by the present method.

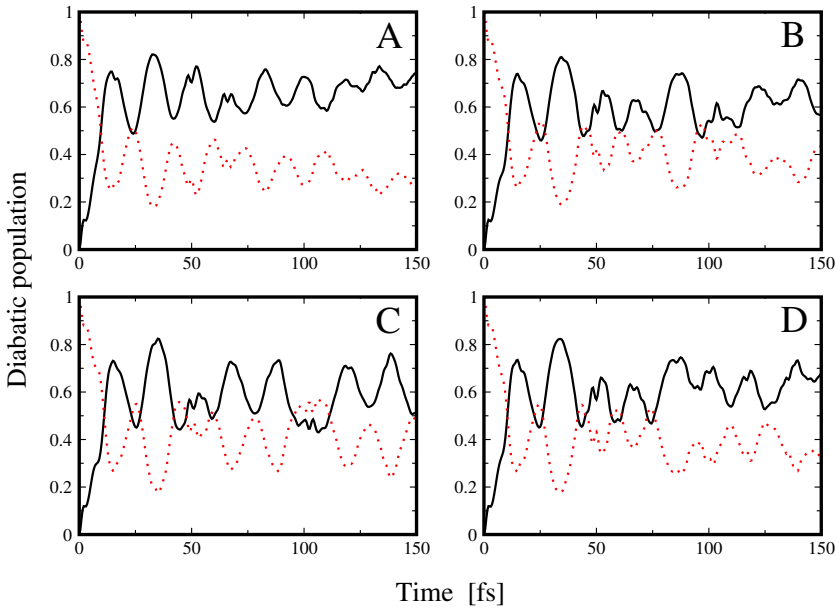

Figure 34: Diabatic state populations for butatriene as a function of time. The D_1 state is initially excited. Population for the lower state D_0 (solid line) and for the upper state D_1 (dotted line) are presented. Panel A: exact 18-mode model. Panel B: linear vibronic coupling model (5-mode). Panel C: three-effective-mode approach. Panel D: quadratically extended three-effective-mode approach.

The diabatic populations of the two electronic states (X^2B_{2g} and A^2B_{2u}) are depicted as a function of time in Fig. 34. Each panel shows the diabatic lower (X^2B_{2g}) and diabatic upper (A^2B_{2u}) states for one particular case among the four studied ones. We notice, however, that there is practically no difference between the curves up to 4 fs. For longer times, the pictures are different. If one compares the exact result (panel (A)) with that of the 3(QVC)-mode (panel (D)), a very good agreement concerning the shape of the functions up to 75 fs can be seen, but the values are shifted to each other moderately. For longer times, the 3(QVC)-mode curves show a more structured shape but still not far from the exact 18-mode one. The results given by the methods of the 5-mode (panel (B)) and 3(QVC)-mode are also in excellent agreement up to 90 fs.

In the effective-mode dynamical study carried out for the butatriene molecule, I implemented the effective Hamiltonian given for the description of the short-time dynamics. Using this Hamiltonian, I simulated nuclear wavepacket propagations and calculated the autocorrelation function, the spectra and the diabatic state populations. For the sake of comparison, I repeated the above procedure for other model Hamiltonians as well (including the exact one).

Summary

In this Thesis, nonadiabatic properties of molecular systems have been investigated by means of theoretical tools. Nonadiabatic processes, emerging from the break-down of the widely used Born-Oppenheimer approximation are the source of numerous interesting phenomena in nature. Their investigation requires high-level numerical techniques both for the electronic structure problems and the nuclear dynamics studies. Therefore it is a real challange to provide reliable results in situations of this kind, namely when electronic states cross each other. The whole work was thus centered around features related to degeneracies in the electronic structure of molecules. Extensive numerical calculations were provided as for confirmation of my new findings presented in this Thesis. The present work is based on six publications (see Publication list) which can be divided into three main subjects:

A) Three publications ([II]–[IV]) are concerned about topological features of small molecules (systems with 3 and 4 atoms). In publication [II] I studied some interesting topological properties of the H_2CN molecule when this system is distorted from the linear configuration losing its Renner-Teller character. To do this, the topological line integral method was used. To summarize my findings the followings can be said: (i) I determined accurately the positions of the two conical intersections between the two lowest states of the bent H_2CN molecule which are located out of the molecular plane; (ii) the nonadiabatic coupling terms and the corresponding topological (or Berry) phase, surrounding either a single CI point from the pair of CIs or both CIs, were calculated. In all cases the values of the Berry phases were equal to π or 2π depending on the radii of the circles along which the calculations were performed. If the radius was small enough to surround only a single CI point from the pair of CIs, then $\alpha=\pi$, in other cases $\alpha=2\pi$ was given. With this, it has been shown undoubtedly that - in all the situations investigated so far - after losing the Renner-Teller character in a molecular system always two single CIs are formed; (iii) in addition, I could show that the *ab initio* nonadiabatic coupling terms can be approximated very well using the vector-algebra approach with the flat 'virgin' distribution for both CIs.

Publications [III] and [IV] are closely related. In those works, a detailed topological study has been carried out for the tri-atomic $F+H_2$ molecule. This system possesses two kinds of degeneracies (along its collinear axis), namely Renner-Teller and Jahn-Teller type intersections. The principal goal of these works was to introduce a theory for the description

of the entanglement between the above-mentioned (RT and JT) degeneracies and to provide numerical calculations so as to verify the applicability of the approach. Earlier studies demonstrated that the two-state approximation does not give satisfactory results for $F+H_2$ in the desired chemical volume, namely quantized topological phases were obtained only for small circular contours. This implies the need for including some more electronic states in the treatment. In the case that more than two states are involved, the line integral method is not applicable and the ADT matrices has to be considered instead. The theory presented in [III] indeed deals with the ADT matrices and the tri-state and four-state situations are incorporated (by including two and three A' states along with an A" state). Finally a formula is derived for calculating the so-called privileged ADT angle for which the end-of-contour value is associated with the topological phase. The numerical studies provided quantized topological phases in a large domain confirming the viability of the approach developed for the RT/JT effect. Making use of the encouraging results of [III], I was able to derive exact diabatic potential energy surfaces for the subject system in publication [IV]. Based on the diabatic potentials I calculated dressed adiabatic potentials and compared to dressed potentials obtained directly from adiabatic potentials. By doing so I got insight into the low energy dynamics of $F+H_2$. Since the two kinds of dressed potentials differed significantly near the equilibrium arrangement, I could conclude that topological effects strongly influence processes on the lower adiabatic surface, thus implying that the BO approximation is not valid for the studied system.

B) Two of the six publications ([V] and [VI]) are about the investigation of molecular switch properties for several compounds. The operation of molecular switch systems is based on low-lying electronic potential energy surfaces and one of their main criteria is the presence of degeneracy between (usually) the ground and first excited states. Hence the function of switch systems is a typical nonadiabatic process which can be used, for instance, for high density data storage. In paper [V] I have studied two pyrimidine derivatives (NPE and PQol) as possible photo-switch systems. I investigated excited state intramolecular hydrogen transfer process, promoted by twisting around the covalent bond that connects the crane and frame parts of each molecule, as photochemical mechanism by which the two conformers of both NPE and PQol can isomerize. Based on this concept detailed numerical electronic structure studies have been performed. The ground state equilibrium geometries of both stable forms, the potential energy functions of the six lowest-lying singlet states along hypo-

thetical reaction pathways, oscillator strengths and dipole moments were calculated along with other properties. The analysis of the results obtained for both systems so far indicates that PQol and NPE are ineffective photo-switch systems. However, it is still possible that more extended studies may in fact reveal that PQol and NPE are interesting photo-switch systems, but based on the present status of the study, this does not seem likely. Making use of the experience gained in this work (concerning the applied electronic structure methods, basis sets and the formation of the pathways etc.) I continued studying switch features. In publication [VI] I carried out an extensive study by investigating systematically the impact of chemical substitutions on the molecular photo-switch properties of several quinoline compounds. My results undoubtedly indicate that the studied systems possess a number of switch features, namely: all the six molecules exhibit two minima on the ground state PES which are separated from each other by a sufficiently large energy barrier. The excitation energies of the lowest excited states differ significantly in the two terminal geometries of the investigated ESIHT reaction paths. It was revealed that the S_1 state of 7HQ8CB and 4A7HQ8CB can't be excited directly from S_0. In case of the 7HQ8CC and 4A7HQ8CC molecules, S_1 of the enol forms can be populated directly while the keto only indirectly. I have explored the PESs of the ground and first excited states along the ESIHT path. It was found that carboxyboryl and carboxycyanide cranes result in a pronounced increase of the S_0 surface around a perpendicular twist. An amide group attached to the frame was shown to have only a small effect on the PESs eventuating slightly shifted energies. The existence of conical intersections near 90 degree distortion has been revealed for the six molecules. According to the potential energy landscapes, one can expect that the 7HQ8CA/4A7HQ8CA and 7HQ8CC/4A7HQ8CC pairs will probably be switchable only in one direction (enol$\rightarrow$ keto) while the 7HQ8CB/4A7HQ8CB pair is most likely suitable for reversible switching. However, in order to fully confirm the predictions concerning the photo-switch behaviour of the studied molecules, quantum dynamical calculations on the S_0 and S_1 electronic surfaces are necessary, which can be the subject of a future work.

C) One of the publications ([I]) deals with quantum dynamical studies. In this paper a new approach has been developed to investigate the short-time dynamics of large polyatomic molecules or molecule-environment systems at conical intersections. This approach is based on the QVC Hamiltonian and the effective-mode formalism. It can be considered as one possible extension of the earlier developed three-effective-mode scheme corresponding to the

LVC Hamiltonian. In both methods, the complex system is split into system modes and an environment. It has already been shown that the short-time dynamics of the full system can reasonably be described by applying the system modes, supplemented by only three effective modes. By using a suitable orthogonal transformation, these effective coordinates can be extracted from the environmental modes. It is known that the short-time dynamics is controlled by the first few cumulants. By performing a cumulant expansion of the autocorrelation function, one can recover the exact cumulants up to second order. That is, the zeroth-, first-, and second-order cumulants of H (6.2.6) and H' (6.2.8) are identical. This fact ensures that, with the application of the operator, H' in the actual calculations, the intensity, the center of gravity and the width of the spectrum can be reproduced accurately. It has to be mentioned that this kind of conservation of the cumulants holds up to third order when one considers the LVC three-effective-mode decomposition. I investigated the butatriene molecule as a showcase example. Fortunately, I was able to perform exact numerical calculations for this system using the MCTDH method to compute the dynamics of all 18 modes. Four different kinds of calculations were performed (among them the afore-mentioned exact one) and compared to each other. One of the main outcomes of this comparative analysis is that the present QVC three-effective-mode scheme reproduces the short-time dynamics and the overall shape of the spectra with a reasonable accuracy. Namely, the autocorrelation function is more accurate up to the first 14 fs, compared to that derived from the LVC three-effective-mode approach. The results for the diabatic populations given by the QVC three-effective-mode scheme are excellent up to 75 fs.

As a final conclusion, I can say that the initial goals have been successfully achieved and an extensive and comprehensive theoretical study of nonadiabatic properties has been presented in this Thesis.

Összefoglalás

Doktori tanulmányaim során molekulák nemadiabatikus tulajdonságainak elméleti vizsgálatával foglalkoztam. A nemadiabatikus folyamatok tárgykörébe a Born-Oppenheimer-közelítés keretein túlmutató jelenségek tartoznak, melyek számos érdekes folyamat forrásai a természetben. Nemadiabatikus tulajdonságok vizsgálata során pontos elektronszerkezeti és magdinamikai számolásokra van szükség, ezért külön nehézséget jelent ezen sajátságok korrekt leírása. Dolgozatom tehát az elektronállapotok kereszteződési pontjainak (degenerációk) tanulmányozása köré összpontosult. Munkám során numerikus módszerekkel kis molekulák elektronszerkezeti topológiáját vizsgáltam, molekuláris kapcsoló tulajdonságokat tanulmányoztam, illetve atommagok dinamikai leírásával is foglalkoztam. Ennek megfelelően a dolgozat alapjául szolgáló hat publikáció három fő csoportra osztható:

A) Három közleményben ([II]-[IV]) kis rendszerek (3 és 4 atomos) elektronszerkezetében fellépő topológiai effektusokat vizsgáltam. A [II]-es publikációban azt tanulmányoztam, hogy mi történik ha a Renner-Teller-típusú H_2CN molekulát kimozdítjuk a lineáris elrendeződésből és ezáltal elveszíti RT-karakterét. Vizsgálataimhoz a topológiai vonalintegrál módszert használtam, melynek főbb eredményeit a következő pontokban lehet összefoglalni: (i) A kimozdítást követően az alap és az első gerjesztett állapot között keletkező két kónikus kereszteződés (CI) pozícióját pontosan meghatároztam. Ezek a kereszteződések a molekulasík alatt, illetve felett szimmetrikusan helyezkednek el. (ii) Kiszámoltam a nemadiabatikus csatolási tagokat és a topológiai (vagy Berry) fázist arra az esetre, amikor csak egy CI-t, illetve arra az esetre is amikor mindkét CI-t körbevesszük az integrálások során. A Berry-fázis értékére minden esetben π, vagy 2π értékeket kaptam, attól függően, hogy az integrálás során bejárt kör sugara mekkora volt. Ha a sugár elegendően kicsi volt ahhoz, hogy a két CI közül csak egyet vegyen körbe a kör, akkor $\alpha = \pi$, más esetekben $\alpha = 2\pi$ értékeket kaptam. Ezek az eredmények egyértelmű bizonyítékai annak, hogy a Renner-Teller-karakter elvesztését követően mindig két CI keletkezik a rendszerben. (iii) Ezeken túlmenően sikerült belátnom, hogy az *ab initio* számolásokból nyert nemadiabatikus csatolási tagok nagyon jól közelíthetők egy a közelmúltban kidolgozott, ún. vektor-algebra módszer segítségével.

A [III]-as és [IV]-es publikációk szorosan összefűződnek. Ezekben a munkákban a háromatomos $F+H_2$ rendszerre vonatkozóan végeztem részletes topológiai vizsgálatokat. Ebben a molekulában Renner-Teller- és Jahn-Teller-típusú kereszteződések egyaránt jelen vannak a

kollineáris elrendeződés mentén. Munkám során a cél egy olyan elmélet bevezetése volt, mely képes leírni az imént említett elfajulások csatolódását. Az új módszer helyességét pedig numerikus számolásokkal kívántam alátámasztani. Korábbi publikációkban bebizonyították, hogy a kétállapot közelítés nem ad pontos eredményt az $F+H_2$ rendszer esetén (csak kis sugarú körök mentén kaptak kvantált topológiai fázist), amiből arra lehet következtetni, hogy további állapotok bevonására van szükség. Ezen a vonalon indultunk el a [III]-as munkában. Kettőnél több állapot esetén nem alkalmazható a vonalintegrál módszer, ehelyett az ADT mátrix bevezetésére van szükség. A bemutatott módszert három- és négyállapot közelítésre terjesztettük ki (egy A" állapot mellett két, illetve három A' állapot figyelembevételével), minek eredményeképpen formulákat kaptunk egy ún. kitüntetett ADT szög származtatására, melynek értéke a teljes körbejárást követően megfeleltethető a topológiai fázisnak. Ezt követően a numerikus számolások már nagy geometria tartományban is kvantált topológiai fázist szolgáltattak, amiből az elmélet létjogosultságára következtethetünk. A [III]-ban számolt topológia szögek segítségével lehetőség nyílt pontos diabatikus potenciális energia felületek számolására, melyeket a [IV]-es közleményben prezentáltunk. Ahhoz, hogy betekintést nyerjünk molekulák alacsony energiájú dinamikájába, ún. "dressed" potenciálok vizsgálata szükséges. Az adiabatikus felületekből számolt "dressed" potenciálokat összehasonlítva a "dressed" diabatikus felületekből származtatott adiabatikusokkal, arra a következtetésre jutottam (a számottevő eltérés alapján), hogy a topológiai effektusok jelentősen befolyásolják a rendszer alsó adiabatikus felületén lejátszódó folyamatokat, tehát a BO-közelítés minden bizonnyal érvényét veszti.

B) Két publikáció a hatból ([V] és [VI]) molekuláris kapcsoló tulajdonságok vizsgálatával foglalkozik. A molekuláris kapcsolók működése alacsonyan fekvő potenciális energia felületek közti kereszteződésen alapul, ezáltal tipikus nemadiabatikus jelenség. A kapcsoló molekulák számos gyakorlati alkalmazási lehetőséggel bírnak, melyek közül az egyik legfontosabb talán az, hogy nagy sűrűségű adattárolást tesznek lehetővé. Informatikai alkalmazási lehetőségük ezáltal kiemelten fontos a jövőre nézve. Az [V]-ös közleményben két pirimidin-származék (NPE és PQol) kapcsoló tulajdonságait tanulmányoztam. Fotokémiai reakcióútnak az ún. gerjesztett állapoton keresztül történő intramolekuláris hidrogén transzfer (ESIHT) folyamatot tekintettem, melynek eredményeképpen mindkét rendszerben megtörténhet az átmenet a stabil izomerek között. Részletes elektronszerkezeti vizsgálatokat végeztem az említett rendszerekre, melynek során alapállapoti egyensúlyi geometriákat, oszcillátor erősségeket,

dipólmomentumokat és gerjesztési energiákat is számoltam. A reakcióút függvényében vizsgált potenciális energia profil a hat legalacsonyabban fekvő szinglett állapotot tartalmazta, melyek között nem találtam kónikus kereszteződéseket és az eredmények további elemzése arra vezetett, hogy sem NPE, sem PQol nem alkalmasak kapcsoló molekulának a jelenlegi álláspont szerint. A szerzett tapasztalatokat felhasználva (az elektronszerkezeti módszereket, a bázisfüggvényeket, a reakcióút felépítését illetően stb.) tovább folytattam kutatásaimat molekuláris kapcsoló vonalon.

A [VI]-os publikációban kinolin-származékok különböző funkciós csoportjainak a kapcsoló tulajdonságokra gyakorolt hatását tanulmányoztam. A szisztematikus vizsgálat során számos kapcsoló sajátságra fény derült: Mind a hat molekula rendelkezik két stabil, egymástól jól elszeparált minimummal az alapállapot energia felületén. Ezen stabilis izomerek, melyek a már említett ESIHT folyamat végpontjait jelentik, jól megkülönböztethető gerjesztési energia spektrummal rendelkeznek. Az alapállapothoz viszonyított átmeneti valószínűségekről kiderült, hogy két rendszerben (7HQ8CB és 4A7HQ8CB) az S_1 állapot csak közvetve gerjeszthető, míg a 7HQ8CC és 4A7HQ8CC molekulák esetén ez csak a keto konformerekre igaz. Az alap és az első gerjesztett állapotok potenciális energia profiljait vizsgálva (az ESIHT folyamat mentén) azt találtam, hogy a karboxboril és karboxcianid csoportokat (az ún. "crane" pozícióban) tartalmazó rendszerekben az alapállapot profilja jelentősen megemelkedik a merőleges elfordulás környezetében. Beláttam, hogy az ún. "frame" részhez kötött amid csoportoknak nincs jelentős szerepe a kapcsoló tulajdonságokban, csupán nagyon kicsi eltolódást (< 0.1 eV) okoznak az energiákban. Mind a hat molekulában sikerült kónikus kereszteződést találnom a 90 fokos elfordulások közelében. A kapott potenciális energia profilok alapján nagy valószínűséggel a 7HQ8CA/4A7HQ8CA és 7HQ8CC/4A7HQ8CC rendszerek egyirányban billenthetők (enol→keto), míg a 7HQ8CB és 4A7HQ8CB molekulák reverzibilis kapcsolásra is képesek. A vizsgált rendszerek kapcsoló tulajdonságaira tett jóslatainkat dinamikai számolások tudják teljes körűen megerősíteni, ami a sok szabadsági fok miatt nagy kihívást jelent és egy jövőbeni publikáció tárgya lehet.

C) Egy közleményem ([I]) molekuláris kvantum dinamikával foglalkozik. Ebben a munkában egy új módszer került bemutatásra nagy molekulák (vagy környzetbe ágyazott kis rendszerek) kónikus kereszteződésen keresztül lejátszódó rövid távú dinamikai folyamatainak leírására. A módszer alapját a QVC ("quadratic vibronic coupling") Hamilton-operátor és az ún. három effektív módus modell képezik. Lényegében a már korábban publikált,

LVC ("linear vibronic coupling") Hamilton-operátoron alapuló három effektív módus modell egy továbbfejlesztett változatának tekinthető. Mindkét esetben a teljes rendszer Hamilton-operátorát felosztjuk ún. rendszer és környezet részre, majd pedig egy ortogonális transzformáció bevezetésével a környezet Hamilton-operátorának a további particionálása történik meg. Eredményül három effektív módus adódik, melyek a rendszert jellemző Hamilton-operátorral együtt írják le óriás molekulák (vagy kis rendszer és környezet) rövid távú, nagyon gyors dinamikai folyamatait. Az irodalomból ismert, hogy a rövid távú dinamikát az autokorrelációs függvény logaritmusának t = 0-nál vett sorfejtésében megjelenő első néhány együttható - kumuláns - határozza meg. Az autokorrelációs függvény és a spektrum szoros kapcsolata miatt a kumulánsok információt hordoznak a spektrum megfigyelhető sajátságairól. A QVC három effektív módus modell H' (6.2.8) operátora másod rendig megtartja az egzakt H-hoz (6.2.6) tartozó valószínűségeloszlást (azaz H'-t használva visszakapjuk a spektrum teljes intenzitását, súlypontját és szélességét). Az LVC három effektív modellben az egyezés harmad rendig bizonyítható. A kifejlesztett módszer tesztelésére a butatrién molekulát választottam. A 18 módussal rendelkező butatrién esetén egzakt számolásokat is képes voltam kivitelezni az MCTDH algoritmus segítségével. Vizsgálataim során négy különböző módszert hasonlítottam össze. A numerikus számolások legfontosabb eredménye, hogy a QVC három effektív módus modell megfelelő pontossággal leírja a rövid távú dinamikát és a spektrum alakját. Az autokorrelációs függvény 14 fs-ig pontosabb az LVC három effektív modell eredményénél. A diabatikus betöltöttségeket illetően az egzakt leíráshoz viszonyítva 75 fs-ig nagyon jó egyezést kaptam.

Összességében elmondható, hogy a doktori tanulmányaim kezdetén kitűzött célokat sikerült teljesítenem, aminek eredményeképpen molekulák nemadiabatikus tulajdonságainak átfogó és részletes elméleti vizsgálatáról számolhattam be a Dolgozatomban.

Acknowledgments

I would like to thank everyone who assisted during the course of completion of this Thesis. First of all I am grateful to my supervisor Gábor Halász who introduced me in the field of theoretical computational physics and helped my work with his skillful advices during the years. As my mentor, he was always ready to help me with his prompt answers, I could really learn a lot from him.

I am greatly indebted to Ágnes Vibók for the valuable discussions, the encouragements and all her guidance in the world of science. She always found the way to provide me proper working conditions.

I would like to express my thanks to Michael Baer for involving me in the electronic structure topological studies.

I would like to note my appreciation to Clemens Woywod for giving me so much help with the *ab initio* calculations in the early days.

Last but not least I owe my gratitude to my Family for supporting me all through the years.

Finally I would like to acknowledge the following financial supports: This work would not have been possible without the PhD scholarship provided by the Faculty of Informatics of the University of Debrecen. Thanks go also to the Research Center Jülich (cluster JUROPA: Project ID ehu01), NOTUR (cluster Abel) and NIIF (supercomputer in Debrecen) for providing computational resources. The Thesis was supported by the TÁMOP-4.2.2.C-11/1/KONV-2012-0001 project. The project has been supported by the European Union, co-financed by the European Social Fund.

Publication list

The Thesis is based on the following publications

[I] Á. Vibók, A. Csehi, E. Gindensperger, H. Köppel, and G. J. Halász: Quantum dynamics through conical intersections: Combining effective modes and quadratic couplings, *J. Phys. Chem. A* **116**, 2629 (2012).

[II] A. Csehi, G. J. Halász and Á. Vibók: Conical intersections in the H_2CN molecule induced by the distortion from its Renner-Teller arrangement, *Chem. Phys. Lett.* **533**, 10 (2012).

[III] A. Csehi, A. Bende, G. J. Halász, Á. Vibók, A. Das, D. Mukhopadhyay and M. Baer: A tri-atomic Renner-Teller system entangled with Jahn-Teller conical intersections, *J. Chem. Phys.* **138**, 024113 (2013).

[IV] A. Csehi, A. Bende, G. J. Halász, Á. Vibók, A. Das, D. Mukhopadhyay, S. Mukherjee, S. Adhikari and M. Baer: Dressed adiabatic and diabatic potentials for the Renner-Teller/Jahn-Teller F+H_2 system, *J. Phys. Chem. A* **117**, 8497 (2013).

[V] A. Csehi, C. Woywod, G. J. Halász, Á. Vibók: Ab initio studies of two pyrimidine derivatives as possible photo-switch systems, *Cent. Eur. J. Phys.* **11**, 1141 (2013).

[VI] A. Csehi, L. Illés, G. J. Halász, Á. Vibók: The effect of chemical substituents on the functionality of a molecular switch system: a theoretical study of several quinoline compounds, *Phys. Chem. Chem. Phys.* **15**, 18048 (2013).

Posters

1) A. Csehi, C. Woywod, Á. Vibók, G. J. Halász: Ab initio studies of two pyrimidine derivatives as possible photo-switch systems, *4th annual meeting of the COST Action CUSPFEL, 21st-23rd March 2012, Cluj, Romania.*

2) A. Csehi, E. Gindensperger, H. Köppel, G. J. Halász and Á. Vibók: Quantum dynamics through conical intersections: Combining effective modes and quadratic couplings, *High-dimensional Quantum Dynamics: Challenges and Opportunities, 12th-14th April 2012, Birmingham, England* and *4th annual meeting of the COST Action CUSPFEL, 21st-23rd March 2012, Cluj, Romania.*

3) A. Csehi, L. Illés, G. J. Halász, Á. Vibók: Theoretical investigation of molecular switch properties of several quinoline compounds, *The VIIIth Congress of the International Society of Theoretical Chemical Physics, 25th-31st August 2013, Budapest, Hungary* and *Magyar Fizikus Vándorgyűlés, 21st-24th August 2013, Debrecen, Hungary.*

REFERENCES

[1] M. Born, R. Oppenheimer, *Ann. Phys.* **84**, 457 (1927).

[2] M. Born, K. Huang, The Dynamical Theory of Crystal Lattices, Oxford University Press, New York (1954).

[3] H. Köppel, W. Domcke, L. S. Cederbaum, *Adv. Chem. Phys.* **57**, 59 (1984).

[4] M. Baer, G. D. Billing (Eds.), The Role of Degenerate States in Chemistry, *Adv. Chem. Phys.* **124**, Wiley-Interscience, New York (2002).

[5] W. Domcke, D. R. Yarkony, H. Köppel (Eds.), Conical Intersections: Electronic Structure, Dynamics and Spectroscopy, World Scientific: Singapore (2004).

[6] G. A. Worth, L. S. Cederbaum, *Annu. Rev. Phys. Chem.* **55**, 127 (2004).

[7] M. Baer (Ed.), Beyond Born-Oppenheimer: Electronic Nonadiabatic Coupling Terms and Conical Intersections, Wiley: Hoboken, NJ (2006).

[8] S. Matsika, *Rev. Comp. Chem.* **23**, 83 (2007).

[9] M. Klessinger, J. Michl (Eds.), Excited States and Photochemistry of Organic Molecules, VCH Publishers Inc., New York (1995).

[10] P. Kukura et al., *Science* **310**, 1006 (2005).

[11] S. Hahn, G. J. Stock, *J. Phys. Chem. B* **104**, 1146 (2000).

[12] T. Schultz, E. Samoylova, W. Radloff, I. V. Hertel, A. L. Sobolewski, W. Domcke, *Science* **306**, 1765 (2004).

[13] Z. Lan, L. M. Frutos, A. Sobolewski, W. Domcke, *Proc. Natl. Acad. Sci. U.S.A.* **105**, 12707 (2008).

[14] T. Andruniow, N. Ferre, M. Olivucci, *Proc. Natl. Acad. Sci. U.S.A.* **101**, 17908 (2004).

[15] M. Assmann, G. Pérez-Hernández, L. González, *J. Phys. Chem. A* **114**, 9342 (2010).

[16] M. Assmann, C. S. Sanz, G. Pérez-Hernández, G. A. Worth, L. González, *Chem. Phys.* **377**, 86 (2010).

[17] V. Leyva, I. Corral, F. Feixas, A. Migani, L. Blancafort, J. González-Vázquez, L. González, *Phys. Chem. Chem. Phys.* **13**, 14685 (2011).

[18] D. Asturiol, B. Lasorne, G. A. Worth, M. A. Robb, L. Blancafort, *Phys. Chem. Chem. Phys.* **12**, 4949 (2010).

[19] G. A. Worth, C. S. Sanz, *Phys. Chem. Chem. Phys.* **12**, 15570 (2010).

[20] D. Mendive-Tapia, B. Lasorne, G. A. Worth, M. J. Bearpark, M. A. Robb, *Phys. Chem. Chem. Phys.* **12**, 15725 (2010).

[21] G. Herzberg, H. C. Longuet-Higgins, *Discuss. Faraday Soc.* **35**, 77 (1963).

[22] H. C. Longuet-Higgins, *Proc. R. Soc. London A* **344**, 147 (1975).

[23] M. V. Berry, *Proc. R. Soc. London A* **392**, 45 (1984).

[24] E. Renner, *Z. Phys.* **92**, 172 (1934).

[25] Halász Gábor: Degenerált állapotok és nemadiabatikus folyamatok molekuláris rendszerekben. Doctor of the Hung. Acad. of Sci. thesis, in Hungarian (2012).

[26] A. Szabó, N. S. Ostlund (Eds.), Modern Quantum Chemistry (ISBN 0-07-062739-8).

[27] C. Møller, M. S. Plesset, *Phys. Rev.* **46**, 618 (1934).

[28] D. Peláez-Ruiz and H. D. Meyer, Introduction to MCTDH, lecture notes (2011).

[29] H. D. Meyer, G. A. Worth, *Theor. Chem. Acc.* **109**, 251 (2003).

[30] H. D. Meyer, U. Manthe, L. S. Cederbaum, *Chem. Phys. Lett.* **165**, 73 (1990).

[31] H. D. Meyer, F. Gatti, G. A. Worth (Eds.), Multidimensional Quantum Dynamics: MCTDH Theory and Applications, Wiley-VCH: Weinheim, Germany (2009).

[32] M. Baer, *Chem. Phys. Lett.* **35**, 112 (1975).

[33] M. Baer, *Chem. Phys.* **259**, 123 (2000).

[34] G. J. Halász, Á. Vibók, R. Baer, M. Baer, *J. Phys. A: Math. Theor.* **40**, 267 (2007).

[35] G. J. Halász, Á. Vibók, R. Baer, M. Baer, *J. Chem. Phys.* **124**, 081106 (2006).

[36] G. J. Halász, Á. Vibók, R. Baer, M. Baer, *J. Chem. Phys.* **125**, 094102 (2006).

[37] G. J. Halász, Á. Vibók, D. K. Hoffman, D. J. Kouri, M. Baer, *J. Chem. Phys.* **126**, 154309 (2007).

[38] G. J. Halász, Á. Vibók, M. Baer, *J. Chem. Phys.* **127**, 144108 (2007).

[39] T. Vértesi, R. J. Englman, *J. Phys. B: At. Mol. Opt. Phys.* **41**, 025102 (2008).

[40] G. J. Halász, Á. Vibók, *Int. J. Quant. Chem.* **111**, 342 (2011).

[41] G. J. Halász, Á. Vibók, *Chem. Phys. Lett.* **494**, 150 (2010).

[42] A. Das, D. Mukhopadhyay, S. Adhikari, M. Baer, *J. Chem. Phys.* **133**, 084107 (2010).

[43] A. Das, D. Mukhopadhyay, *J. Phys. Chem. A* **116**, 1774 (2012).

[44] A. Papp, G. J. Halász, M. C. Bacchus-Montabonel, Á. Vibók, *Chem. Phys. Lett.* **504**, 20 (2011).

[45] E. Bene, T. Vértesi, R. J. Englman, *J. Chem. Phys.* **135**, 084101 (2011).

[46] B. H. Lengsfield III, D. R. Yarkony, *Adv. Chem. Phys.* **82**, 1 (1992).

[47] B. O. Roos, *Adv. Chem. Phys.* **69**, 399 (1987).

[48] B. O. Roos, P. R. Taylor, P. E. M. Siegbahn, *Chem. Phys.* **48**, 157 (1980).

[49] H. J. Werner, *Adv. Chem. Phys.* **69**, 1 (1987).

[50] K. Ruedenberg, M. W. Schmidt, M. M. Gilbert, S. T. Elbert, *Chem. Phys.* **71**, 41 (1982).

[51] Á. Vibók, T. Vértesi, E. Bene, G. J. Halász, M. Baer, *J. Phys. Chem. A* **108**, 8590 (2004).

[52] H. Jahn and E. Teller, *Proc. Roy. Soc. A* **161**, 220 (1937).

[53] D. Golez, Jahn-Teller effect, seminar (2011).

[54] Z. H. Top and M. Baer, *J. Chem. Phys.* **66**, 1363 (1977).

[55] A. Das, D. Mukhopadhyay, S. Adhikari, M. Baer, *Int. J. Quant. Chem.* **112**, 2561 (2012).

[56] K. Stark and H. J. Werner, *J. Chem. Phys.* **104**, 6515 (1996).

[57] H. J. Werner et al., MOLPRO, Version 2012.1, A Package of ab initio Programs. Available from: <http://www.molpro.net>.

[58] A. Das, D. Mukhopadhyay, S. Adhikari and M. Baer, *Chem. Phys. Lett.* **517**, 92 (2011).

[59] A. Das, D. Mukhopadhyay, S. Adhikari and M. Baer, *Eur. Phys. J. D* **65**, 373 (2011).

[60] A. Das, T. Sahoo, D. Mukhopadhyay, S. Adhikari, M. Baer, *J. Chem. Phys.* **136**, 054104 (2012).

[61] S. H. Lipoff, D. Herschbach, *Mol. Phys.* **108**, 1133 (2010).

[62] A. L. Sobolewski, *Phys. Chem. Chem. Phys.* **10**, 1243 (2008).

[63] B. L. Feringa (Ed.), Molecular Switches, Wiley-VCH (2001).

[64] J. E. Green et al., *Nature* **445**, 414 (2007).

[65] L. Lapinski, M. J. Nowak, J. Nowacki, M. F. Rode, A. L. Sobolewski, *ChemPhysChem* **10**, 2290 (2009).

[66] M. F. Rode, A. L. Sobolewski, *J. Phys. Chem. A* **114**, 11879 (2010).

[67] A. Aviram, M. A. Ratner, *Chem. Phys. Lett.* **29**, 277 (1974).

[68] J. Chen, M. A. Reed, A. M. Rawlett, J. M. Tour, *Science* **286**, 1550 (1999).

[69] Z. Yao, H. W. C. Postman, L. Balents, C. Dekker, *Nature* **406**, 273 (1999).

[70] P. R. Hania, R. Telesca, L. N. Lucas, A. Pugzlys, J. van Esch, B. L. Feringa, J. G. Snijders, K. Duppen, *J. Phys. Chem. A* **106**, 8498 (2002).

[71] D. Guillaumont, T. Kobayashi, K. Kanda, H. Miyasaka, K. Uchida, S. Kobatake, K. Shibata,

S. Nakamura, M. Irie, *J. Phys. Chem. A* **106**, 7222 (2002).

[72] D. Dulic, S. J. van der Molen, T. Kudernac, H. T. Jonkman, J. J. D. De Jong, T. N. Bowden, J. van Esch, B. L. Feringa, B. J. van Wees, *Phys. Rev. Lett.* **91**, 207402 (2003).

[73] J. Li, G. Speyer, O. Sankey, *Phys. Rev. Lett.* **93**, 248302 (2004).

[74] M. Zhuang, M. Ernzerhof, *Phys. Rev. B* **72**, 073104 (2005).

[75] C. J. Barrett, J. Mamiya, K. G. Yagerc, T. Ikeda, *Soft Matter* **3**, 1249 (2007).

[76] H. Tamura, S. Nanbu, T. Ishida, H. Nakamura, *J. Chem. Phys.* **125**, 034307 (2006).

[77] B. L. Feringa, W. F. Jager, B. Delange, E. W. Meijer, *J. Am. Chem. Soc.* **113**, 5468 (1991).

[78] B. L. Feringa, W. F. Jager, B. Delange, *Tetrahedron* **49**, 8267 (1993).

[79] W. R. Browne, B. L. Feringa, *Annu. Rev. Phys. Chem.* **60**, 407 (2009).

[80] N. Katsonis, T. Kudernac, M. Walko, S. J. van der Molen, B. J. van Wees, B. L. Feringa, *Adv. Mater.* **18**, 1397 (2006).

[81] A. J. Kronemeijer, H. B. Akkerman, T. Kudernac et al., *Adv. Mater.* **20**, 1467 (2008).

[82] B. L. Feringa, N. P. M. Huck, H. A. Vandoren, *J. Am. Chem. Soc.* **117**, 9929 (1995).

[83] R. A. van Delden, N. Koumura, N. Harada, B. L. Feringa, *Proc. Natl. Acad. Sci. U.S.A.* **99**, 4945 (2002).

[84] D. Pijper, M. G. M. Jongejan, A. Meetsmia, B. L. Feringa, *J. Am. Chem. Soc.* **130**, 4541 (2008).

[85] W. R. Browne, B. L. Feringa, *Nature Nanotechnology* **1**, 25 (2006).

[86] T. Kudernac, S. J. van der Molen, B. J. van Wees, B. L. Feringa, *Chem.Commun.* **34**, 3597 (2006).

[87] S. J. van der Molen, H. van der Vegte, T. Kudernac, I. Amin, B. L. Feringa, B. J. van Wees, *Nanotechnology* **17**, 310 (2006).

[88] B. L. Feringa, *J. Org. Chem.* **72**, 6635 (2007).

[89] W. Wu et al., *Appl. Phys. A* **80**, 1173 (2005).

[90] J. F. Scott, C. A. Paz de Araujo, *Science* **246**, 1400 (1989).

[91] Y. Chen et al., *Nanotechnology* **14**, 462 (2003).

[92] G. Snider, P. Kuekes, T. Hogg and R. S. Williams, *Appl. Phys. A* **80**, 1183 (2005).

[93] A. DeHon, S. C. Goldstein, P. J. Kuekes and P. Lincoln, *IEEE Trans. Nanotechnol.* **4**, 215 (2005).

[94] N. A. Melosh et al., *Science* **300**, 112 (2003).

[95] R. Waser and A. Rudiger, *Nature Mater.* **3**, 81 (2004).

[96] J. R. Heath and M. A. Ratner, *Phys. Today* **56**, 43 (2003).

[97] B. Y. Zong et al., *Nanotechnology* **24**, 24530 (2013).

[98] C. Kügeler, J. Zhang, S. Hoffmann-Eifert, S. K. Kim, and R. Waser, *J. Vac. Sci. Technol. B* **29**, 01AD01 (2011).

[99] B. De Salvo, J. Buckley, D. Vuillaume, *Current Applied Physics* **11**, e49 (2011).

[100] S. Song et al., *Adv. Mater.* **22**, 5048 (2010).

[101] A. Chung, J. Deen, J. S. Lee and M. Meyyappan, *Nanotechnology* **21**, 412001 (2010).

[102] J. Y. Son, Y. H. Shin, H. Kim, H. M. Jang, *ACS Nano* **4**, 2655 (2010).

[103] P. Ball, *Nature* **445**, 362 (2007).

[104] J. E. Otterstedt, *J. Chem. Phys.* **58**, 5716 (1973).

[105] O. Christiansen, H. Koch, P. Jørgensen, *Chem. Phys. Lett.* **243**, 409 (1995).

[106] C. Hättig, F. Weigend, *J. Chem. Phys.* **113**, 5154 (2000).

[107] L. S. Cederbaum, E. Gindensperger, I. Burghardt, *Phys. Rev. Lett.* **94**, 113003 (2005).

[108] E. Gindensperger, L. S. Cederbaum, *J. Chem. Phys.* **127**, 124107 (2007).

[109] E. Gindensperger, I. Burghardt, L. S. Cederbaum, *J. Chem. Phys.* **124**, 144103 (2006).

[110] E. Gindensperger, I. Burghardt, L. S. Cederbaum, *J. Chem. Phys.* **124**, 144104 (2006).

[111] E. Gindensperger, H. Köppel, L. S. Cederbaum, *J. Chem. Phys.* **126**, 034106 (2007).

[112] M. Basler, E. Gindensperger, H. D. Meyer, L. S. Cederbaum, *Chem. Phys.* **387**, 78 (2008).

[113] H. Tamura, E. R. Bittner, I. Burghardt, *J. Chem. Phys.* **126**, 021103 (2007).

[114] H. Tamura, E. R. Bittner, I. Burghardt, *J. Chem. Phys.* **127**, 021103 (2007).

[115] K. H. Hughes, C. D. Christ, I. Burghardt, *J. Chem. Phys.* **131**, 124108 (2009).

[116] K. H. Hughes, C. D. Christ, I. Burghardt, *J. Chem. Phys.* **131**, 024109 (2009).

[117] I. Burghardt, K. H. Hughes, R. Martinazzo, H. Tamura, E. Gindensperger, H. Köppel, L. S. Cederbaum, in: Conical Intersections: Theory, Computation, and Experiment, *Advanced Series in Physical Chemistry*, Vol. **17**, W. Domcke, D. R. Yarkony, H. Köppel (Eds.), World Scientific, Singapore p. 301-346 (2011).

[118] H. Müller, H. Köppel, L. S. Cederbaum, *New J. Chem.* **17**, 7 (1993).

[119] A. Raab, G. A. Worth, H. D. Meyer, L. S. Cederbaum, *J. Chem. Phys.* **110**, 936 (1999).

[120] G. A. Worth, H. D. Meyer, L. S. Cederbaum, *J. Chem. Phys.* **105**, 4412 (1996).

[121] G. A. Worth, H. D. Meyer, L. S. Cederbaum, *J. Chem. Phys.* **109**, 3518 (1998).

[122] S. Mahapatra, G. A. Worth, H. D. Meyer, L. S. Cederbaum, H. Köppel, *J. Phys. Chem. A* **105**, 5567 (2001).

[123] G. J. Halász, A. Papp, E. Gindensperger, H. Köppel, Á. Vibók, *Prog. Theor. Chem. Phys.* **16**, 287 (2011).

[124] C. Cattarius, G. A. Worth, H. D. Meyer, L. S. Cederbaum, *J. Chem. Phys.* **115**, 2088 (2001).